Advanced Non-Contacting Ultrasonic Techniques for Non-Destructive Testing

Being a Thesis submitted for the degree of Doctor of Philosophy, in the Department of Physics, University of Warwick.

Pertaining to work done in the department of Engineering, University of Warwick.

By Duncan Robert Billson B.Sc., M.Sc.

June 1994

Table of contents

List of figures

Acknowledgements

I would firstly like to thank Dr. David Hutchins (my Ph.d Supervisor) for his guidance, support and friendship throughout the course of the studies leading to the submission of this thesis, without Dr. Hutchins' contribution, this thesis would not have been possible. I would also like to thank all of the people who have helped me in my research at Warwick, although I must apologise to the people whom brevity forbids me to mention.

In the Department of Engineering I have enjoyed the friendship and help from colleagues in the ultrasound laboratory, including Lawrence Scudder, Steve Appleton, Bill Wright and Andy Bashford. I would also like to mention the help that I was given by many of the departmental technicians, including Steve Wallace, Frank Courtney, Viola Kading, Rhod Mortimore, Graham Canham, Huw Edwards, Colin Banks, Colin Bidmead and Geoff Russell.

In the Department of Physics, I would firstly like to thank Professor Stuart Palmer for his generosity in allowing me to work on my thesis whilst in his employ. I would also like to thank Chris Edwards, John Reed, Steve Dixon and Diane Holland for their contribution. Thanks must also be given to Steve Westgate at T.W.I. for providing many of the adhesively bonded samples investigated in this thesis. Finally, I must thank my family for their support and patience, especially whilst I was writing this thesis.

Duncan Billson, June 1994.

Declaration

The work described in this thesis is my own, except where stated as otherwise, and was carried out in The Department of Engineering, University of Warwick between February 1990 and May 1994. No part of this work has been submitted previously to the University of Warwick, or any other academic institution for admission to a higher degree. Some of the work has already appeared in the form of publications which are listed in the bibliography.

Summary

This thesis describes research towards the development of ultrasonic methods to test samples that are difficult to test using conventional techniques, with particular emphasis being given to non-contacting methods. The samples investigated in detail were adhesively bonded structures and zircalloy (a zirconium-niobium alloy).

The adhesively bonded structures were investigated ultrasonically using an ultrasonic resonance technique (referred to as ultrasonic spectroscopy) to analyse suitable ultrasonic waveforms. This thesis starts by explaining a new approach to ultrasonic spectroscopy, and then describes a number of transduction techniques (both contacting and non-contacting) that were devised to obtain waveforms suitable for spectroscopic analysis. These including conventional piezoelectric transducers, laser generation of ultrasound, EMAT reception of ultrasound, and a novel couplant-free transducer. Tests were undertaken on a variety of samples under a number of different conditions, with the experimental results comparing well with those predicted by theory.

Zircalloy was investigated next in an effort to evaluate nondestructively the concentration of hydride in the alloy. This was performed using velocity-temperature measurements (at temperatures up to 500°C) for both shear and longitudinal waves, and by dilatometry (thermal expansion) measurements. Both sets of tests successfully determined the hydride concentrations of test samples.

A separate chapter is devoted to the description of some of the novel transducers developed during the course of this research, including a couplant-free transducer, and several transducers for airborne ultrasound. These transducers were found to operate well, the couplant-free transducer being particularly successful (subsequently finding a number of industrial applications). The final experimental chapter describes the building of both a photoelastic, and a schlieren rig that were used to visualise ultrasound, with the intention of giving an insight into some of the the ultrasonic phenomena that were associated with the rest of the work. The results obtained were invaluable in analysing the results from previous chapters.

CHAPTER 1

INTRODUCTION

1.1 Background

This thesis describes work that has developed non-contacting ultrasonic techniques for the non-destructive testing of difficult materials. This section commences with a brief review of the background of modern ultrasonic nondestructive testing, followed by a short history of the science of ultrasound. After this, a theory section describing both laser generation of ultrasound, and the theoretical basis behind the operation of electro-magnetic acoustic transducers (EMATs) is given. This chapter finishes with a section describing the work in subsequent chapters.

Throughout the last century, both technological advances and economical factors have induced engineers to manufacture products with increasing performance and reliability, and with lower costs. This has been achieved using new and improved manufacturing techniques in conjunction with higher standards of quality control, and has been aided by the availability of new engineering materials. The need for improved reliability of goods, particularly for safety-critical applications, requires that defects are not present in the finished product. This is usually achieved by a variety of routes, including;

i) close monitoring of the manufacturing process,

ii) destructive testing of a proportion of products at stages through their manufacturing process,

iii) testing the finished product beyond its working parameters.

iv) nondestructive testing, which can occur during and immediately after manufacture, and during the service life of the product.

In practice, one or all of these methods are usually applied to ensure that the product in question does not fail in service.

Nondestructive testing is usually applied where it is either economically advantageous, or where it is essential for safety purposes. The application of nondestructive techniques has been increasing since the last war because of both of these reasons;

i) In the first case, modern techniques (such as on-line testing) allow large quantities of products to be tested quickly, reliably and economically, ensuring the quality of the goods produced. Furthermore, if NDT is considered at an early stage in the product design, the extra cost of over-engineering goods to allow for the minority of parts that contain defects is eliminated when such parts are identified and rejected.

ii) NDT is sometimes essential for products, particularly for those that are safety-critical. In these situations, it is usually insufficient to test components only during their manufacture, and a continuous monitoring of these components must be maintained at regular intervals through their service life. In many cases, particularly in the aerospace, nuclear and pressure-vessel industries, this has led to specified procedures being required by both national, and by international law. With the advent of the European Common Market, many of these procedures are being standardised, often resulting in more rigorous procedures.

These factors have led to the increasing application of nondestructive testing, generating a requirement for;

i) New testing techniques for the application of NDT where it has not been

applied in the past

ii) Making conventional testing techniques faster, cheaper and more reliable, (testing for smaller defects, with an increased probability of detection).

Much research is currently being directed throughout the world's scientific community towards these aims, and it is hoped that this thesis might contribute to this field of research. The work described addresses both of the above requirements; firstly by investigating novel techniques for new applications (for example the testing of zircalloy), and secondly by working to improve conventional ultrasonic testing techniques (the couplant-free transducer being an example). Non-contacting techniques can be considered to be especially applicable to both of these requirements, as they are both novel, and are eminently applicable to rapid testing.

1.2 A brief history of ultrasound

The scientific study of sound has been continuing since at least the time of the Greeks, where Pythagoras, in the sixth century B.C., surmised that sound does not travel through a vacuum, (which was not experimentally verified until 1650 by Guericke)[1]. The first studies of sound at frequencies beyond the range of human hearing, have been attributed to Dr. William H. Wollaston in 1820: "Wollaston made numerous observations on the variations in pitch audibility between individuals, and speculated that some insects might communicate by high notes inaudible to humans"[2]. The first developments of practical ultrasonic applications originated from the discovery of piezoelectricity, attributed to Jacques and Pierre Curie in 1880. This, along with the discovery of high-frequency

vacuum-tube amplifiers, lead Langevin to develop an ultrasonic system for submarine detection during the First World War. Whilst this was not perfected until after the armistice in 1918, this discovery prompted rapid growth in the development of ultrasonics in the post WW1 years.

The first applications of ultrasound to the nondestructive testing of metals was by Sokolov (1929), and by Mühlhäuser (1931), who both used continuous-wave ultrasound to detect defects in metals in through-transmission. It was not, however until the second World War that the electronics developed for Radar, were adapted to ultrasonic testing applications, leading to pulse-echo techniques (these, of course, were used earlier for submarine detection, but the fundamental difficulty was the scaling down of the delay between generation, and detection). The first "flaw detectors" for nondestructive testing were developed by F.A.Firestone in America (using a single crystal transducer), and by D.O.Sproule in London (using a twin crystal transducer). These simultaneous developments, (in two continents) may be the cause for the American preference for single-crystal transducers, and for the European preference for twin crystal transducers (this "cultural preference" has often generated problems when trying to compare American N.D.T. standards with British standards).

The first reference to the generation of sound with light (arguably the predecessor of laser generated ultrasound), was by Alexander Graham Bell in 1881, in this he described the operation of his "*photophone*", which exposed discs of a variety of materials to a rapidly-interrupted beam of sunlight[3]. The first experiments that used a pulsed laser to generate ultrasound were performed by White[4] and independently by Askar'yan et al[5] in 1963. Of these, the former was

on solids, and the latter on liquids. More recently, a more thorough study of the nature of laser generated ultrasound for nondestructive testing applications was performed by the Applied Physics group at Hull University[6] in the early 1980's, which preceded a large increase in the applications of these techniques by a multitude of groups throughout the world.

1.3 Background theory

Because of the diverse nature of this thesis, much of the theory necessary for individual chapters is included within those chapters, eliminating the need for a separate theory chapter. The background that is included in this introductory chapter is relevant to most of the following chapters, and is not repeated therein. The theory included here gives a brief description of the physics behind the generation of ultrasound by pulsed lasers, and the reception of ultrasound by EMATs.

a) Laser generation of ultrasound

The generation of ultrasound with a pulsed laser beam is well documented in the literature, an example of which is a review by Hutchins[7]. However it was considered important to give a brief description of ultrasonic laser generation here, as this is of fundamental importance for several chapters in this thesis. It is generally understood that a pulsed laser beam can generate ultrasound in solids by one of three mechanisms, commonly referred to as thermoelastic, ablative, and air-breakdown. The work described in the following chapters uses a laser to generate in both the thermoelastic, and the ablative mode, but not the air-

breakdown mode. However a brief description is given of all three for completeness.

A pulsed laser can generate ultrasound using the "air-breakdown" mechanism by focusing down the laser beam to a point in the air, just above the sample under test, as shown schematically in Figure 1.1. Because light is an electro-magnetic wave, a single photon of light will have a corresponding electric field, the magnitude of which will increase with increasing numbers of (coherent) photons. With a high enough concentration of these photons (which can be achieved by focusing down a sufficiently powerful pulsed laser beam), this can form an electric field sufficiently strong cause the air to break down. This break-down generates an ultrasonic "blast wave" which, when it hits the surface of a sample, is sufficiently strong to transmit a useable quantity of ultrasound into the sample. This technique is used to generate high-amplitude longitudinal waves in samples, without damaging their surfaces[8,9,10]. It has, however, two disadvantages when compared with the other generating mechanisms; firstly that it generally requires higher powered (and therefore more expensive) lasers to generate the same amplitude ultrasonic pulses, and secondly, the blast wave in air has a tendency to affect any ultrasonic receiver that is placed on the same side of the sample as the laser, often precluding the use of this technique for non-contacting pulse-echo work.

The ablative mechanism is used to generate predominately longitudinal waves by focusing the laser onto the surface of the sample, as shown schematically in Figure 1.2. The laser pulse rapidly heats up the surface of the sample, raising the temperature of the material to above its boiling point, causing

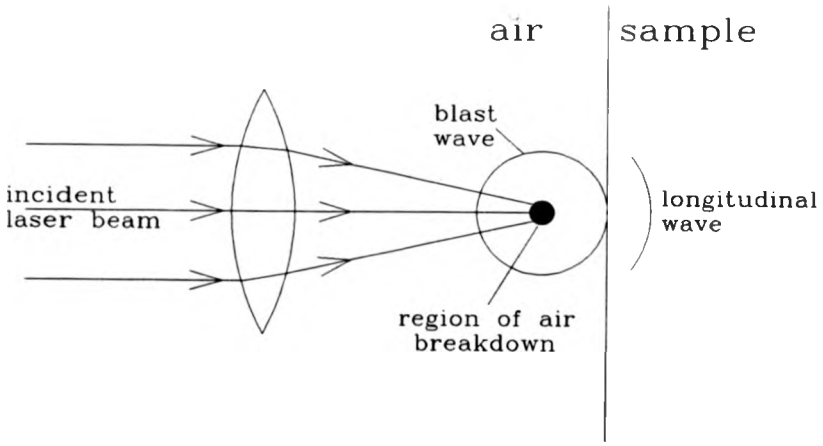

Figure 1.1 laser generation of ultrasound, air-breakdown mechanism.

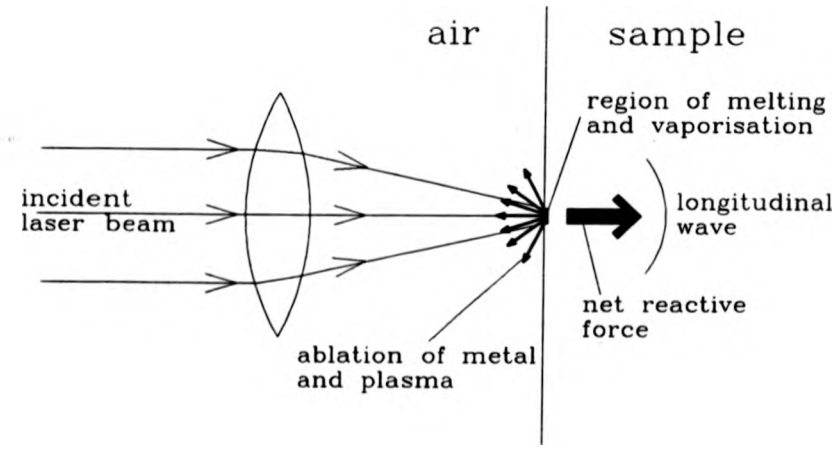

Figure 1.2 laser generation of ultrasound, ablative mechanism.

it to blast, or ablate from the sample surface. This causes an equal and opposite reaction (Newtons' second law) into the sample, which is in the form of a longitudinal ultrasonic wave. This mechanism can produce high intensity longitudinal wave pulses, but with a clean sample, can have the disadvantage of damaging the surface. With a constraining layer over the sample (such as dirt, oxidation, or a purposely applied viscous layer), this damage can however be reduced, or eliminated. A constraining layer can also increase the amplitude of the ultrasound produced by both increasing the absorption of the laser light, and by being significantly easier to ablate, (it must be noted that a constraining layer modifies the nature of the ultrasonic source). The ablation technique also tends to generate shear waves at the same time (which are not always desirable).

The thermoelastic mechanism for ultrasonic generation is highly complicated, and a full description of this phenomenon would not be warranted here, however a simplified diagram depicting this process is shown schematically in Figure 1.3. In this, a laser beam impinges onto the surface of the sample under test, rapidly heating a layer at the surface. This causes the material in this layer to expand, forming stresses which are predominately parallel with the surface of the material. This generates both ultrasonic longitudinal and shear waves which propagate into the sample. The majority of the ultrasonic energy is in the form of shear waves as the shear stresses parallel with the sample surface are constrained (or to put it another way, there is material to "push against"). Forces normal to the sample surface (that would predominantly generate longitudinal waves) are not as well constrained, making this method generally less efficient at generating longitudinal waves (which are usually undesirable when using this

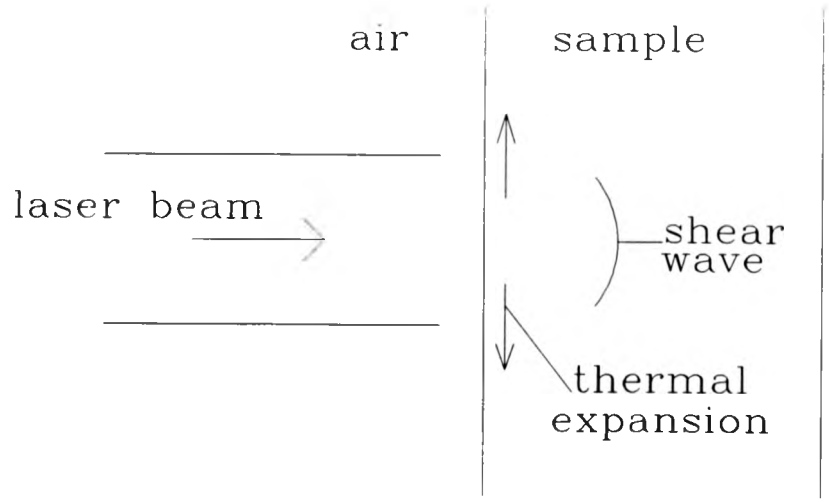

Figure 1.3 laser generation of ultrasound, thermoelastic mechanism.

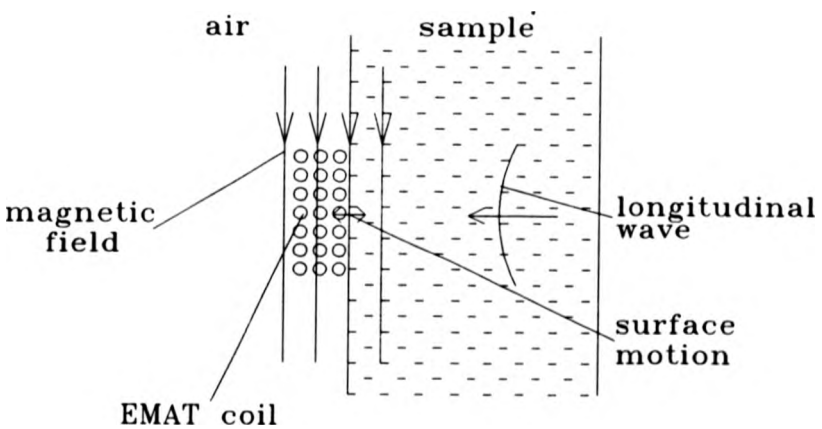

Figure 1.4 The mechanism behind a longitudinal wave EMAT.

method). It should be noted that on epicentre, the predominant shear wave motion is not perpendicular to the sample surface, but is normal to it. This technique does not usually mark the surface of the sample under test. It should be noted that, as with the ablative mechanism, a constraining layer often modifies the ultrasound generated with this mechanism, however a full description of this complication is beyond the scope of this thesis, and the reader is referred to Hutchins[7] and Dewhurst et al[11].

b) Electro-Magnetic Acoustic transducers (EMATs)

As with the Laser generation of ultrasound, the reception (and the generation) of ultrasound by electro-magnetic acoustic transducers (EMATs) has been well documented in the literature, with examples by Kawashima[12], Frost[13], Dobbs[14] and Thompson[15]. However, it was considered important to include a brief description of the theory behind EMAT reception of ultrasound to complement the chapters in this thesis that use EMATs as ultrasonic receivers.

It has been said that there are almost as many EMAT designs as there are papers on EMATs in the literature, however, for the reception of bulk waves, there are two basic configurations; the first being optimised for the reception of longitudinal waves, and the second being optimised for the reception of shear waves.

The EMAT design optimised for the reception of longitudinal waves is shown schematically in Figure 1.4. This shows a longitudinal wave approaching the surface of the sample, which will create motion at the surface of the sample, as shown. Because this motion is in a magnetic field (which is parallel with the

sample surface), this will induce a current to flow within the sample (Lorentz), in a direction perpendicular to both the magnetic field, and the ultrasonic motion (Fleming), this is into the paper in Figure 1.4. This current will, by mutual induction, generate a current in the EMAT coil, which can be amplified to give a waveform. It should be noted that the resultant waveform from this transducer is a measure of the velocity of the sample surface (as opposed to displacement).

The EMAT design optimised for the reception of shear waves is schematically shown in Figure 1.5, the mechanism for this EMAT variant is similar to that described above, but with normally incident shear waves, the ultrasonic motion is parallel with (not perpendicular to) the sample surface. By having the magnetic field now perpendicular to the sample surface, Lorentz is again satisfied, and currents are again picked up in the EMAT coil. Because shear waves are transverse waves, they have the property of being polarised. This necessitates the careful design of coils to match the ultrasonic wave that has been generated. Two examples of coil design (used later in this thesis) are given in Figures 1.6 and 1.7. Figure 1.6 shows a "pancake" coil that is configured to receive radial motion (which can be generated by a laser that is focused to a circle). As the Figure shows, the orientation of the coil is such that the coil wire is perpendicular to the ultrasonic motion. Figure 1.7 shows a linearly wound coil that is configured to detect linearly polarised shear waves (which can be generated either by a laser that is focused to a line source, or by a piezoelectric, normal incidence shearwave transducer). Again, the coil is wound to align the wire to be perpendicular to the ultrasonic motion.

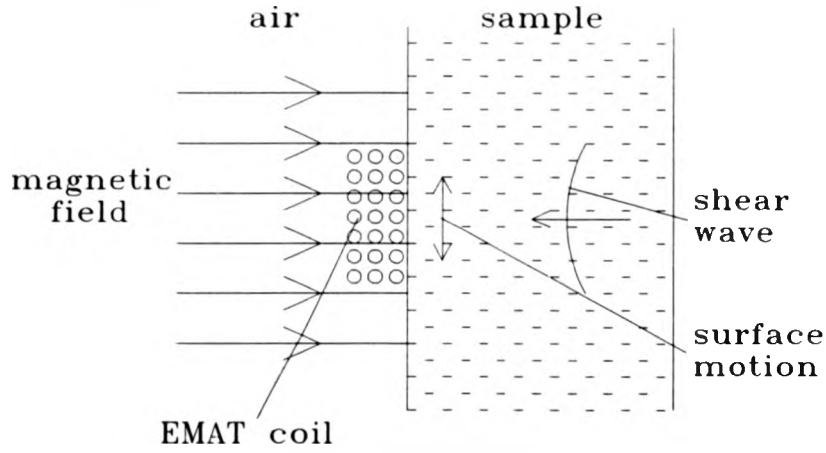

Figure 1.5 EMAT mechanism to detect shear waves.

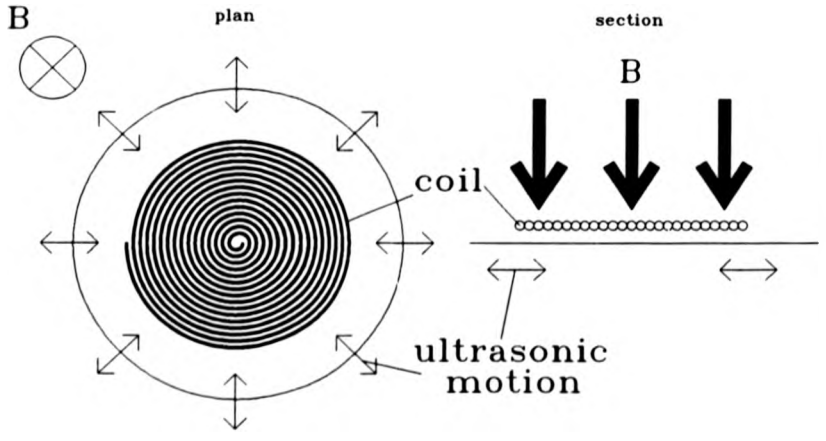

Figure 1.6 Pancake EMAT coil.

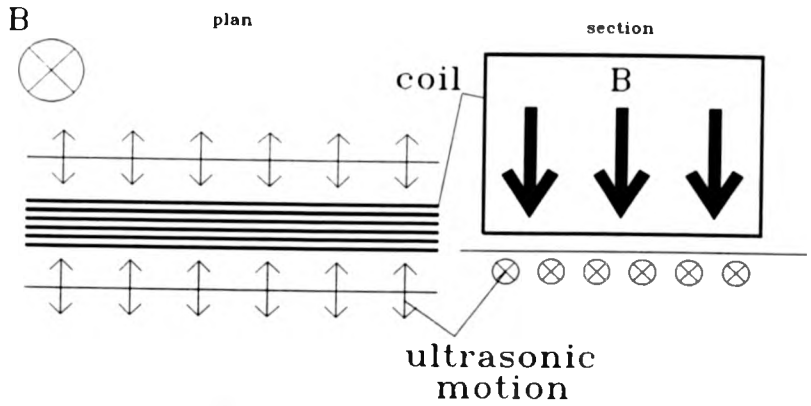

Figure 1.7 Linear coil.

1.4 The following chapters

Chapter 2 acts as an introduction to adhesive bonds, and describes techniques currently used to test these. This chapter then describes in greater detail, a technique that can be used to analyze ultrasonic waveforms obtained from adhesive bonds, known as a spectroscopic or resonance technique. Following this, a description is given of a computer model that can predict the spectroscopic response of bonds. An analysis of the results predicted by this model is given for both good and bad bonds, showing the differences that are predicted. This gives the basis of a technique that allows defective bonds to be identified.

Chapter 3 follows from chapter 2 by comparing experimental spectra obtained from nominally "good" adhesively bonded samples with the spectra predicted by the computer model. The effect of varying the adhesive thickness is investigated, as well as the effect that gross defects in bonds have on the data, showing the efficiency of this technique for detecting "poor" bonds. A number of transduction techniques are investigated (both contacting and non-contacting), and the results obtained are analyzed. One experiment is described that uses non-contacting methods for testing the degradation of a bond at increasing temperatures. The chapter finishes with an investigation into "poor bonds" (which are impossible to detect using conventional techniques) using spectroscopic techniques, aided by tensile testing.

Chapter 4 describes experiments that were performed at elevated temperatures on a zirconium-niobium alloy, known as "zircalloy". This was to measure the concentration of hydrides in the alloy (which have been responsible for failures in CANDU nuclear reactors). The first series of tests necessitated the

development of novel high temperature EMATs for either shearwave or longitudinal wave non-contacting reception of ultrasound, generated by laser. These tests are followed by a dilatometry (thermal expansion) study of the alloy.

Chapter 5 describes a number of transducers that were developed by the author during the course of the research for this thesis, but were not included in other chapters. The first of these transducers is a novel "dry-coupled" transducer which (unlike other dry-coupled transducers) works at frequencies up to 5MHz. This is described fully, and an example is shown of the transducer's effectiveness when testing adhesive bonds using the resonance techniques described in chapters 2 and 3. The other transducers described here are ultrasonic air transducers. These were investigated as successful ultrasonic air transduction could have applications for both spectroscopic testing of adhesive bonds, and for testing zircalloy at high temperatures. Whilst no airborne transducer currently exists with sufficient sensitivity and bandwidth to allow it to be used to test these materials successfully, the results shown here are thought to make a substantial contribution to the field of air transducer technology.

Chapter 6 describes the design, operation and results from two ultrasonic visualisation rigs; the first a photoelastic rig, and the second a schlieren rig. The photoelastic system was used to investigate ultrasound propagating through solids, and the schlieren system was used to look at ultrasound in both air and in immersion. These rigs were built to produce a visual record of ultrasound propagating through models representing the samples investigated in this thesis, using the transducers used in this thesis. The photographic records that were taken were used to supplement the results obtained in the preceding chapters.

1.5 References

1. D.Abbott, "The biographical dictionary of scientists; Physicists", Blond Educational, 1984. p.5.
2. K.F.Graff, "A history of Ultrasonics", in Physical Acoustics, Vol. XV, (1981), pp. 1-97.
3. A.G.Bell, "Upon the production of sound by radiant energy", Philosophical magazine, Vol.11, (1881), pp. 510-528.
4. W.D.White, J.Appl. Phys., 34, (1963), pp. 3559-3567.
5. A.Askar'yan, A.M.Prokhorov, G.F.Chanturiya and M.P.Shipulo, Sov. Phys. JETP, 17, (1963), pp. 1463-1465.
6. A.M.Aindow, R.J.Dewhurst, D.A.Hutchins and S.B.Palmer, "Laser generated ultrasonic pulses at free metal surfaces", J. Acoust. Soc. Am. **69**, (1981), pp. 449-455.
7. D.A.Hutchins, "Ultrasonic generation by pulsed lasers", in Physical acoustics, Vol.18, Eds; W.P.Mason & R.N. Thurston, Academic press, (1988) pp. 21-123.
8. G.Taylor, Ph.d. Thesis, Warwick University, 1990
9. G.Taylor, D.A.Hutchins and S.B.Palmer, J.Phys.D, Vol.28, No.6, (1990) pp. 343-350.
10. G.Taylor, C.Edwards and S.B.Palmer, Nondestr. Test and Eval., Vol.5, No.2, (1990), pp. 135-144
11. R.J.Dewhurst, D.A.Hutchins, S.B.Palmer and C.B.Scruby, J. Appl. Phys., 53, (1982), pp. 4064-4071.
12. K.Kawashima, IEEE Trans, Vol.SU-31, No.2, (1984), pp. 83-94.

13. H.M.Frost in "Physical acoustics", Chapter 3, Vol.14, Eds; W.P.Mason & R.N. Thurston, Academic press, (1979) pp. 179-275.

14. E.R.Dobbs, in "Physical acoustics", Chapter 3, Vol.10, Eds; W.P.Mason & R.N. Thurston, Academic press, (1973) pp. 127-191.

15. R.B.Thompson, in "Physical acoustics", Vol.18, Eds; W.P.Mason & R.N. Thurston, Academic press, (1990) pp. 157-200.

CHAPTER 2

ULTRASONIC TESTING OF ADHESIVE BONDS BACKGROUND THEORY

2.1 Introduction

Adhesives have been used by man for many thousands of years to join parts together, though until relatively recently, adhesive, or glue as it was more commonly known then, was only capable of being used as a sealant, a gap filler or a reinforcement to other joining techniques, such as nailing, screwing or tenon jointing. These adhesives invariably failed when exposed to variations in temperature or humidity. It is only since the second world war that modern adhesives and adhering techniques have been able to produce strong adhesive bonds that could support structures in their own right. This advancement of adhesive technology was led by the aerospace industry where adhesives were used to fix wooden parts of aircraft together, an early example being the Mosquito bomber used in WWII. Today, the aerospace industry still leads in the development of the use of adhesives, as modern aircraft require very strong, stiff, cost effective and lightweight methods of joining components together. Unfortunately, the use of adhesives in critical parts has been severely hampered by the difficulty of testing such joints nondestructively, both at the time of manufacture, and in service. This single factor has precluded the use of adhesive bonds in many joints where they would be best suited. Current production procedures require that test components are made at the same time as the production article, the former are then destructively tested to ensure adequate bond strength. These procedures are costly, do not actually test the production components (and only imply their strength), and give no indication of any degradation of the component during service. It is not therefore surprising to find that a great deal of work in developing nondestructive testing techniques to test

adhesive bonds has been carried out by many authors, It is hoped that the work described here will make a small contribution to the mass of work already carried out.

This chapter serves as a introduction to the theory of adhesive bonding, defects that can occur in these bonds, and nondestructive testing techniques that have been applied by other authors to detect these defects. Following on from this, there is a description of the theory behind a technique that analyses ultrasonic waveforms from adhesive bonds in the frequency, rather than the time domain.

Chapter 3 of this thesis follows this chapter by describing the development and application of techniques that utilise this approach to test adhesively bonded aluminium lap-joints. The first part of this chapter describes experiments done using contacting transduction, used initially to develop the application of spectroscopic techniques, and subsequently demonstrate both their capabilities and limitations. The second part of the chapter follows on by describing the application of ultrasonic spectroscopy using non-contacting transduction to various testing problems.

2.2 Usage and advantages of adhesive joints

Structural adhesive bonding is becoming an increasingly important joining technique in modern engineering applications. Adhesive bonds can have a number of distinct advantages over other joining techniques, which include:

i) Adhesive bonding produces a more uniform stress distribution over the area of the bond than other localised connectors such as rivets, bolts or spot-welds. This eliminates large, localised stress concentrations (that would be found around these connectors) and hence increases the strength of the bond. This can also make the joint less susceptible to fatigue and vibration.

ii) The stiffness of the joint is usually increased when adhesive bonding is used. This can increase the overall strength of the complete structure

iii) The joint can provide an integral seal against the unwanted ingress of air or water, offering better environmental resistance and reducing structural degradation.

iv) Adhesive bonding reduces the machining of the components, saving costs.

v) Adhesive bonding allows joints to be made between dis-similar materials that could not be joined by welding, soldering or brazing techniques. It also greatly reduces galvanic corrosion problems between dis-similar metals, and does not introduce any distortion.

vi) By increasing joint strength, adhesive bonds allow the use of lighter components, both reducing initial materials costs, and reducing the weight of the finished product (this is particularly relevant to the aerospace industry).

vii) Adhesive bonds can be accurately jigged to produce an aesthetically

pleasing structure.

Adhesive bonds can produce very strong bonds in both compression and shear modes, but do not work well in peel modes. The relative ability of a joint to withstand loading in the compression, shear and peel modes is crudely reflected by the ratio 1000:100:1[1]. This affects the designs of adhesive joints, which try to reduce, or eliminate any peel stresses, a number of common engineering adhesive joints have been given by Adams and Cawley[2], and are shown in Figure 2.1.

2.3 Defect types in adhesive joints

A simple adhesive joint consist of adherends (the components being adhered together) and adhesive layers, as shown in Figure 2.1. Some of the defects that can occur in these bonds are shown schematically in Figure 2.2. These defects can be separated into three regions:

(a) Within the adherend

Techniques for testing these are the conventional ultrasonic methods.

(b) Within the adhesive layer

A number of different types of defects can occur within this layer, the more common forms being;

i) Cracks, these are often caused by poor curing, by thermal stresses during manufacture, or by impact damage during service. Brittle adhesives are predominantly at risk with this type of defect.

ii) Porosity, caused by either volatiles or entrained gases, (principally air and water vapour).

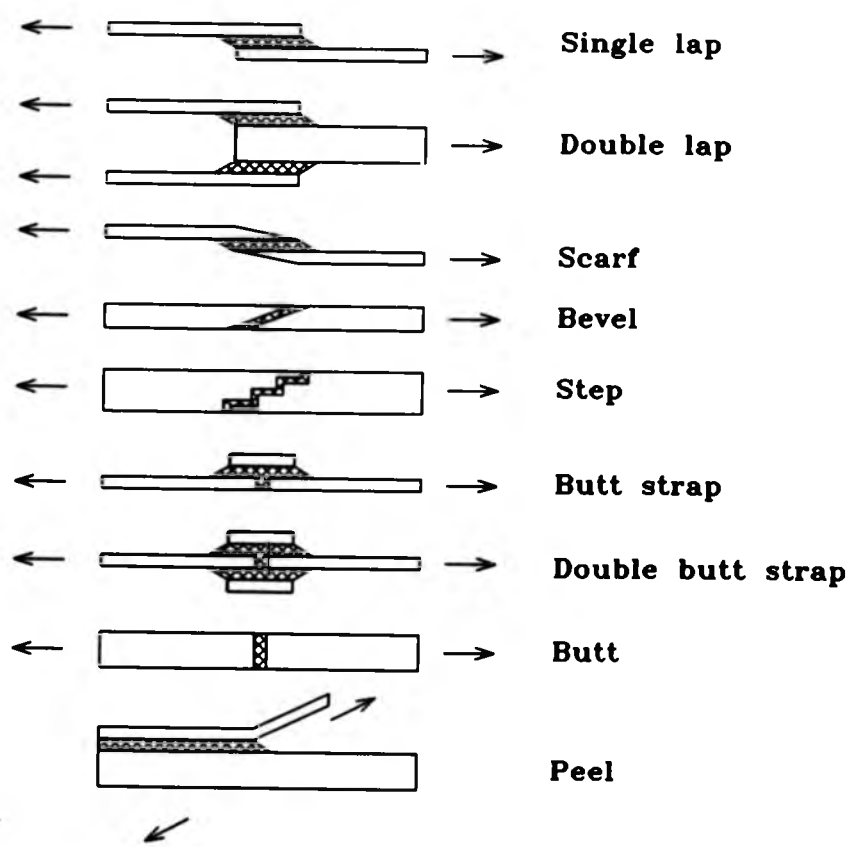

Figure 2.1 Some common Engineering adhesive joints, after Adams and Cawley[2].

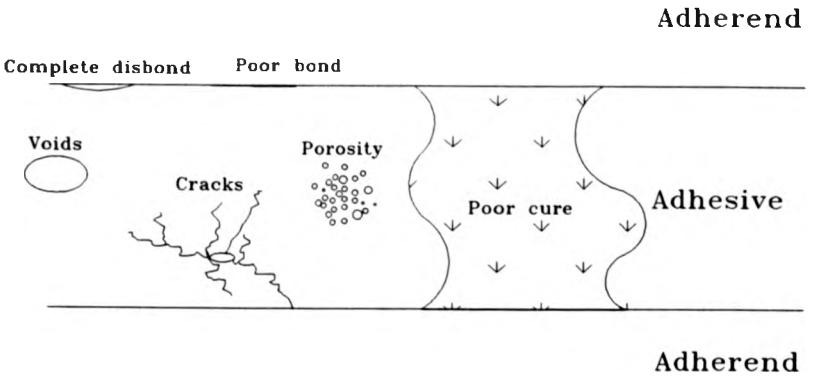

Figure 2.2 Schematic diagram of typical defects in an adhesively bonded joint

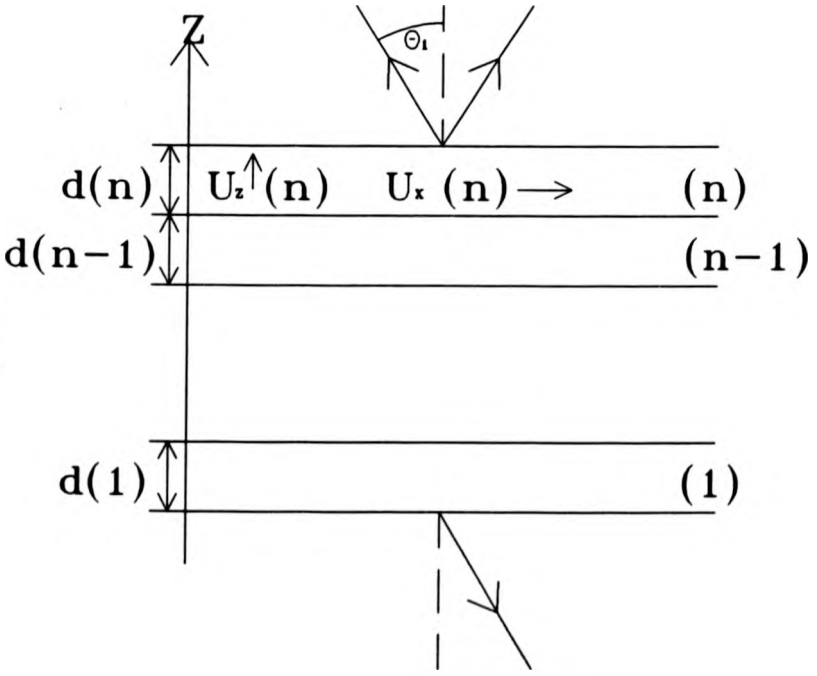

Figure 2.3 Schematic diagram of a multilayered structure

iii) Voids, caused by either coalescence of porosity, by air entrapment during lay-up, by volatile compounds being evolved by the adhesive, or by insufficient or unevenly applied adhesive.

iv) Areas of poor cure, which give a poor cohesive strength. These can occur because of aged/defective adhesives, contaminants, incorrect mixing, or by an incorrect thermal curing cycle. This is sometimes a localised defect, but more commonly occurs throughout the whole of the adhesive layer.

(c) At the adhesive-adherend interface

Defects at this interface can cause either a complete disbond (known as a zero-volume disbond) or a partial disbond (known as a poor-bond). Complete disbonds are possible to detect nondestructively using one of a variety of techniques, which are discussed in greater detail later in this chapter. The second group of adhesive-adherend defects, namely those with partial disbonds, are notoriously difficult to detect, and a great deal of research has been undertaken, and is continuing to try to develop techniques to be able to detect this type of defect reliably. To date, no single method has been demonstrated to be able to do this reliably, indeed the ability to do this has been described as the "holy grail" of nondestructive testing[3].

Interface defects can be caused by contaminants (such as oil, grease or unremoved surface coatings such as peel ply), a loose coating of oxides on the adherend, faulty adhesives (caused for example, by the adhesive being left unadhered too long, and drying out) and in-service degradation, caused by either the adherend corroding, or aggressive chemicals and water degrading the adhesive.

2.4 Nondestructive methods of testing adhesive bonds

A multiplicity of nondestructive test methods have been applied to different defect types in adhesive bonds, with a varying range of success. Cawley has reviewed much of the work done in this field, and has produced a table of defect type against NDT techniques[2].

A brief description of some of the test methods used to investigate adhesive bonds is given below

2.4.1 Ultrasonic test methods

Ultrasonic test methods constitute the majority of the techniques used for investigating adhesive bonds. Most ultrasonic techniques have at one time or another been applied to adhesive bonds, and a number of these are now discussed.

Normal incidence ultrasonic amplitude measurements have been investigated by using either a single ultrasonic transducer in pulse-echo mode, or by using a pair of transducers in either pulse-echo or through transmission modes. Gross defects in the bond such as complete disbonds, porosity or inclusions, can usually be detected by monitoring the amplitude of a single pulse in the ultrasonic waveform. Complete disbonds will stop any transmission across an interface, extinguishing the pulse in question, inclusions and porosity will have the effect of scattering the propagating ultrasound, thus reducing the signal amplitude. Poor curing of the adhesive can often lead to an increase in attenuation, again reducing the signal amplitude. Amplitude measurements are easy to make using conventional ultrasonic equipment, and lend themselves well to C-scans, allowing

two dimensional images of the adhesive bond under test to be made easily, these are easily interpreted, and are commonplace throughout the NDT industry, and it is therefore not surprising to learn that it is this type of technique that is most commonly used in practice. In pulse echo or pitch-catch mode, the pulse that is monitored is usually either the backwall echo from the sample, or when used in immersion this is from a flat reflector placed some distance behind the component. In through transmission mode, the pulse that is generally monitored is the first arrival through the component. Work has been reported by a number of authors monitoring the amplitudes of specific reflections from adhesive-adherend interfaces. However, the adhesive layer under investigation is invariably thin, and for standard pulse-echo techniques a high frequency, broadband pulse is necessary to resolve the interfaces. However as most adhesives attenuate ultrasound strongly, especially at the frequencies necessary, this makes this technique very difficult for most applications. Moreover, components containing more than one adhesive layer give increasingly complicated waveforms due to multiple reflections within the structure, making this technique even less desirable. One way around this problem is to analyze the ultrasonic waveforms in the frequency, rather than the time domain. This technique overcomes the need for such difficult waveform requirements, and is sometimes referred to as ultrasonic spectroscopy. This technique is described in greater detail later on in this chapter, and is backed up by experimental data in the next chapter.

By using the above techniques, and paying particular attention to the ultrasonic transit time through the bond line, a number of authors[4,5] have calculated the ultrasonic velocity in the adhesive (usually by measuring the

adhesive thickness accurately) to give information about the state of the adhesive, either to monitor the curing of the adhesive, or to imply the state (and therefore the cohesive strength) of the adhesive.

Techniques involving investigation of the bond with non-normal (oblique) incidence ultrasound have been considered, in an attempt to identify weak adhesive-adherend interfaces. The theory behind this approach is to try and introduce ultrasonic stresses and displacements parallel to the interface surface, causing "slippage", at poor adhesive-adherend interfaces. Theoretical models have predicted that ultrasound is capable of showing a discontinuity of stresses and displacements at a "slipping" bond line, which would be continuous at a good bond line. The ultrasonic stresses and displacements parallel to the interface are present as components of either refracted longitudinal waves, or by mode-converted shear waves. As will be better described later on in this chapter, and experimentally demonstrated in the next, a technique using a contacting piezoelectric SH wave transducer has been developed to generate normal incidence shear waves which propagate perpendicular to the interface, and therefore have stresses and displacements parallel to the interface. This improves on the above as, firstly all of the ultrasonic stress and displacement is in the correct orientation to identify slippage (not just a small component, as for the oblique incidence cases above), and secondly the ultrasound is at normal-incidence, greatly simplifying the analysis.

Acousto-ultrasonic testing has been reported as a technique that has been used to investigate adhesive bonds[6,7], and involves the use of two piezoelectric ultrasonic transducers placed a set distance apart on the surface of the structure

being investigated. One of the transducers generates either an ultrasonic pulse, or a wavetrain, whilst the other receives the ultrasonic signal after it has propagated through the structure under test. The signals are then processed using techniques analogous to those used for acoustic emission. This technique has been reported as being able to detect disbonds in adhesive bonds, and has the advantage of testing relatively large areas at a time. However, this method does not always give satisfactory results, and the reasons for this are not entirely clear[2].

Adhesive bonds usually take the form of a thin adhesive layer sandwiched between two adherends, and this allows Waves such as Lamb waves, Rayleigh waves, and Stonely waves to propagate within and around the adhesive layer. This has lead to a number of authors looking at the propagation of such waves through adhesive bonds to try to develop techniques to detect defects within the bond layer[8]. Lamb waves are elastic plate waves which propagate dispersively through a plate, having a number of both symmetric and anti-symmetric modes[9]. Rayleigh waves are elastic surface waves which decay exponentially below the surface, and propagate non-dispersively[10]. Stonely waves are analogous to Rayleigh waves, that (if certain conditions are satisfied) propagate at the interface between two media[11]. These wave types which, when propagating through an adhesive bond can become intimately linked, and are sometimes indistinguishable from each other, can be used to investigate a section of a bond at a time. This would allow a technique using these waves to be relatively rapid, and indeed it has been reported that such techniques have been successful in detecting disbonds, and in monitoring the properties of the bulk adhesive. However, this line of investigation presents a number of difficulties in that the waves propagating through the

adhesives have a complex structure[12], so that their analysis is generally very difficult, especially when the huge variety of adhesive types, and bond designs are considered. Details of the adhesive type, thickness and adherend material and thickness would have to be accounted for, for every bond investigated. Another problem with this line of investigation is that of access, as a number of techniques require that the probes are attached to the adherend on the same side as the adhesive layer, which, in practice is often impossible. Further problems arise when adhesive fillets (the excess adhesive found at the end of adhesive joints), and surface coatings are present, as these can affect the results.

2.4.2 Mechanical impedance measurements

Mechanical impedance methods are derived from what is often referred to as the "coin-tap" technique, an early, well known application of which was the "wheel tap" method use for testing the steel "tyres" on locomotive wheels (which were press-fitted together). This technique involved the engineer hitting the wheel with a hammer and listening to the corresponding ringing. The tone of this would indicate whether the tyre was defective or not. When a structure is excited by a impulsive force, such as a tap from a (calibrated) hammer, this can cause the structure, or part of the structure to resonate, this is usually at relatively low frequencies (up to 2kHz). A gross defect, such as a disbond, can lead to a change in the mechanical impedance of part of the structure, and thus change this resonance. This can either be looked at globally (examining the resonance of the whole structure), or locally (examining the area immediately surrounding the point of excitation), depending on the nature of the structure, and the type of

defect being investigated. Global methods have the obvious advantage in that they test the whole component, making this a quick, and therefore a very cost-effective technique. Local techniques are particularly applicable to large areas of bonds, where the bond line is under a thin, flat adherend, for example as is found with some honeycomb structures. Mechanical impedance techniques are particularly suitable to monitor the performance of components throughout their service life, since a calibration measurement (in the form of a waveform, or FFT), can be made with the component at manufacture, and a changes in a subsequent measurement will indicate a degradation of the component. These techniques have been in use for a number of years, and a number of commercial instruments are available that use them, including the Fokker-bond tester, Mk.II, The Tap-ometer, the sondicator, and the Shurtronics harmonic bond tester. The theory behind such techniques has been investigated by Cawley[13], and a number of papers applying these techniques to real components are in the literature[14].

2.4.3 Thermography

The use of thermography for adhesive bond testing relies on the bond exhibiting defects that will affect the thermal characteristics of the surface of the adhered structure. This requires that the adherend is relatively thin (with ideally a low thermal conductivity), and is suitable for inspecting defects such as the absence of adhesive, gross disbonds and an excess of adhesive. The technique studies the change of temperature of the structure's surface to imply the state of the bond. The sample is first heated, either by a flash-lamp or a hot air blower, and the sample surface is then monitored to look at the change in temperature

with time. This can be done with either temperature-sensitive liquid crystals painted on to the sample surface, or with an infra-red camera, the latter usually giving better results, but having high equipment costs. A much quoted example of a practical application of this technique is the inspection of helicopter rotors at Westland Helicopters, Yeovil. This technique is described in some detail by Reynolds[15]

2.4.4 Optical local-amplitude methods

This group of techniques have been shown to be able to detect gross disbonds, and work by comparing the very small surface profile change of a structure before and after some form of stress is applied to it. By using techniques such as double exposure holography[16,17], electronic speckle pattern interferometry (ESPI)[18], shearography, or Moire-fringe interferometry, an image consisting of a series of fringes corresponding to variations in the surface displacement of the structure can be taken, with areas of gross disbonding showing up as irregularities in the fringes.These techniques tend to have relatively high equipment costs, but can scan large areas quickly, allowing rapid inspection of parts, and may be cost effective where large areas of structure are to be inspected. Stress may be applied to the structure either mechanically, by placing the component under vacuum/high pressure, or by localised heating. A variation on this technique involves vibrating the structure at a resonant frequency, and producing a time-averaged hologram of this motion[19].

2.5 Resonance studies of adhesively bonded aluminium joints

2.5.1 Background

Ultrasonic spectroscopy has already been mentioned in section 2.3.1 of this chapter, and refers to the analysis of ultrasonic waveforms in the frequency, rather than the time domain. Testing adhesive bonds in the frequency domain can have a number of advantages, as adhesive bonds are difficult to test with conventional ultrasonic techniques in the time domain. This is because the bond layer is invariably both thin and highly attenuative of ultrasound. For standard pulse-echo techniques, a high frequency, broadband pulse is necessary to achieve sufficient resolution to resolve specific adherend-adhesive interfaces[20]. However, most adhesives attenuate ultrasound strongly, thus precluding the use of sufficiently high frequencies. Moreover, structures containing more than one adhesive layer give increasingly complicated waveforms due to multiple reflections within the structure.

This approach to adhesive bond testing started in the 1950's with the development of the Fokker bond tester, which measures changes in the resonant frequency and impedance of a transducer attached to a bonded joint [21]. More recent work has attempted to quantify the theory behind such techniques, which are commonly collectively known as ultrasonic spectroscopy[22,23]. Guyott and Cawley have modelled a simple adhesive bond as three solid cylinders in axial vibration joined end on[24]. This predicts vibrational modes for normal incidence longitudinal waves that agree well with experiment. It would however, be difficult to extend this model to take account of shear waves, non-normal incidence, and

multilayered adhesive bonds.

An alternative approach to the model used by Guyott and Cawley is a wave model, based on work done by Brekhovskikh[25]. This was applied by Madaras *et al*[26] to investigate a multi-layer structure containing interfaces and bonds, a thick, resonant, steel layer obscuring an artificial disbond beneath. Resonance of the steel layer was shown to be influenced by the bonding conditions, and an image was presented based on the amplitude and phase of the resonance. This model can be used to predict the exact shape of the reflected or transmitted spectrum for a given bonded sample, and can also incorporate non-normal incidence, shear waves and multiple adhesive layers[27]. It is this computer model that has been used as the basis behind much of the experimental work on adhesive bonds presented in this thesis, and a description of the theory underlying this model follows.

2.5.2 Frequency response prediction of adhesively bonded structures

An adhesively bonded joint responds to ultrasound in much the same way as a dielectric coating on an optical lens responds to light, in that waves reflected from various interfaces within the structure interfere with each other. This phenomenon causes the ultrasonic transmittivity / reflectivity coefficient of an adhesive bond to vary with frequency in a way that is characteristic of the structure of the bond, and it is this phenomena that is studied in ultrasonic spectroscopy. When a bond is insonified by a broad-band ultrasonic pulse, a frequency spectrum can easily be calculated from the reflected or transmitted ultrasound by using a simple Fast fourier transform algorithm. This can then be

compared to the frequency spectrum of a "good" bond, predicted by the computer program described below, thus allowing the condition of the bond to be inferred.

To understand the theory behind the model, first consider an elastic plate, consisting of an arbitrary number (n) of isotropic layers. This plate is bounded by a liquid layer at its upper surface, and either a liquid or solid at its lower surface. This is shown schematically in Figure 2.3. Each layer is denoted by an index (i), and has a thickness d(i), a density, $\rho(i)$, and longitudinal and shear velocities, $C_p(i)$ and $C_s(i)$ respectively. The model can incorporate attenuation in each layer by assigning an imaginary part to the wave velocities[25]. The problem is solved by investigating the reflected and transmitted energy, for an incident plane wave at a certain frequency. The response to any time excitation can be analyzed using a Fourier superposition of the required frequencies. In the theory, the angle of incidence from the upper fluid to the multi-layer structure is adjustable. All distances are measured relative to the set of coordinates shown in Figure 2.3, with the z-direction being normal to the interfaces between each layer. The components of displacement (U) and stress (σ) at the lower interface for each layer (i) are denoted by $U_x(i)$, $U_z(i)$, $\sigma_x(i)$ and $\sigma_z(i)$. Because of the assumption that all waves are plane and continuous, all waves have a common propagation component of

$$e^{j(\chi x-\omega t)}$$

where ω is the angular velocity, and χ is the x-component of wavenumber, defined as;

$$\chi = (\omega / C_1).Sin(\tau_1) \qquad (2.1)$$

with τ_1 being the angle of incidence from the liquid of density, ρ_1.

At each interface within the layered medium, four boundary conditions have to be satisfied (two each for the displacement and stress components). An efficient method for solving the resultant equations is by the matrix transfer technique, introduced by Thompson[28] and described in the book by Brekhovskikh[25]. Using the boundary conditions that exist between one layer (i-1) and its neighbour (i), a propagation matrix is defined as

$$\begin{vmatrix} U_x(i+1) \\ U_z(i+1) \\ \sigma_x(i+1) \\ \sigma_z(i+1) \end{vmatrix} = \begin{vmatrix} a_{11}(i) & a_{12}(i) & a_{13}(i) & a_{14}(i) \\ a_{21}(i) & a_{22}(i) & a_{23}(i) & a_{24}(i) \\ a_{31}(i) & a_{32}(i) & a_{33}(i) & a_{34}(i) \\ a_{41}(i) & a_{42}(i) & a_{43}(i) & a_{44}(i) \end{vmatrix} \begin{vmatrix} U_x(i) \\ U_z(i) \\ \sigma_x(i) \\ \sigma_z(i) \end{vmatrix} \qquad (2.2)$$

where the matrix coefficients $a_{ij}(i)$ can be found in several works[25,28]. By successive applications of the above, the ultrasonic signal at the chosen frequency at the top of the composite plate (with $i = n+1$) can be related to that at the bottom face, using the following matrix:

$$\begin{vmatrix} U_x(n+1) \\ U_z(n+1) \\ \sigma_x(n+1) \\ \sigma_z(n+1) \end{vmatrix} = \begin{vmatrix} A_{11}(i) & A_{12}(i) & A_{13}(i) & A_{14}(i) \\ A_{21}(i) & A_{22}(i) & A_{23}(i) & A_{24}(i) \\ A_{31}(i) & A_{32}(i) & A_{33}(i) & A_{34}(i) \\ A_{41}(i) & A_{42}(i) & A_{43}(i) & A_{44}(i) \end{vmatrix} \begin{vmatrix} U_x(1) \\ U_z(1) \\ \sigma_x(i) \\ \sigma_z(1) \end{vmatrix} \qquad (2.3)$$

Where the matrix A is obtained by taking the product of all matrices a(i):

$$[A_{ni}]=[a_{ij}(n)].[a_{jk}(n-1)]...[a_{im}(2)].[a_{mn}(1)] \quad (2.4)$$

This matrix transfer technique uses an iterative approach to obtain a solution, and has been used in a computer program, the results of which are presented below. This program was initially developed by L.F.Bresse[29]. The program requires that the characteristics of each layer are input, namely the thickness, density, longitudinal and shear velocities, and attenuation coefficients of the layer (which are entered as the complex coefficients of the acoustic velocities). The output from the computer program is in the form of either the reflection or transmission coefficient, as a function of frequency, which can then be conveniently plotted to give the transmission or reflection spectrum.

2.5.3 Explanation of the predicted spectra

Consider a composite sample, representing a bonded joint with a layer of epoxy adhesive between two 0.754mm thick aluminium plates, the properties of these materials being:

	$C_p(ms^{-1})$	$C_s(ms^{-1})$	$\rho(gcm^{-3})$
aluminium	6350	3100	2.7
epoxy	2580	1100	1.3

The computer program described above predicts both the reflectivity and transmittivity for such samples, and examples of the reflected spectra for normal incidence longitudinal waves for samples with layers of adhesive 0 and 0.1mm thick are given in Figures 2.4 and 2.5 respectively. These show a series of minima, which correspond to acoustical resonances within the various layers, and layer

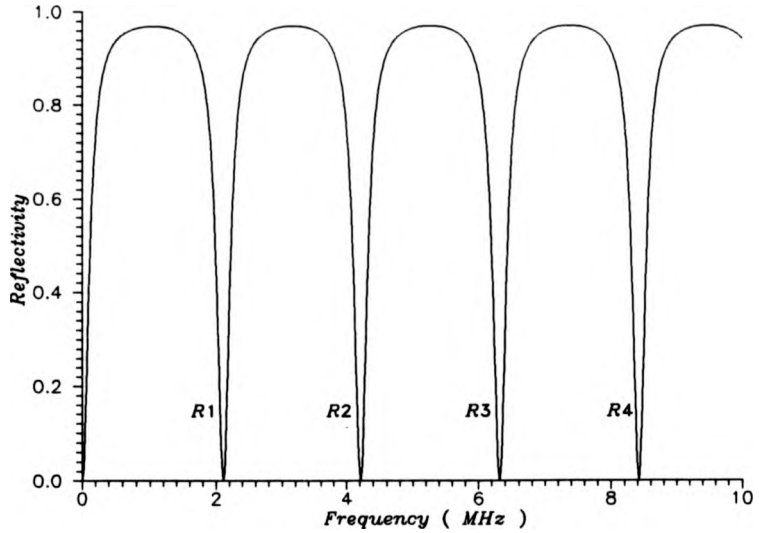

Figure 2.4 Predicted frequency response of an adhesively bonded lap joint to longitudinal waves, the joint having 0.754mm aluminium adherends and no adhesive layer

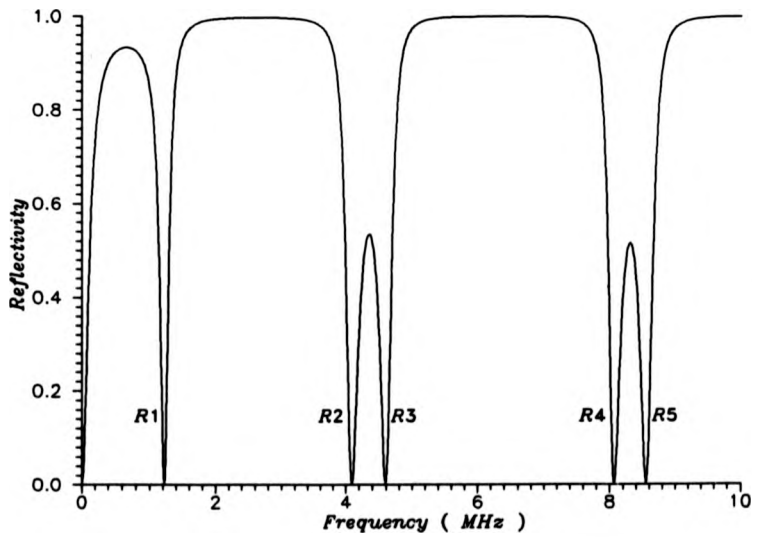

Figure 2.5 Predicted frequency response of an adhesively bonded lap joint to longitudinal waves, the joint having 0.754mm aluminium adherends and 0.1mm of epoxy adhesive

combinations within the sample. It should be noted that the ultrasonic attenuation was not included in these calculations, although this could have been done easily. The predicted modes have been analyzed for a simple lap joint by Guyott and Cawley[2], who have identified some of the lower resonances.

To understand the origins of the individual resonances in a spectrum, first consider the simplest case, i.e. a lap joint with a vanishingly small adhesive layer (or an aluminium plate twice the thickness of the adherends). The lowest order resonance for this is depicted in Figure 2.6, which shows the displacement U_x against through thickness direction (x). This is analogous to Kundt's tube, with the thickness being half a wavelength thick. Compare this now with Figure 2.7, which depicts the next resonance, with the structure being a wavelength thick, and with Figure 2.8, which has the structure being 1.5 wavelengths thick. This trend continues, with more resonances at 2λ, 2.5λ, 3λ and so on. These resonances, when plotted on a graph will be equally spaced (by 0.5λ), and were predicted by the computer program (using the material values given above), to give the plot of reflectivity against frequency shown earlier in Figure 2.4. The resonances are seen to be regularly spaced, and the first resonance is marked by the symbol R1, the second R2, and so on.

Consider now Figure 2.9, which again depicts the first (the lowest, or R1) resonant mode, in a sample which now has a thin layer of adhesive introduced (the thickness of the adhesive is much less than half the wavelength of ultrasound being considered). The adhesive obviously has a much lower Young's modulus than the aluminium, and the strain caused by the ultrasound (seen as the gradient of Ux) is concentrated in this layer. This has the effect of decreasing the resonant

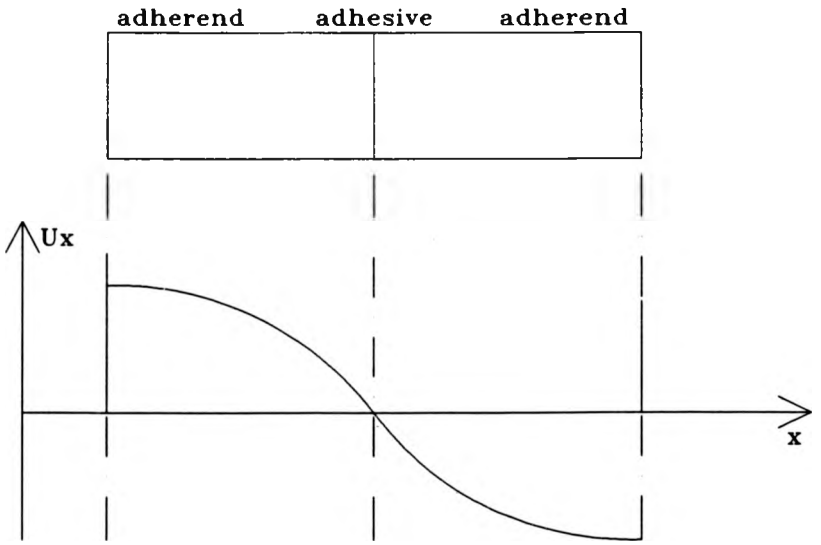

Figure 2.6 Mode shape of the first (R1) resonance of an adhesive lap joint, no adhesive layer

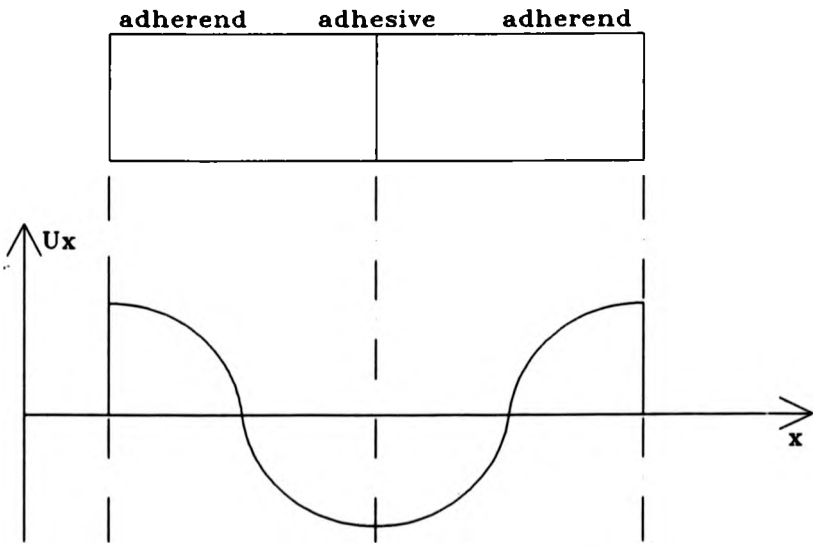

Figure 2.7 Mode shape of the second (R2) resonance of an adhesive lap joint, no adhesive layer

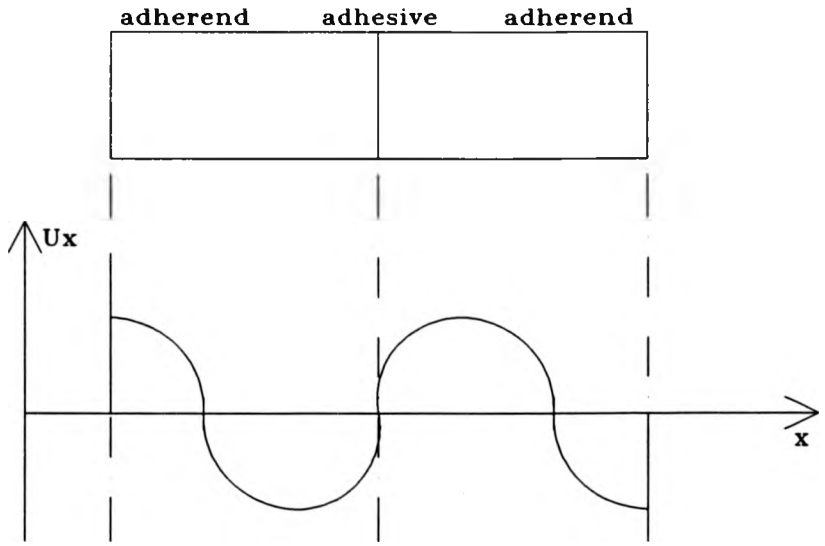

Figure 2.8 Mode shape of the third (R3) resonance of an adhesive lap joint, no adhesive layer

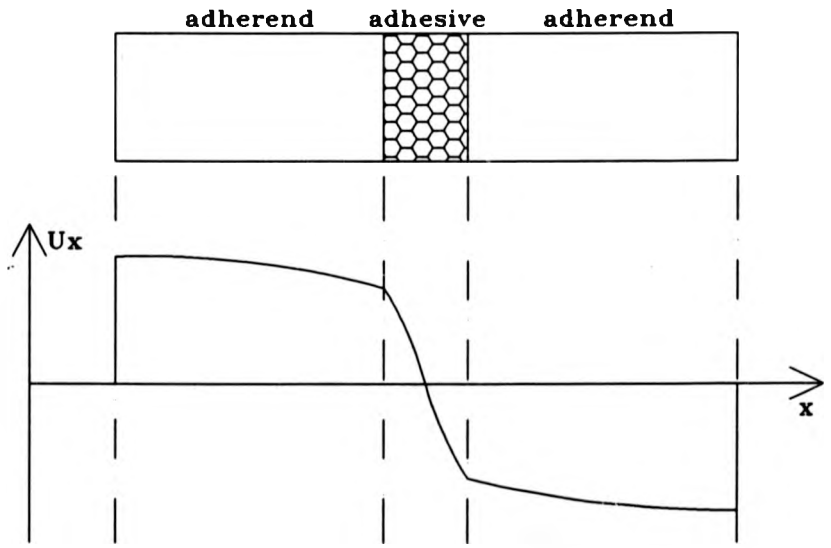

Figure 2.9 Mode shape of the first (R1) resonance of an adhesive lap joint, thin adhesive layer

frequency. Compare this now with Figure 2.8, representing the second or R2 resonance. This mode is symmetric and therefore exerts little strain within the adhesive layer (Ux does not exhibit a large gradient across the adhesive layer), the consequence of this is that the frequency of this mode does not change dramatically as a result of adding the adhesive layer. This is not the situation when the third resonance is considered (R3), as shown in Figure 2.11. This is an anti-symmetric mode, and the strain is again concentrated within the adhesive layer, causing the resonant frequency to decrease dramatically to just above that for the R2 mode. This trend continues as the resonant mode increases, with symmetric modes changing little as a result of adding the adhesive layer, and antisymmetric modes changing markedly. This effect forms "pairs" of resonances (above the R1 mode), which are seen in the spectra predicted for a bond with a 0.1mm thick adhesive layer, shown in Figure 2.5. This effect can be more clearly be seen in Figure 2.12, which is a contour plot of the reflected spectra as the adhesive thickness is increased. At the bottom of the plot, with zero adhesive thickness, the resonances occur regularly at 2.1, 4.1, 6.2, 8.3 and around 10 MHz. The first, R1 mode (2.1 MHz at the bottom) is seen to change rapidly, whereas the second mode, R2, a symmetrical mode, remains relatively stable (up to around 0.25mm thick adhesive). The third resonance, R3, an anti-symmetrical mode, (6.2MHz at the bottom) changes rapidly in frequency in the same way as the first mode.

This theory breaks down when the wavelength of the ultrasound in the epoxy approaches twice the epoxy thickness, although, as Figure 2.12 shows, this pairing still tends to occur. The important conclusion that must be made from this

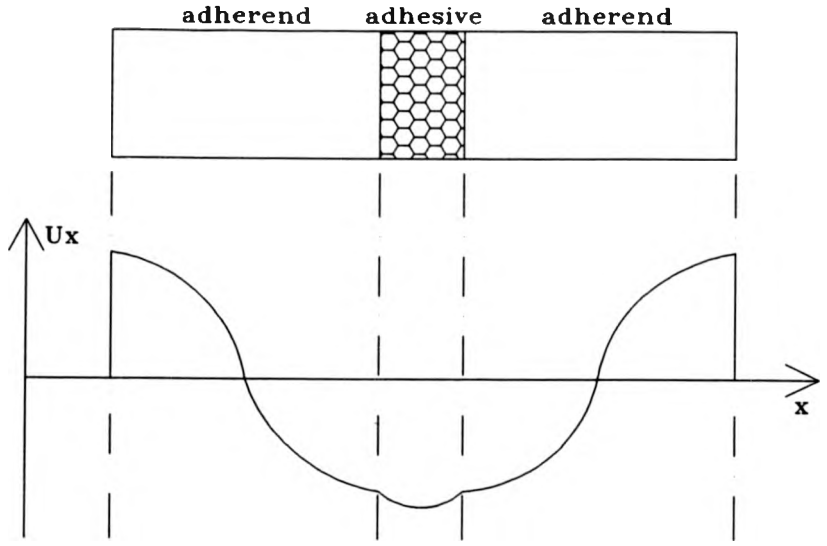

Figure 2.10 Mode shape of the second (R2) resonance of an adhesive lap joint, thin adhesive layer

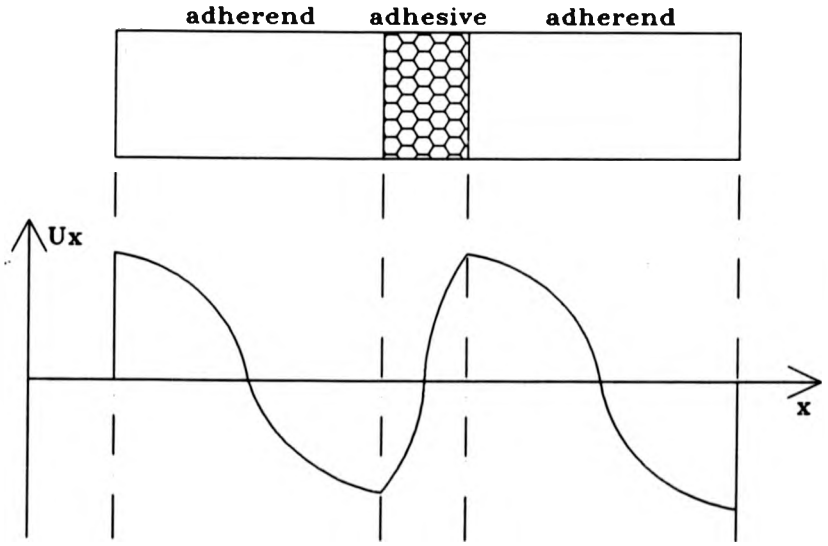

Figure 2.11 Mode shape of the third resonance (R3) of an adhesive lap joint, thin adhesive layer

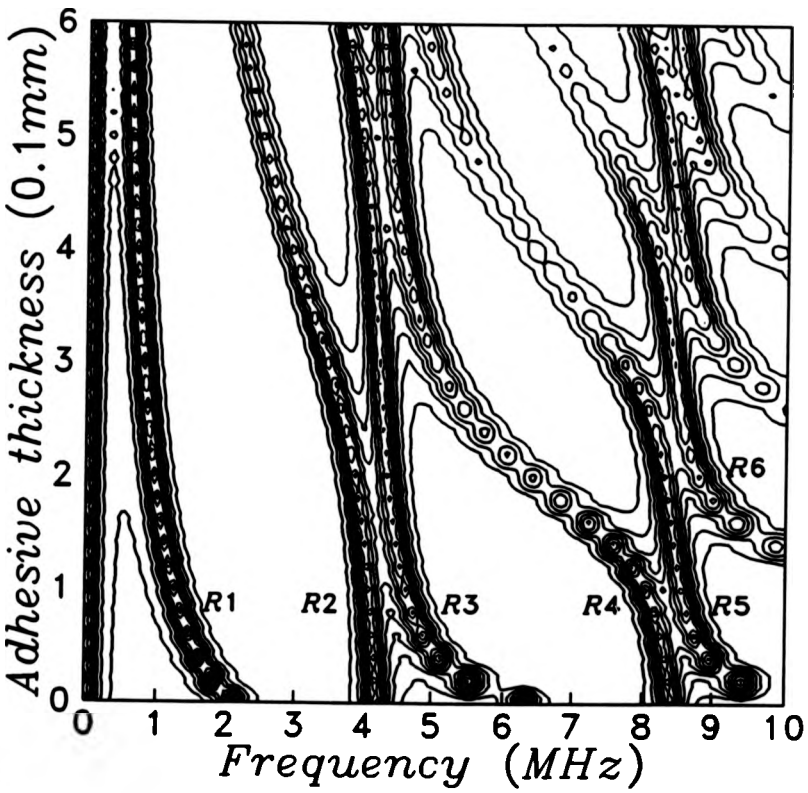

Figure 2.12 Three dimensional contour plot showing the predicted change in the reflectivity spectra with adhesive thickness for a lap joint

is that (at least for small adhesive thicknesses) the model predicts pairs of resonances, one with the epoxy under strain and the other not. Thus when an experimental comparison is made between these resonances, and as only one of these resonances will be dependant on the state of the adhesive, information pertaining to the condition of the bond might be extracted, leading to a possible nondestructive test method for adhesive bonds. This is particularly pertinant when normal incidence shear waves are considered, as areas of poor bond might show partial slippage, which would affect the second of the pair more than the first, and thus it is hoped that this work can help in the search for a valid ultrasonic technique for nondestructive testing of adhesive bonds.

The computer program predicts the reflection and transmission spectra of both longitudinal and shear waves, and the above analysis of resonant modes for longitudinal waves is equally relevant to shear waves. The predicted shearwave reflection spectrum for a bond with no adhesive is shown in Figure 2.13, and the predicted shear wave reflection spectrum for a bond with 0.1mm of adhesive is shown in Figure 2.14. It is seen that the trend for the initial pairing of resonances occours again at the bottom of this diagram (for very small adhesive thicknesses), but occurs much more rapidly than in the case for the longitudinal waves. This is because the wavelength of the shear waves is around half of that for longitudinal waves.

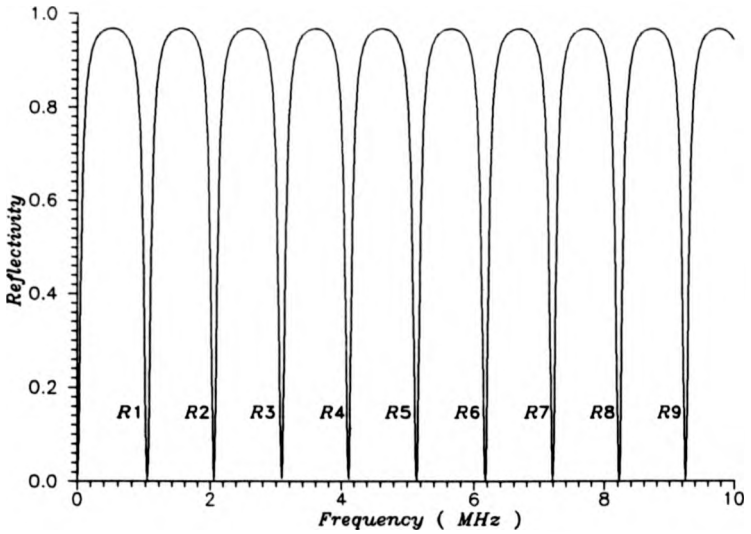

Figure 2.13 Predicted frequency response of an adhesively bonded lap joint to shear waves, the joint having 0.754mm aluminium adherends and no adhesive layer

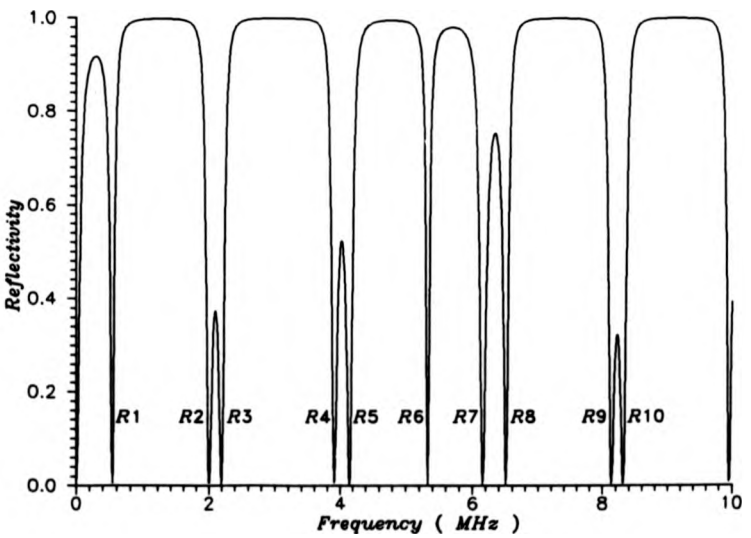

Figure 2.14 Predicted frequency response of an adhesively bonded lap joint to shear waves, the joint having 0.754mm aluminium adherends and 0.1mm of epoxy adhesive

2.6 References

1. W.A.Lees, "Adhesives for composite joints", in "Bonding and repair of composites", Metropole hotel, NEC, Birmingham, U.K., Pub.: Butterworths, 14.7.89, pp. 17-26.
2. R.D.Adams and P.Cawley, "A review of defect types and nondestructive testing techniques for composites and bonded joints", NDT International, 21 (4), 1988, pp.208-222
3. J.A.G.Temple, "Inspection of adhesive joints: a review", AEA industrial technology report, March 1992, AEA Technology.
4. R.J.Freemantle, T.Alper and R.E.Challis, "A broad band technique to simultaneously measure the compression and shear acoustic wave velocities in thin samples of engineering samples", Ultrasonics International 1993 conference proceedings, pp. 291-294.
5. R.P.Cocker and R.E.Challis, "Automatic algorithms for digital signal processing to characterise the propagation of ultrasound in thin adhesive layers", Ultrasonics International 1993 conference proceedings, pp. 299-302.
6. H.L.M.Dos Reis, L.A.Bergman and J.H.Bucksbee, "Adhesive bond strength quality assurance using the acousto-ultrasonic technique", Brit. J. of NDT, 28, (1986) pp.357-358
7. A.Fahr and S.Tanary, "Nondestructive examination of adhesively bonded joints", Impact of emerging NDE-NDI methods on aircraft design manufacture and maintenance, Brussels, (Belgium), 1-6 Oct. 1989, pp. 7.1 - 7.10

8. G.M.Light and H.Kwun, "Review of NDE methodology of adhesive bond strength determination", NDE of adhesive bonds and bondlines, topical proceedings, Oct 9-13, 1989, Valley Forge, PA. pp.7-23

9. H.Lamb, Proc. Roy. Soc. Lond. A93, 114 (1917)

10. J.W.S.Rayleigh, Proc. Lond. math Soc. 17, 4 (1887)

11. R.Stonely, Proc. Roy. Soc. A106, 416 (1924)

12. G.A.Georgiou, A.M.Lank and I.Munns, "Mathematical modelling of ultrasonic wave propagation in adhesively bonded joints", submitted to the proceedings of the 20th Annual review of progress in QNDE, (1-6 Aug. 1993), Brunswick, Maine, U.S.A.

13. P.Cawley, "Low frequency NDT techniques for the detection of disbonds and delaminations", Brit. J. NDT, 32 (9), 1990, pp. 454-461

14. E.P.Papadakis, "Ultrasonic impulse-induced-resonance utilising damping for adhesive disbond detection", Mat. Eval., 36 (1), 1978, pp. 37-40

15. W.N.Reynolds, "Inspection of laminates and adhesive bonds by pulse-video thermography", NDT International, Vol. 21, No.4, pp. 229-232

16. V.I.Neeley, "Ultrasonic holography: a real time NDT method for inspection of adhesive bonds", applied polymer symposia (19), Hoboken, New Jersey, Aug. 23-25, 1972, pp. 451-461

17. M.V.Rao, R.Samuel and K.Ramesh, "Dual vacuum stressing technique for holographic nondestructive testing of honeycomb sandwich panels", NDT International, 23 (5), pp. 267-270

18. B.P.Holownia, "NDE method using electronic speckle pattern interferometry", NDE of adhesive bonds and bondlines, ASNT Topical

proceedings, Valley Forge, Pennsylvania, 9-13 Oct, 1989, pp. 98-100

19. H.Fagot et al, "Holographic NDT of materials using pulsed lasers", Institut Franco-Allemand de recherches de Saint-Louis, Report No. CO 223/80

20. R.A. Kline, C.P. Hsaio and M.A. Fidaali, "Nondestructive evaluation of adhesively-bonded joints", Trans. ASME 41081, 214-217 (1986).

21. J.Schrijve, "Investigation of the ultrasonic testing of glued metal joints", Netherlands aerospace Lab., report No. M-1995, (1955)

22. R.D.Adams and P.Cawley, "Vibration techniques in nondestructive testing", in research techniques in nondestructive testing, Vol. 8 (R.S.Sharpe, Ed. Academic press, N.Y., 1985) pp. 303-360

23. C.C.H. Guyott, P. Cawley, "Evaluation of the cohesive properties of adhesive joints using ultrasonic spectroscopy", NDT International 4211, 233-240 (1988).

24. C.C.H. Guyott, P. Cawley, "The ultrasonic vibration characteristics of adhesive joints", J. Acoust. Soc. Am., 4831, 632-640 (1988).

25. L.M. Brekhovskikh, "Waves in layered media", 2nd edition (Academic Press, N.Y., 1980).

26. E.I Madaras, W.P. Winfree, B.T. Smith and J.H. Heyman, "Detection of bondline delaminations in multilayer structures with lossy components", Proc. 1987 IEEE Ultrasonics Symposium (Denver, Colorado, 1987), pp. 1047-1052.

27. D.A. Hutchins, L.F.Bresse and D.R. Billson, "Resonance studies of bonded aluminium joints", Nondestr. Test. Eval., Vol 10, 1993. pp. 149-165.

28. W.T.Thompson, "Transmission of elastic waves through a stratified solid material", J. Appl. Phys., **21**, (1950), pp. 1215-12221.

29. L.F.Bresse, M.Sc. Thesis, Queens University, Canada. (1987)

CHAPTER 3

ULTRASONIC TESTING OF ADHESIVE BONDS: EXPERIMENTS, RESULTS AND CONCLUSIONS

3.1 Introduction

The last chapter served as an introduction to nondestructive testing of adhesive bonds. The types and usage of adhesive bonds deployed in modern structures, the defects associated with these bonds, the techniques used to identify them, and the capabilities and limitations of the techniques were all discussed. Following this, a nondestructive testing technique, known as ultrasonic spectroscopy, was described in more detail, and a computer program was described that could predict the frequency spectrum of a broadband ultrasonic wave (longitudinal or shear) that had either reflected from, or passed through an adhesive lap joint. This was then used to predict the reflected ultrasonic frequency spectrum for adhesive bonds with varying adhesive thicknesses; this in turn was used to explain the origins of the peaks, or resonances found in the spectra. Finally, it was explained why it was thought that this technique could be useful for the nondestructive testing of adhesive bonds.

This chapter develops from the last by verifying initially that the frequency spectra predicted by the computer program can be observed experimentally. This is first demonstrated using piezoelectric transducers on a range of samples, and is then expanded by applying non-contacting ultrasonic transduction methods such as laser-EMAT techniques and new couplant-free probes to generate the frequency spectra being investigated.

Following this, the spectra from bonds which have been manufactured to include a range of artificial defects were analyzed to determine the ability of the technique to test for these defects. The results obtained ultrasonically were then compared with the final tensile failure strengths of the bonds under test.

The final part of this chapter describes experiments that were undertaken to apply this technique to the testing of adhesively bonded samples whilst they were being pulled to destruction.

3.2 Experiments with piezoelectric transducers

3.2.1 Test Specimens

Prior to any practical experimental work on adhesive bonds, test specimens had to be obtained which could be modelled, ultrasonically tested, and in some cases, destructively tested. These were obtained from two sources; Alcan Ltd and TWI (formerly The Welding Institute). All of the samples were in the form of lap joints of bonded aluminium, the samples from Alcan having a variety of adhesive thicknesses. The samples from TWI were manufactured to include a number of artificial defects, and were made to be suitable for destructive shear tensile tests.

3.2.2 Longitudinal wave immersion testing of adhesive bonds with varying adhesive and adherend thicknesses

The samples from Alcan ltd. were ultrasonically tested in pulse-echo mode in a water bath. This was done with a Panametrics 5MHz piezoelectric immersion probe (type V309), using a Panametrics Pulser/receiver (type 5055PR), a Tektronix 2430A digital oscilloscope, and an IBM 30-236 computer. The Fourier transforms of the waveforms produced in this way produce a frequency spectrum. This was then compared with the reflection spectrum predicted for the bond by the computer program described in the previous chapter. The samples had aluminium

adherends that were either 1.613mm or 0.754mm thick, with adhesive thicknesses ranging from 0.190mm to 0.912mm.

A waveform from a sample with 0.754mm adherends and a 0.339mm thick adhesive layer is given in Figure 3.1. The waveform appears to be complicated, and by observing the waveform in this form, no information pertaining to the state of the bond can be readily deduced. The Fourier transform of this waveform, however (shown in Figure 3.2), shows distinct resonances at 3.15, 4.22 4.71 and 8.4 MHz.

The spectrum predicted for this sample (using the computer program described in chapter 3 of this thesis) is shown in Figure 3.3. This shows a series of resonances at about the same frequencies as were observed for the experimental results, but the overall shape of the spectra are quite different. This is mainly because the computer model assumes an "ideal" broadband incident ultrasonic pulse (a Dirac function), which cannot be achieved in practice, as the frequency response of the transducer is finite[1,2]. The frequency response of the transducer used in these experiments is shown in Figure 3.4, which was obtained by performing a Fourier transform of the waveform obtained using the transducer on the first reflection from a thick flat aluminium plate. To incorporate the finite bandwidth of the transduction system into the model, the spectrum predicted by the computer (Figure 3.3) must be multiplied by the frequency response of the transducer (Figure 3.4). This then gives the frequency spectrum shown in Figure 3.5.

It can be seen that after incorporating the frequency response of the transducer, the predicted frequency spectrum (Figure 3.5) compares well with the

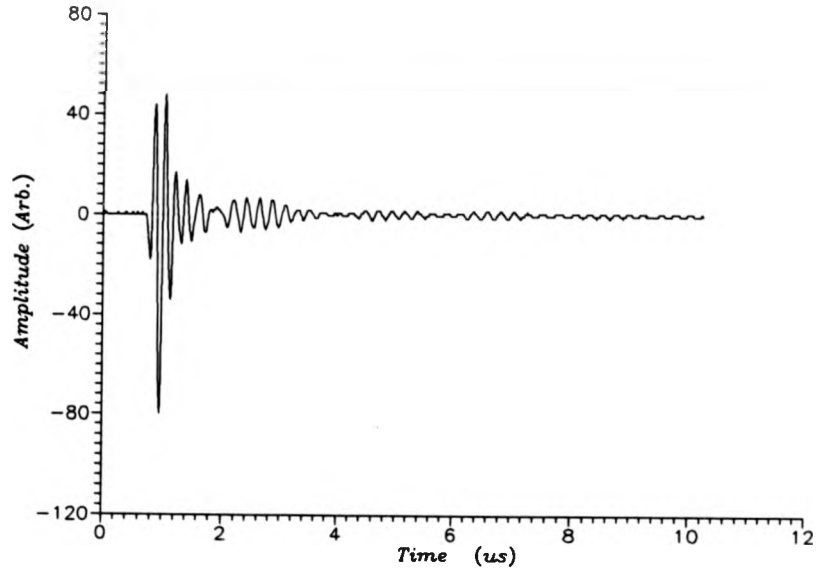

Figure 3.1 The immersion pulse-echo waveform from a sample with 0.754mm adherends and 0.339 mm adhesive

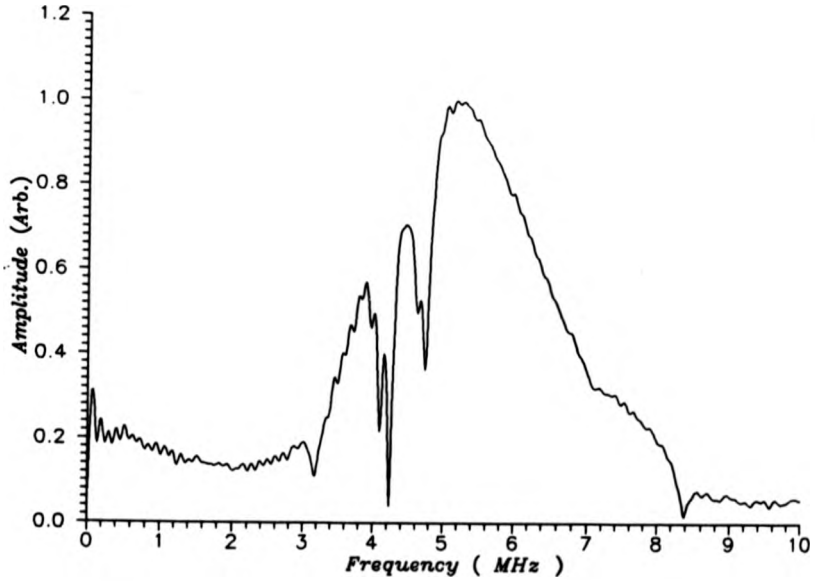

Figure 3.2 The Fourier transform of the waveform shown in Figure 4.1

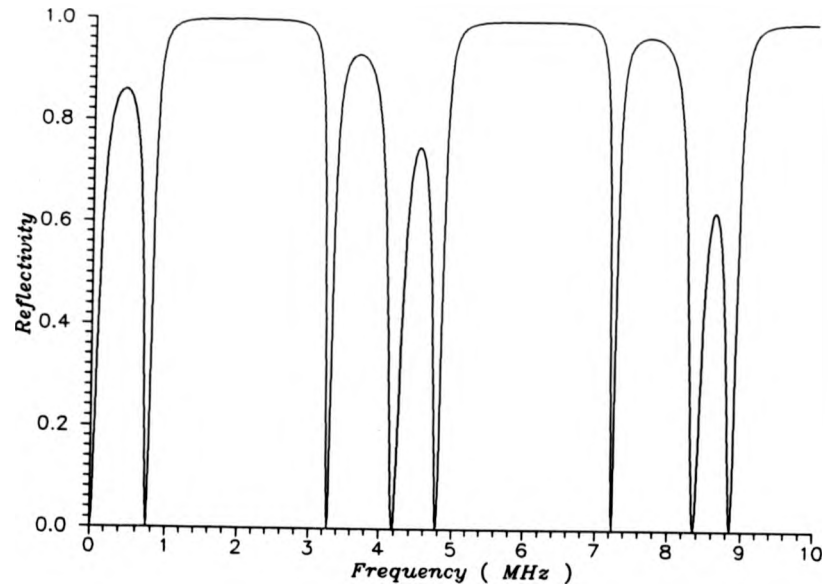

Figure 3.3 The predicted frequency response of the adhesive bond to a broad band ultrasonic pulse

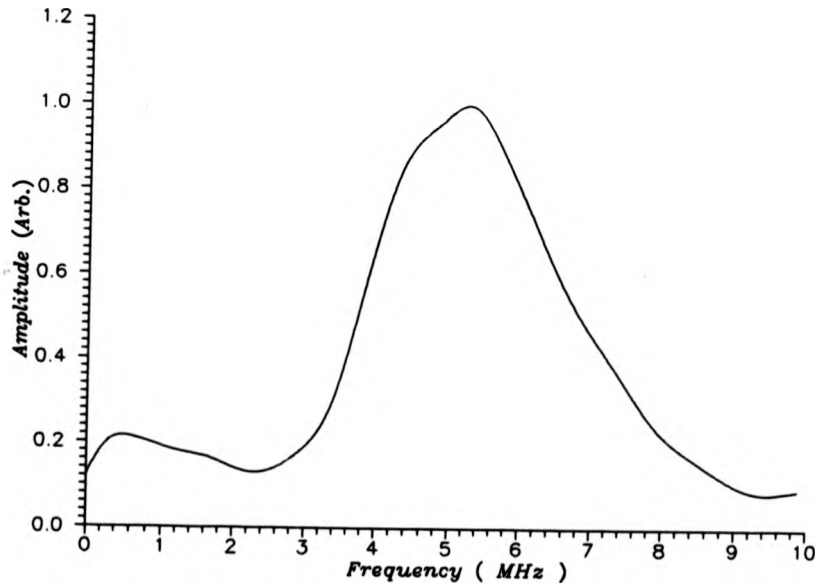

Figure 3.4 The frequency response of the piezoelectric transducer

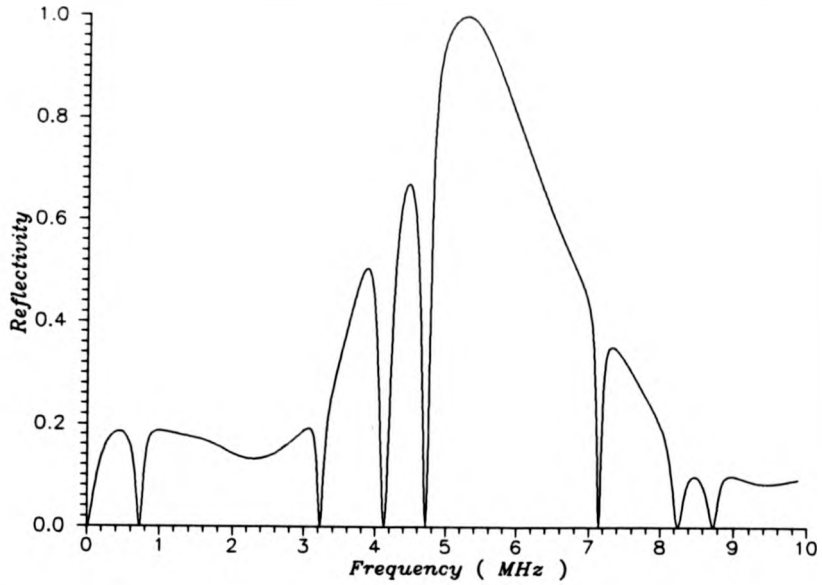

Figure 3.5 The frequency response of the bond to the ultrasonic pulse

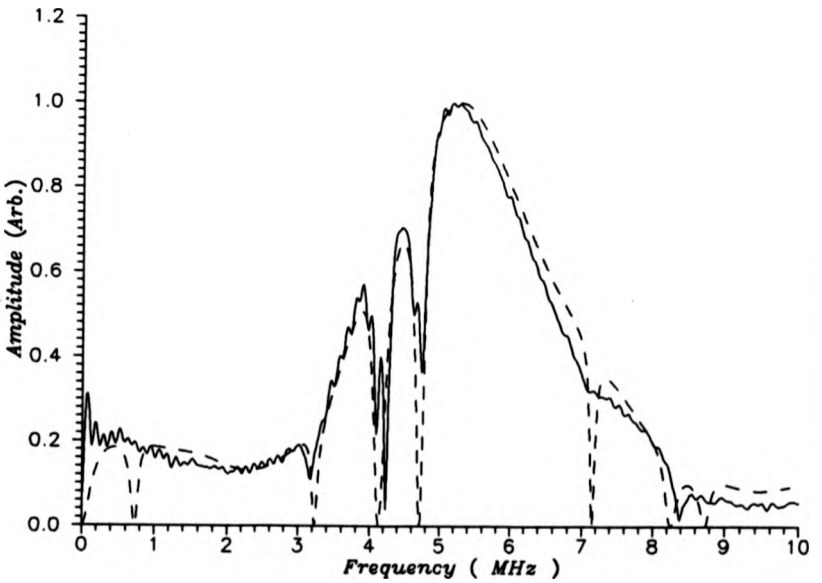

Figure 3.6 Comparison between the experimentally measured (solid line) and the predicted (dashed line) frequency spectra

experimental spectrum (Figure 3.2). This is more easily illustrated by Figure 3.6, where the two spectra are shown superimposed upon each other, with the theoretical plot being the dashed line. The positions of the predicted peaks match well with each other, though any slight discrepancy might be attributed to errors in the value of the epoxy velocity used in the computer model. (The ultrasonic velocity of epoxy adhesives is notoriously difficult to predict, as has been reported in the literature[3]). The amplitudes of the resonances in the predicted (dashed) plot are seen to approach zero at resonance, which is not seen in the experimental plot. This is thought to be due to the effect of attenuation in the adhesive layer. This is easily incorporated into the computer program by assigning an imaginary component to the velocity of sound in the adhesive layer, and the effect can be seen in Figure 3.7, where a complex value of $-100i ms^{-1}$ has been incorporated into the longitudinal velocity in the adhesive. Here, the predicted plot is seen to be much closer to the measured frequency than was observed in Figure 3.6. It is important to note that certain resonances are affected by this attenuation much more than others. This can be seen in the predicted plots when Figures 3.6 and 3.7 are compared. The resonance at 7.1MHz is seen to be greatly reduced by the affect of attenuation, whereas the resonance at 4.1MHz is not. This can be explained by the theory presented in Chapter 2 of this thesis, where certain modes have the ultrasonic energy (strain) concentrated in the adhesive layer, and others have it concentrated in the adherends. It is thought that a technique which observes the resonances that are greatly affected by the adhesive layer, and compares them with the resonances that are not, could form the basis of a technique that might be used to analyze the integrity of the adhesive-adherend

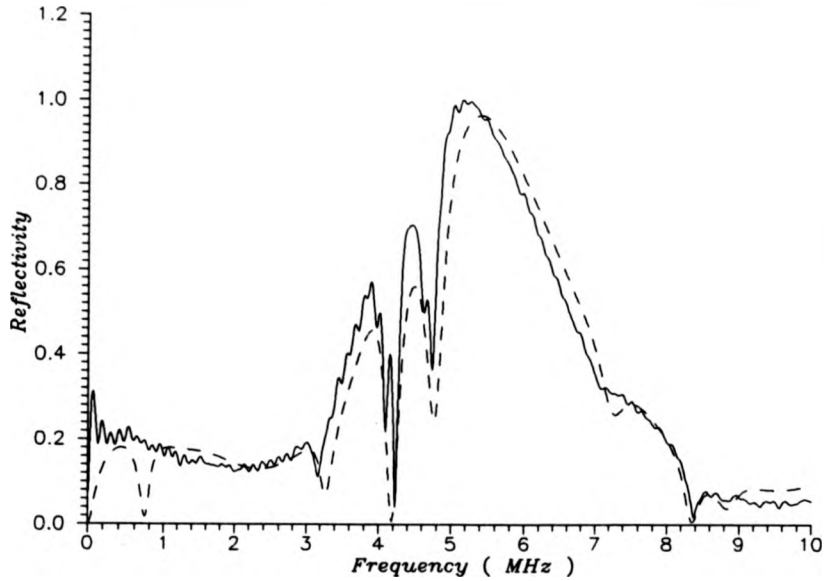

Figure 3.7 Comparison between experimental (solidline) and predicted (dashed line) frequency spectra, allowing for attenuation

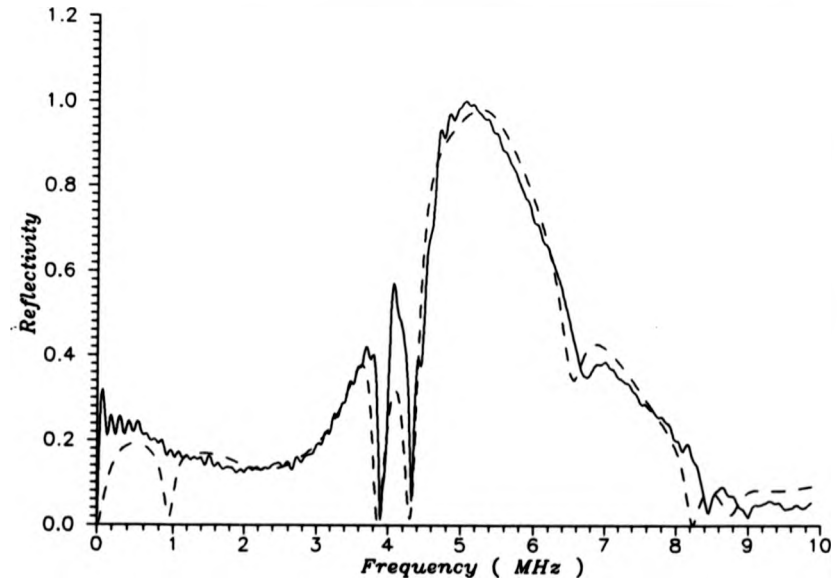

Figure 3.8 Comparison between experimental (solid line) and predicted (dashed line) frequency spectra for a sample with 0.754mm adherends and 0.190mm adhesive

interface.

The ultrasonic frequency spectra from a variety of adhesive bonds was both modelled and measured experimentally. Figure 3.8 shows a comparison between the predicted and the experimental spectra from a bond with 0.754mm thick adherends, and a 0.19mm thick adhesive layer. As with the previous example, the theory and the experiment are seen to be in excellent agreement. This Figure appears at first glance to be very similar to Figure 3.7, (as might be expected with the small change in adhesive thickness), but the resonances have in fact moved considerably. By decreasing the thickness of the adhesive layer from 0.339 to 0.190mm, the resonance at 3.2MHz in Figure 3.7 (an R2 resonance), has moved to 3.85MHz in Figure 3.8. The next resonance (an R3 resonance at 4.2MHz in Figure 3.7, and at 4.3MHz in Figure 3.8) has not moved much, which is in contrast to the next resonance (an R4 resonance), which has moved from 4.8MHz to 6.5MHz. This shows that the frequency spectra produced using this technique are very sensitive to changes in adhesive thickness (which is shown in Figure 3.12 of the last chapter).

Figure 3.9 shows a plot from a bond with 1.613mm thick adherends, and a 0.276mm thick adhesive layer. Again the theory and experiment are in excellent agreement, but this spectra appears to be very different to the previous examples. The resonances are seen to be much closer together, which can be explained by considering the increased thickness of the structure (compared to the previous examples), which allows a greater number of modes to exist within it.

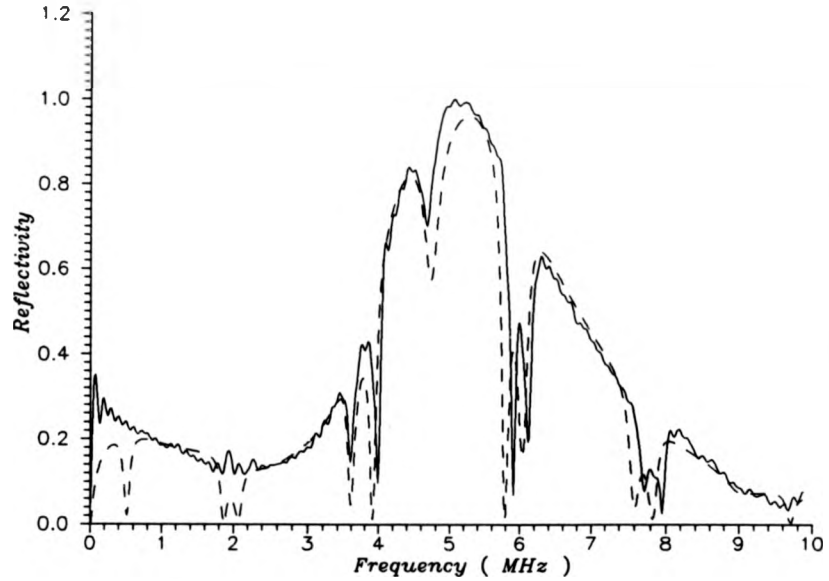

Figure 3.9 Comparison between experimental (solid line) and predicted (dashed line) frequency spectra for a sample with 1.613mm adherends and 0.276mm adhesive

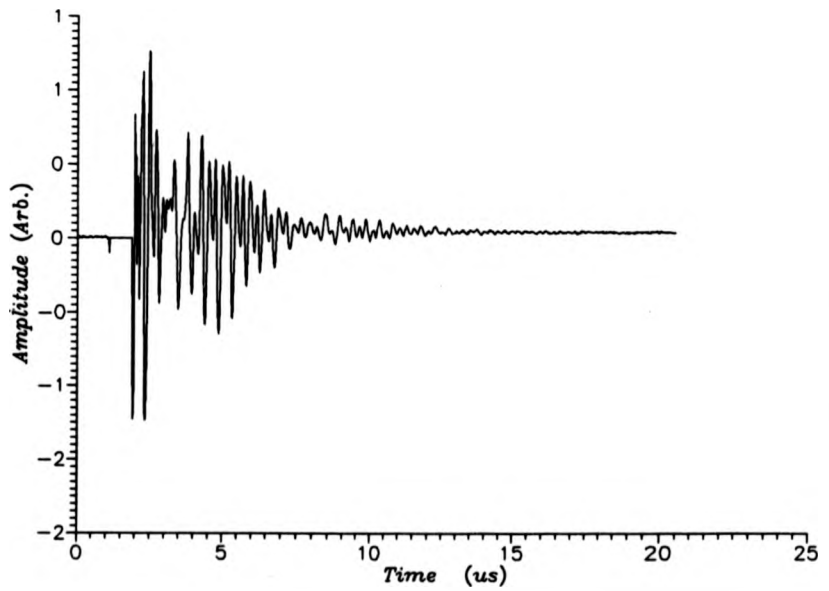

Figure 3.10 The shearwave pulse-echo waveform from a sample with 0.754mm adherends and 0.339mm adhesive

3.2.3 Shear wave testing of adhesive bonds with normal incidence contacting transducers

It was thought that the use of normal incidence, horizontally polarised shear waves (SH-waves) might be useful for the testing of the adhesive-adherend interface. The basis for this is that there should be a greater change between the response of a good interface and a poor interface with tests using a shear stress, rather than a compressive stress (the analysis of "slipping bonds" has been well documented in the literature)[4]. The model and computer program described in the last chapter for longitudinal waves also works for shear waves, and this section of this chapter compares the computer modelled frequency spectrum of a lap joint to shear waves, with the corresponding experimentally obtained spectra. Examples are given only for the reflection case (for conciseness), but it should be noted that the results for transmission were found to be similar.

The shear waveform obtained on a sample with 0.754mm adherends and 0.339mm adhesive is shown in Figure 3.10. This was obtained by directly coupling a normal incidence shearwave transducer to the surface of the joint with a thin layer of honey. The transducer used was a type V154-RB Panametrics broadband hard faced piezoelectric probe, with a diameter of 0.5", and a nominal centre frequency of 2.25MHz. This was driven with a Panametrics pulser-receiver (type 5055PR), and the output connected to a digitising oscilloscope (a Data-Precision DATA6000). The waveforms were subsequently recorded and processed on an IBM 30-286 microcomputer. For the measurements, the transducer was placed directly in contact with the sample, as the addition of a delay line was found to complicate the signal (which was thought to be mainly due to the coupling

between the face of the transducer and the delay line). This arrangement meant that the upper and lower surfaces of the bond were not bounded by an infinite water layer, which is assumed in the computer program, and thus the computer predictions are not strictly correct; however, this was not found to affect the results significantly.

The waveform, as with the longitudinal waveform shown in Figure 3.1, is complicated, and does not appear to show any useful information pertaining to the state of the bond. The Fourier transform of this waveform is shown in Figure 3.11 (the plot with a solid line) which, as with the longitudinal analysis, shows a series of resonances. This can be compared with the predicted reflection spectrum (dashed line) in the same Figure. The positions and relative heights of the resonances appear to be in excellent agreement, however the plots are inverted!. This is because the theory assumes the presence of an initial reflection from the front face of the sample, which could not be detected. The frequency response of the transducer is not incorporated into the modelling, as in this case it was thought that this would only serve to complicate the "inverted" signals. As with the longitudinal spectra, there are resonances with their energy concentrated in the adherends ("adherend resonances"), for example at 4.1MHz, and resonances with their energy concentrated within the adhesive layer ("adhesive resonances"), for example at 3.4MHz. It follows that the adhesive resonances should be most affected by poor adhesive-adherend cohesion. It was hoped that looking at the amplitudes of "adhesive resonances", (after normalising their amplitudes by comparing them to the "adherend resonances") and comparing these between good and bad bonds might form the basis of a useful technique for assessing the

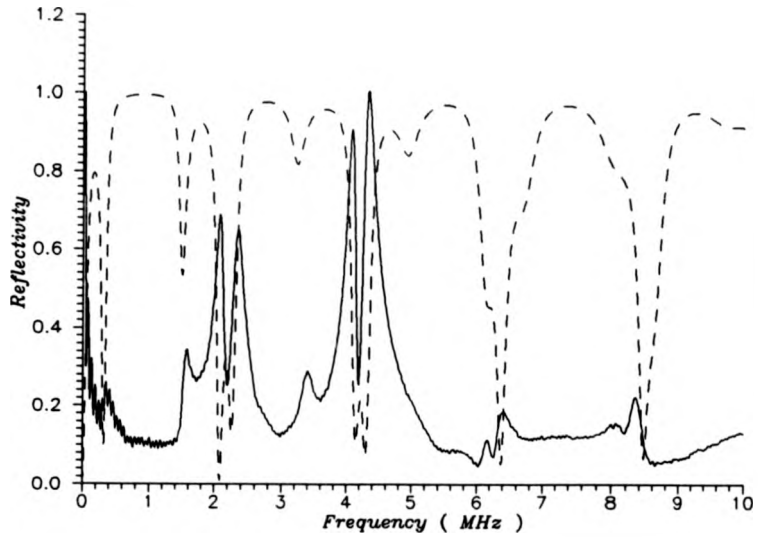

Figure 3.11 Comparison between the shearwave experimental (solid line) and predicted (dashed line) frequency spectra for a sample with 0.754mm adherends and 0.339 mm adhesive

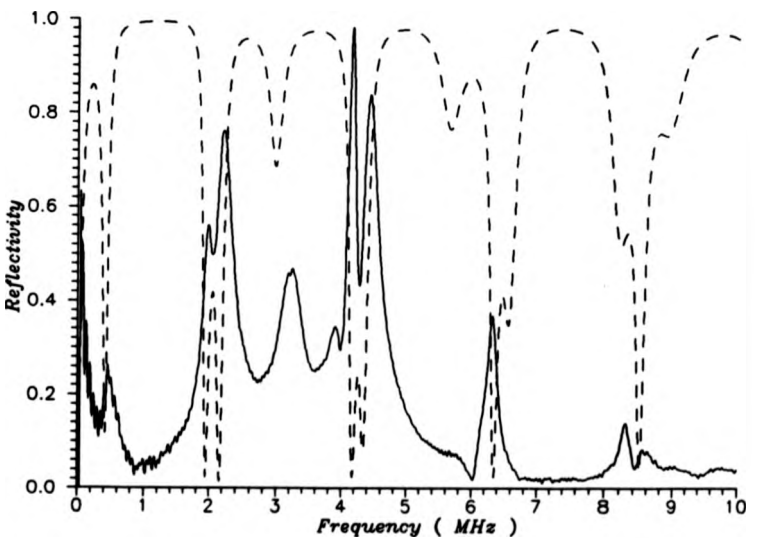

Figure 3.12 Comparison between shearwave experimental (solid line) and predicted (dashed line) frequency spectra for a sample with 0.754mm adherends and 0.190mm adhesive

integrity of bonded structures. The spectrum shown in Figure 3.11 is more complicated than the longitudinal spectrum for the same bond given in Figure 3.8, this is because the wavelength of shear waves is about half that of longitudinal waves, allowing around twice the number of resonances within the same thickness of structure.

A number of adhesive samples were tested with this technique, and the predicted and measured frequency spectra for a bond with 0.754mm adherends and 0.19mm adhesive is given in Figure 3.12. and for a bond with 1.613mm adherends and 0.276mm adhesive in Figure 3.13. As with Figure 3.11, the predicted and measured frequency spectra are in excellent agreement with each other.

3.2.4 Distinguishing between (nominally) good bonds and gross disbonds

Previous workers in the field have already shown that spectroscopic techniques can be used to detect gross disbonds in adhesive bonds[5]. However, for completeness, an example is given of the different frequency spectra from good and bad portions of the same bond (the gross disbond was artificially introduced into the bond at the time of manufacture) to show the differences observed. The time waveforms were taken with a 3.5MHz piezoelectric transducer in immersion, using a Panametrics 5055pr pulser-receiver, a Tektronix 2430A digitising oscilloscope, and an IBM model 30-286 micromputer.

Figures 3.14a and 3.14b represent the time waveforms of the reflection from the good and the bad areas respectively of the adhesive bond. Whilst they appear to be slightly different, the state of the bond cannot readily be assessed

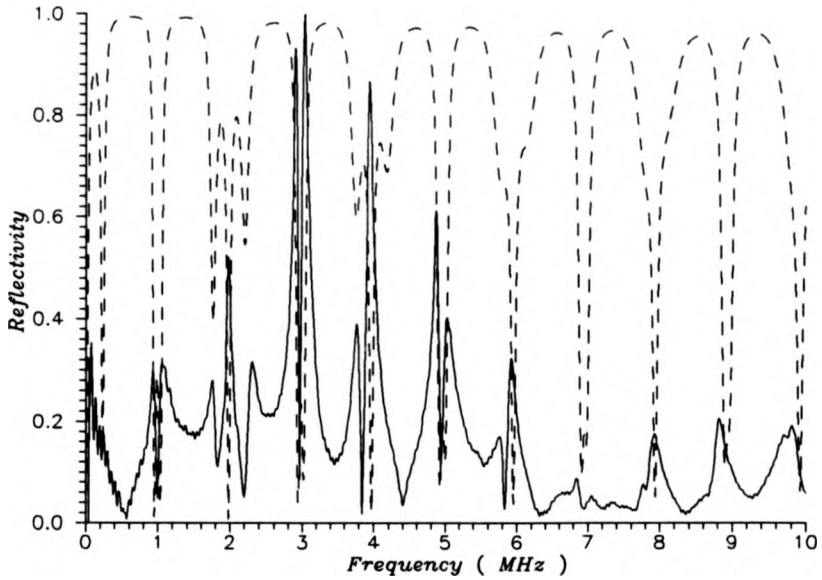

Figure 3.13 Comparison between the shearwave experimental (solid line) and predicted (dashed line) frequency spectra for a sample with 1.613mm adherends and 0.276 mm adhesive

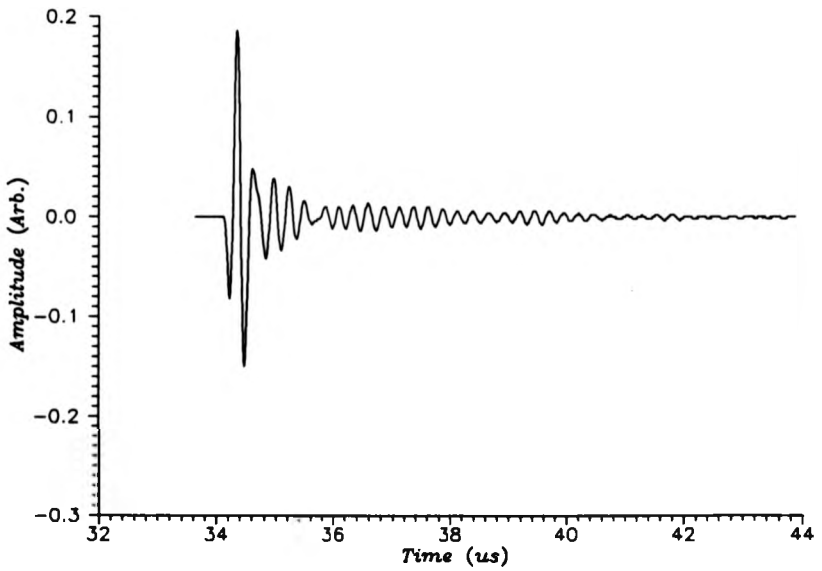

Figure 3.14a Time waveform taken of a nominally good portion of the adhesive bond

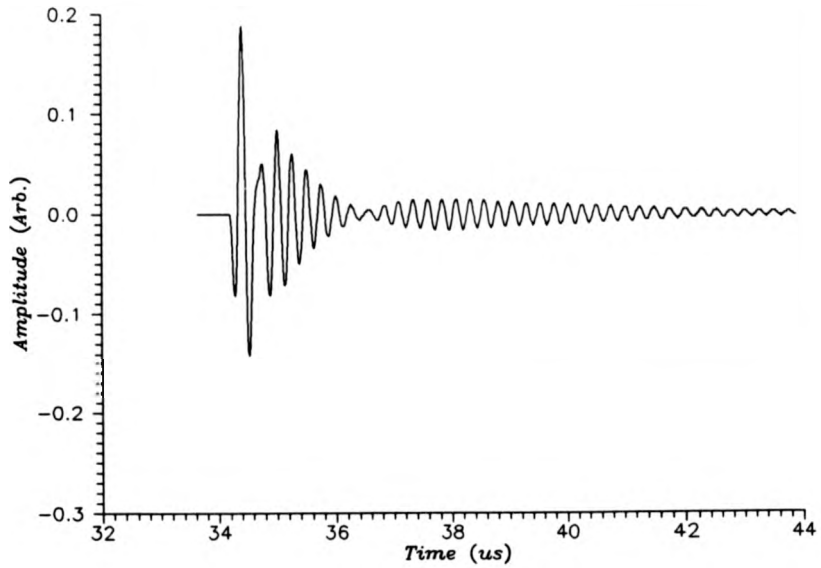

Figure 3.14b Time waveform taken of a nominally bad portion of the adhesive bond

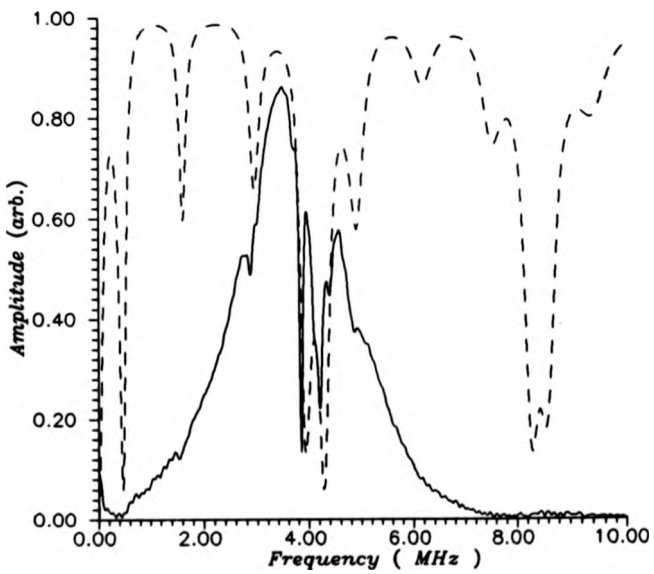

Figure 3.14c A comparison between the predicted (dashed line) and experimentally obtained (solid line) frequency response from a nominally good part of the adhesive bond

from these waveforms alone.

Figures 3.14c and 3.14d show the frequency spectra of these waveforms (solid lines) together with the (dashed) frequency spectra predicted for this bond (although the frequency response of the transducer has not been allowed for here). Figure 3.14c (the spectrum from the good part of the bond) shows excellent correlation between the predicted and the measured peaks, whilst, conversely, Figure 3.14d does not. A number of resonances (notably at 3 and 5 MHz) do not appear, and the pair of resonances around 4MHz in Figure 3.14c seem to have been changed to a single resonance. A comparison between these spectra clearly shows that their observation can be easily used to detect nondestructively gross disbonds in adhesive bonds.

This is a powerful technique, and one that is not widely known about in industry. It is thought that scope exists in developing this technique for industrial exploitation, this will be in the form of developing systems that can analyze the frequency spectra and compare this with the predicted spectra in real time. This should not be difficult with the range of digital equipment and computers available today.

3.3 Non-contacting techniques for obtaining the frequency spectra of adhesive bonds

A number of non-contacting techniques have been used to obtain the frequency spectra of adhesive bonds. This was done to allow the application of the spectroscopy technique to structures where conventional contacting (piezoelectric) transducers could not be used, for example where the structure is at an elevated

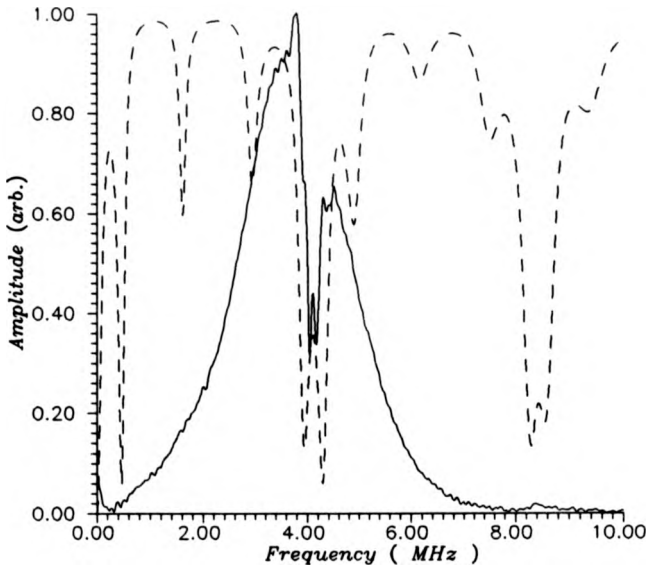

Figure 3.14d A comparison between the predicted (dashed line) and experimentally obtained (solid line) frequency response from a nominally bad part of the adhesive bond

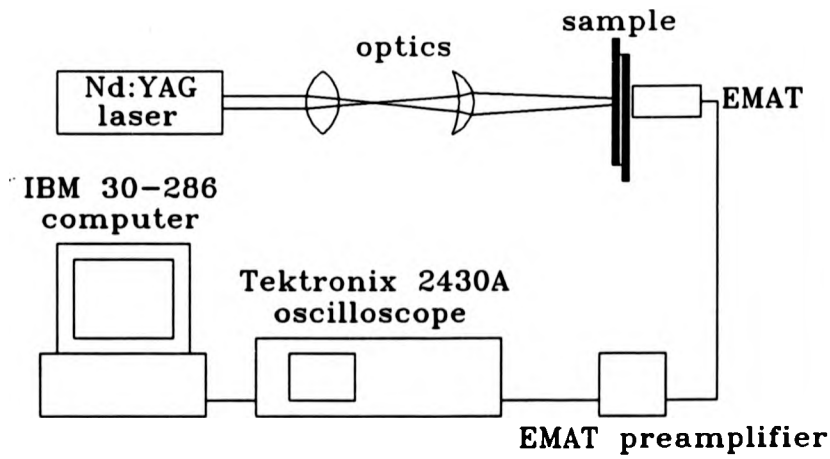

Figure 3.15 Schematic diagram of the apparatus used to collect the data for the laser-EMAT experiments in through-transmission.

temperature, or where the application of a couplant might contaminate the surface of the structure.

3.3.1 Laser - EMAT experiments at room temperature

(a) Apparatus and experiment

A schematic diagram of the apparatus used to collect the data in through-transmission is shown in Figure 3.15. This shows that the laser beam was directed through a series of optical elements on to the surface of the bonded lap joint to generate the ultrasound, and the EMAT was placed on the opposite side of the sample to detect the ultrasound. The signals from the EMAT were amplified using a specially-constructed wideband amplifier, (based around a ZN459-CP low-noise operational-amplifier, described more fully in chapter 5 of this thesis), and were then digitised using a Tektronix 2430A digital oscilloscope, and finally transferred to an IBM Model 30-286 computer for analysis and storage.

It was decided to investigate non-contacting techniques for testing adhesive bonds using a pulsed Nd:YAG laser to provide an ultrasonic source, and an electro-magnetic acoustic transducer (EMAT) as a receiver. Experiments were performed on the same samples that were investigated with the piezoelectric transducers, as described in section 3.2 of this thesis.

The laser source was a Q-switched Nd:YAG laser which provided single pulses of 4ns duration, at energies of up to 120mJ. The laser was operated to generate preferentially, either shear waves (by a thermoelastic mechanism), or longitudinal waves (by an ablative mechanism). The theory behind these mechanisms was described earlier in chapter 2 of this thesis.

Three EMATs were used as ultrasonic receivers in these experiments; two were designed to optimise the reception of longitudinal waves (one was for the pulse-echo mode, and the other was for the through-transmission mode), and the third was optimised for the reception of shear waves (in through-transmission mode). The EMATs for the longitudinal wave investigations needed to maintain a magnetic field parallel with the sample surface, and used mild steel pole pieces with a permanent magnet to achieve this (a "magnetic circuit" was completed). The coils for these EMATs were wound around brass formers placed between the pole pieces, resulting in the transducers having their "active areas" in a line. The pulse-echo longitudinal experiments used one of these EMATs that was designed to allow the laser beam to pass through an aperture in the centre of it, This is shown in Figure 3.16. The EMAT used to receive shear waves at normal incidence needed a magnetic field normal to the sample surface, which was easily achieved with a permanent magnet. This design of EMAT used a "pancake" coil wound on top of the magnet to produced a detector that was sensitive to radially polarised shear waves. The theory behind the operation principles of EMATs was described more fully in chapter 2 of this thesis.

(b) Results

Consider first the through-transmission results obtained with the laser configured to generate preferentially, and the EMAT configured to receive preferentially longitudinal waves.

The first adhesively bonded sample tested was a lap joint with a 0.339mm thick adhesive layer between 0.754mm aluminium adherends. The ultrasonic time-

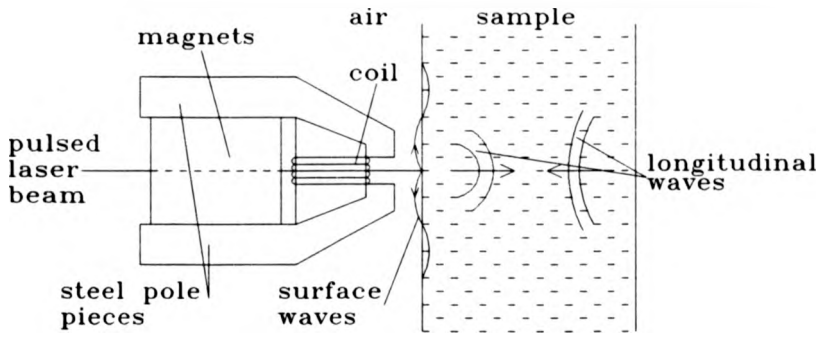

Figure 3.16 Schematic diagram of an EMAT developed for the testing of adhesive bonds using longitudinal waves in pulse-echo.

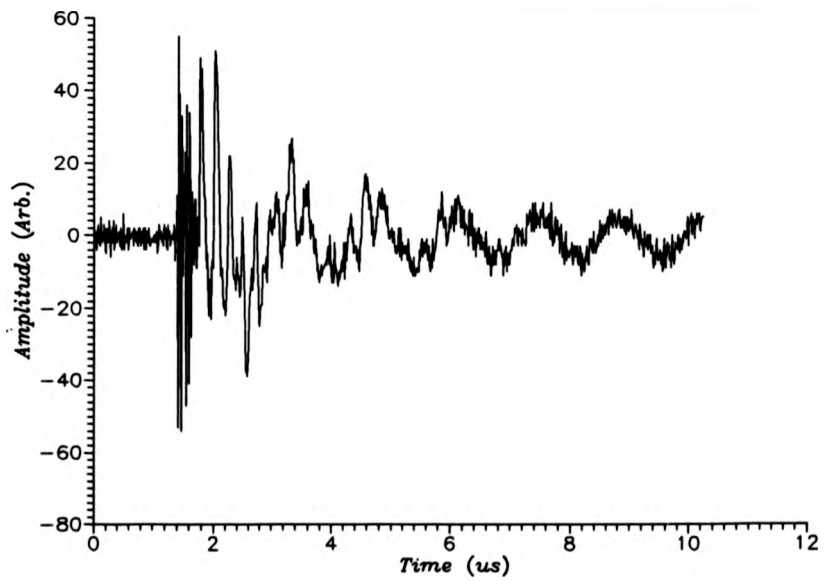

Figure 3.17a The time waveform from an adhesive bond with 0.754mm adherends and 0.339mm adhesive layer, longitudinal laser-EMAT in through transmission.

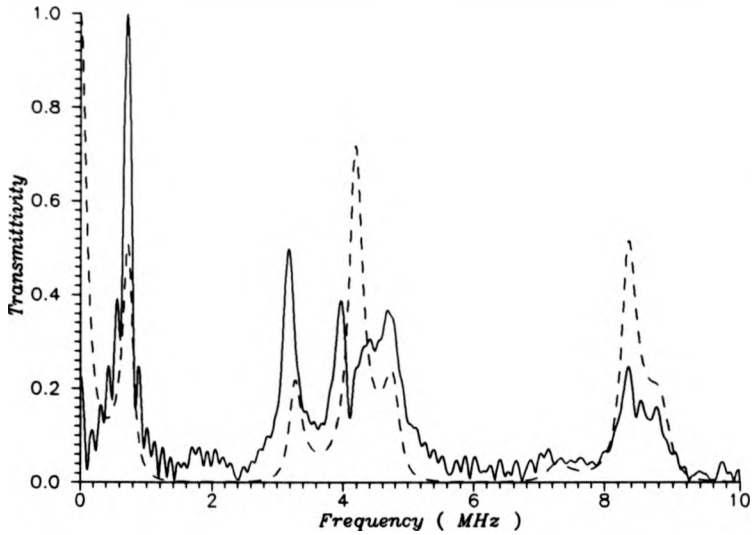

Figure 3.17b The predicted transmission frequency response of an adhesive bond to longitudinal wave ultrasound (dashed line) compared to the spectra experimentally obtained (solid line) with a laser source, and an EMAT receiver

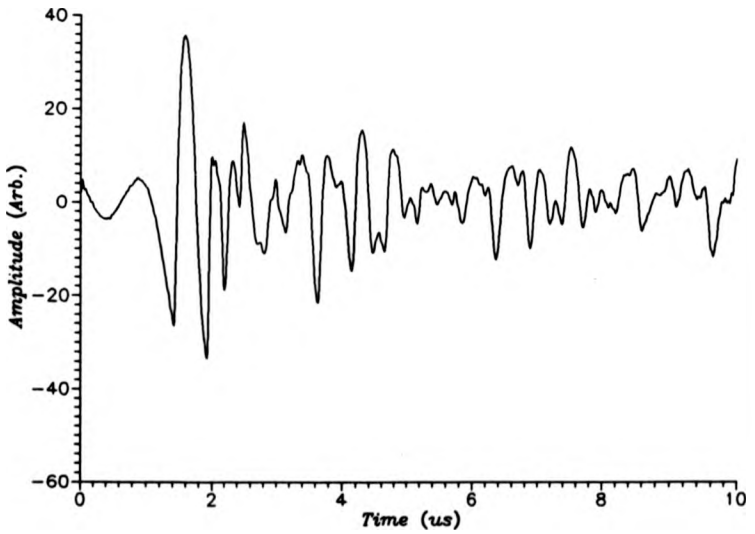

Figure 3.18a The time waveform from an adhesive bond with 1.613mm adherends and 0.276mm adhesive layer, longitudinal laser-EMAT in pulse-echo.

waveform obtained with this method is shown in Figure 3.17a, and the frequency spectrum of this (the Fourier transform) is shown in Figure 3.17b. As with the previous results, the time waveform is highly complicated, and no meaningful information can be derived from this intuitively. However, the frequency spectrum of this (shown as the solid line in Figure 3.17b), shows a series of resonances that correspond well with the predicted resonances (the dashed line). It should also be noted that, whilst the derived frequency spectrum is more noisy than that obtained using the piezoelectric transducers, this transduction system has a wider response over a the bandwidth investigated (0-10 MHz).

The next experimental configuration that is considered is as above, but with the EMAT detector now placed on the same side of the sample as the incident laser beam (in a pulse-echo mode). The EMAT used for this experiment was shown in Figure 3.16. This shows the laser generating both longitudinal waves (propagating within the sample), and surface waves (propagating at the surface of the sample, and duly passing underneath the EMAT). These surface waves resulted in unwanted signals which were superimposed on the signals of interest. Fortunately, these were generally of a lower frequency than the spectral features of interest from bonded joints, and much of this noise was removed by slight alterations to the preamplifier (the input was capacitively decoupled, which, together with the resistor used to match the input impedance of the EMAT to the preamplifier formed a simple high pass filter).

The ultrasonic time waveform that was obtained with this setup on the sample with 1.613mm aluminium adherends, and 0.276mm adhesive is shown in Figure 3.18a, and the corresponding frequency spectrum (together with the

spectrum predicted for this sample, shown as the dotted line) in Figure 3.18b. This spectrum is seen to be inverted relative to the predicted reflection spectrum, which is thought to be due to the initial part of the waveform being lost in noise from the laser pulse, causing an effect similar to that observed with the contacting shearwave transducer (seen in Figure 3.13). This spectrum is also seen to be rather noisy when compared to previous spectra, although resonances are still clearly discernable above 3MHz which compare well with those predicted by theory. It is thought that some of the noise below 3MHz might be due to both surface waves, and geometrical effects.

The time waveform and frequency spectrum obtained using a shear wave EMAT as a receiver and thermoelastic generation by the laser, (in through-transmission) on a sample with 1.613mm adherends, and 0.276mm adhesive, are shown in Figures 3.19a and 3.19b respectively. Above 2.5MHz, the frequency spectrum shows maxima as a series of peaks with positions that correspond well with those in the predicted spectrum. Below 2.5MHz, however, they do not. The cause of this is not understood, though it is thought that this effect may be caused either by mode conversions, or by geometric effects resulting from the receiving pancake coil being displaced around the source.

(c) Conclusions

These experiments have shown that laser-EMAT techniques are applicable to the testing of adhesive bonds with both longitudinal and shear waves, though the quality of the frequency spectra are not generally as good as those obtained with piezoelectric transducers. At low frequencies, (below 3MHz) these techniques

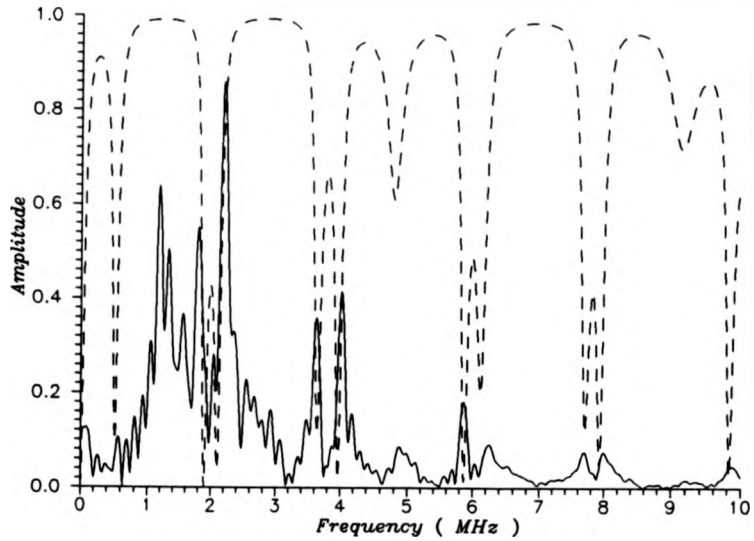

Figure 3.18b The predicted transmission frequency response of an adhesive bond to longitudinal wave ultrasound (dashed line) compared to the spectra experimentally obtained with a laser source, and an EMAT receiver in pulse-echo mode

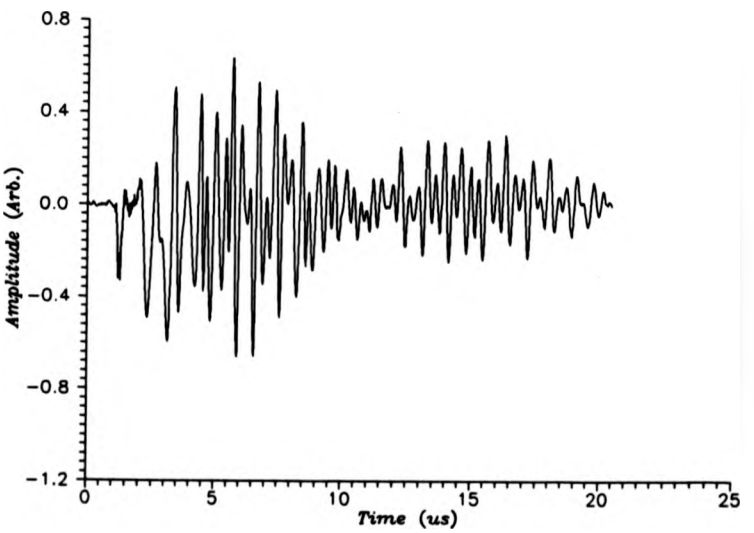

Figure 3.19a The time waveform fron an adhesive bond with 1.613mm adherends, and 0.276mm adhesive layer, shear wave EMAT in through transmission.

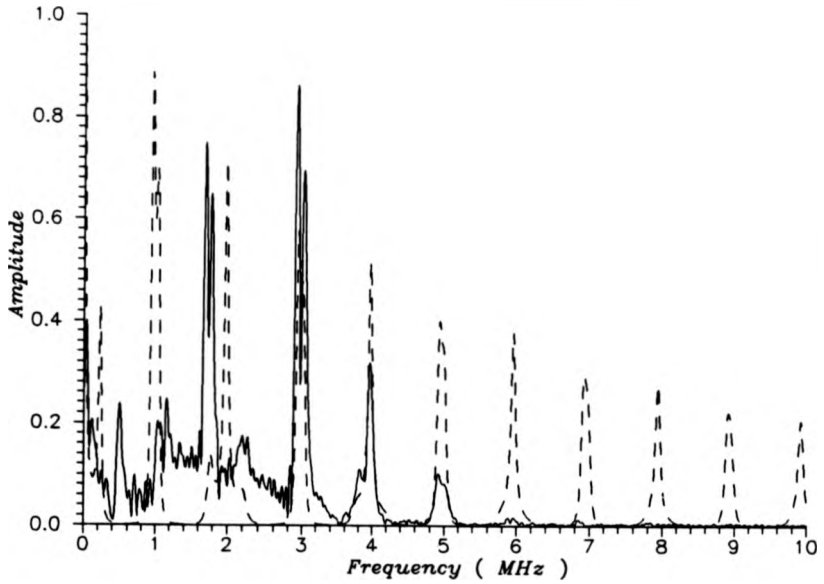

Figure 3.19b The predicted transmission frequency response of an adhesive bond to shear waves (dashed line) compared to the spectra experimentally obtained with a laser source, and an EMAT receiver in through-transmission mode.

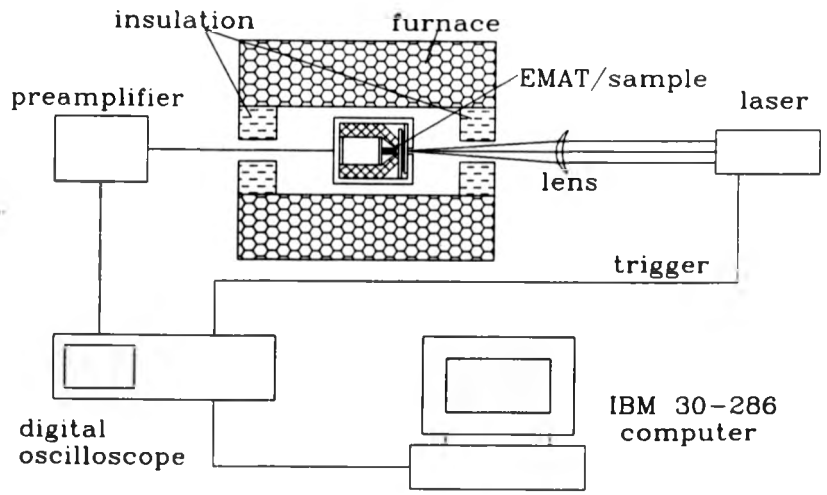

Figure 3.20 The experimental configuration to ultrasonically test adhesive bonds at elevated temperatures.

have been shown to exhibit difficulties, but the spectra are clear enough to tell that a bond is still complete (the spectra would be completely different for a gross defect, such as a complete disbond).

3.3.2 Experiments at elevated temperatures

To show that the non-contacting techniques could be used with the spectroscopic technique to monitor the state of an adhesive bond in a situation where conventional transducers could not be employed, an adhesively bonded sample was heated beyond its failure point in a furnace, with ultrasonic waveforms being taken as the temperature of the sample was increased.

The laser source was again a Q-switched Nd:YAG laser which provided single pulses of 4ns duration, at energies of up to 120mJ. The laser output was configured to generate longitudinal waves preferentially (by an ablative mechanism). The receiver was a longitudinal EMAT that had been developed to operate at temperatures up to 550°C, a more detailed description of this is given in chapter 5 of this thesis. A longitudinal EMAT was chosen over a shear wave EMAT as the signals received were very weak, (a result of both the reduced magnetic field from the high temperature EMAT, and the ultrasonic attenuation of the adhesive layer in the samples) and the shear wave EMAT gave signals that were too weak to easily use.

The samples investigated were prepared by T.W.I. These had 1.6mm aluminium adherends around a 0.25mm thick adhesive layer. The adhesive was a single part toughened epoxy (Permabond ESP110) with a 1% (nominal) addition of ballatini balls to ensure a constant, reproducible adhesive layer thickness.

The experimental setup is as seen in Figure 3.20. The optics focused the beam from the laser down to a spot on the front face of the sample under test, taking great care to ensure that this was directly over the EMAT centre. A waveform was taken at room temperature, averaging over ten shots, and then the furnace was set to heat up. Further waveforms were then taken at regular intervals as the temperature of the sample increased (this was measured by a thermocouple attached directly to the front face of the sample). These waveforms were stored and subsequently processed and analyzed. The room temperature waveform is shown in Figure 3.21a, and the frequency spectrum of this is shown in Figure 3.21b. The time waveform is, as with previous waveforms, highly complicated, but the frequency spectrum of this clearly shows resonances at 1.8, 2.2, 3.6, 4, 6 and 8MHz, which were expected for this bond. As the temperature of the sample increased, similar frequency spectra were obtained from the sample, (though the positions of the resonances changed very slightly, and their amplitude decreased). These resonances continued to be visible up to 260°C, as shown in Figure 3.22a. Whilst the resonances are almost lost in the noise, they are still discernible. At 280°C (Figure 3.22b) no resonances are discernable in the frequency spectrum at all, indicating that the bond had failed catastrophically since the measurement at 260°C.

Before the bond failed, the positions of the peaks changed very slightly, which may be accounted for by the thermal expansion and decrease in ultrasonic velocity in both the aluminium and the adhesive layer (though mainly in the adhesive layer). Both of these effects will increase the ultrasonic transit time across the bond, causing an effect similar to increasing the bond thickness. This is shown

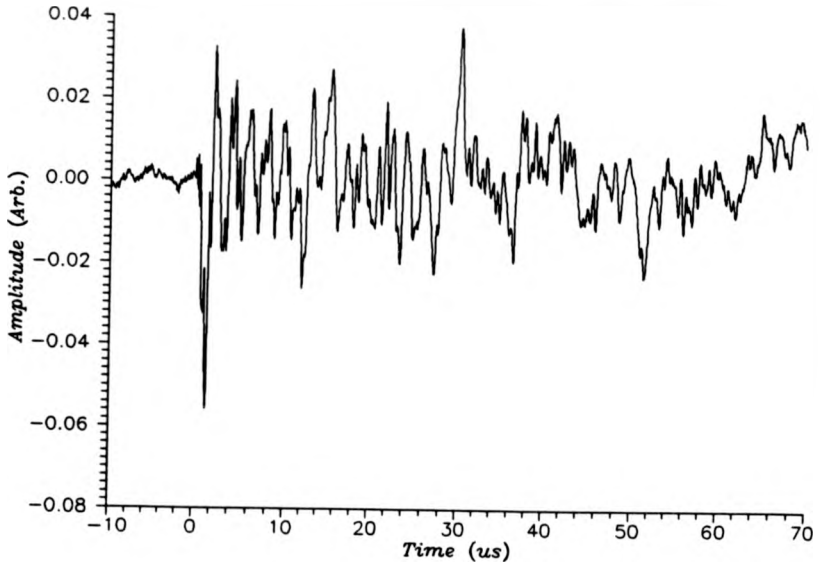

Figure 3.21a The ultrasonic time waveform obtained with an adhesively bonded sample at room temperature.

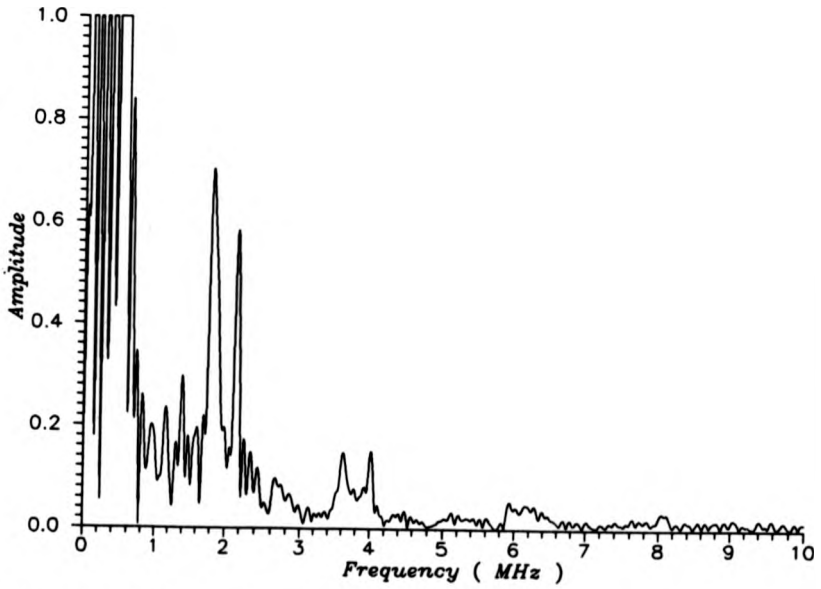

Figure 3.21b The corresponding frequency spectrum.

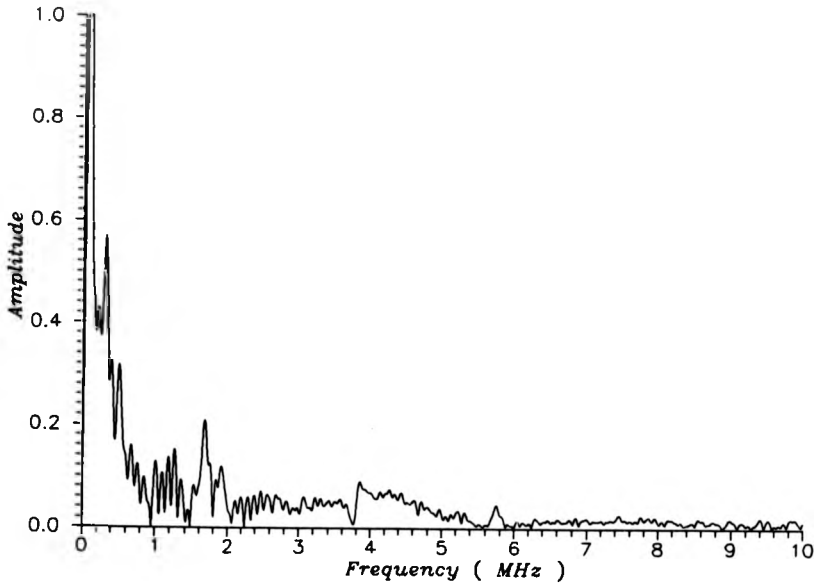

Figure 3.22a The frequency spectrum at 260°C.

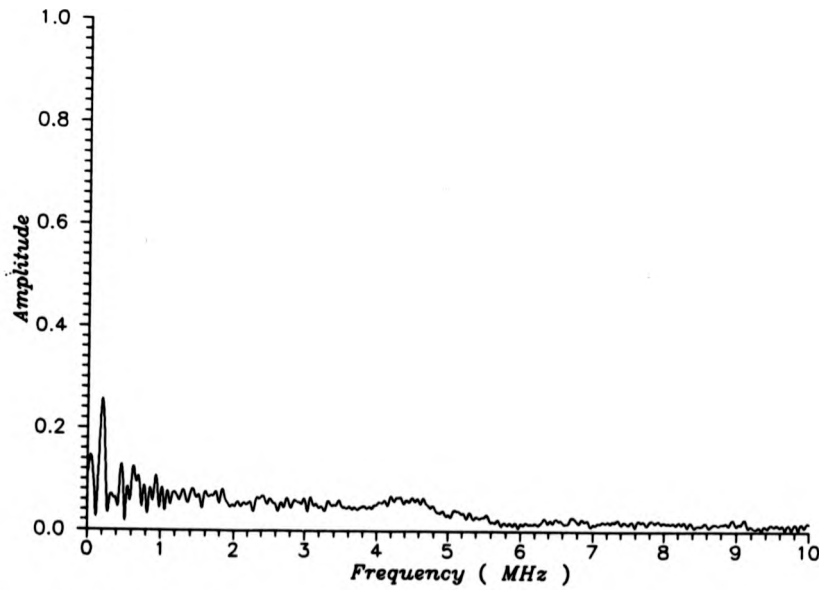

Figure 3.22b The frequency spectrum at 280°C.

in Figure 3.23, where the positions of the resonances are plotted against the sample temperature. Whilst the changes are only very small, the movements of the resonance positions are seen to follow the same trends as were predicted by the theories described in the last chapter, which can be seen by comparing this figure with (what would be a small vertical section of) Figure 3.12.

This experiment shows that the ultrasonic spectroscopy technique can be used with non-contacting ultrasonic techniques to detect the gross failure of adhesive bonds at elevated temperatures.

3.4 Ultrasonic modelling, testing and monitoring of adhesive bonds, and comparison with destructive tensile tests

The theory described in Chapter 2, together with the experimental results described so far in this chapter show that spectroscopic analysis of ultrasonic waveforms obtained using normal incidence ultrasonic waves can be used to detect gross defects within the bonds, and the theory suggests that this technique might be used to monitor the adhesive-adherend interface in "poor bonds", which is notoriously difficult to do. This section describes simple theoretical modelling that was undertaken to assess what difference might be seen in the frequency response of a good bond, compared to a poor bond. Following this, a number of samples containing artificial defects were tested ultrasonically and analyzed, and then destructively tested in order to see if any correlation between the nondestructive and destructive tests existed. Finally, a number of samples were ultrasonically monitored as they were being stressed.

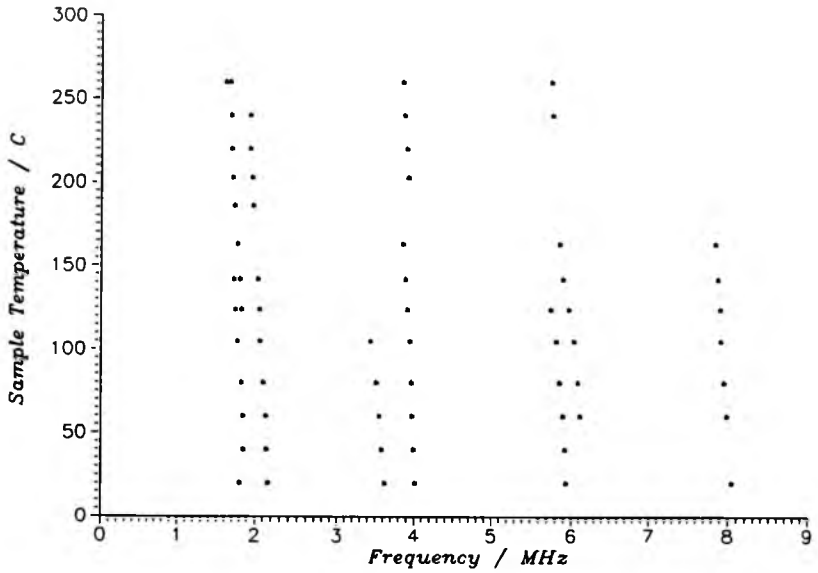

Figure 3.23 Variation of resonance frequencies of an adhesive bond with temperature.

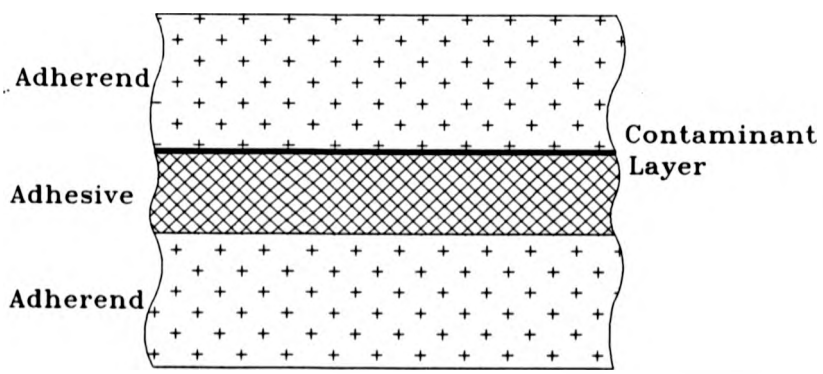

Figure 3.24 Simple schematic diagram of an adhesive bond incorporating a slipping contaminant layer.

3.4.1 Modelling of defects in adhesive bonds

In the last chapter, a computer program was used to model the frequency response of ideal adhesive bonds. In this section, it is described how an extra, extremely thin layer of contaminant was considered between the adhesive layer and the adherend in attempt to model (very simplistically) a "poor" bond. The oil layer was introduced to try to imitate defects that cause these "poor bonds" such as a lack of cohesion, a thin oxide layer on the adherend, or a contaminated adherend surface. The layup that was modelled is shown schematically in Figure 3.24, and assumes that the contaminant layer forms a perfect "slipping layer" between the adherend and adhesive. This is perhaps too great an over-simplification, as the perfect slipping interface is thought not to exist in real structures; what is thought to be a more representative situation is shown schematically in Figure 3.25, and has been referred to as a "kissing bond". This has, on the microscopic level, a proportion of the interface that is perfectly bonded, and a proportion that exhibits slippage.

Despite the approximations that were made when considering a slipping rather than a kissing bond, it was thought that modelling a pure slipping bond could show any general trends of change in the frequency response of the frequency spectra, which would be sufficient to show what aspects of these spectra should be monitored for these tests. The main acoustical property of the contaminating layer that was thought to be important was that of ultrasonic attenuation; the extreme attenuation of shearwaves by "slipping materials" (i.e. liquids) is well known to anybody who has tried to couple a normal-incidence shearwave transducer onto a testpiece. The effect of the impedance of the layer,

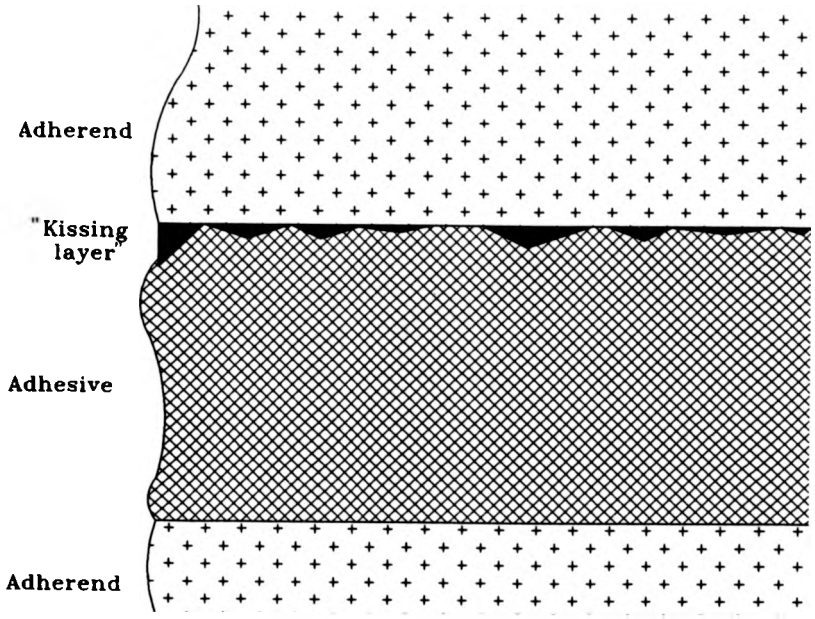

Figure 3.25 Schematic diagram of a more complex bond, incorporating a "kissing layer".

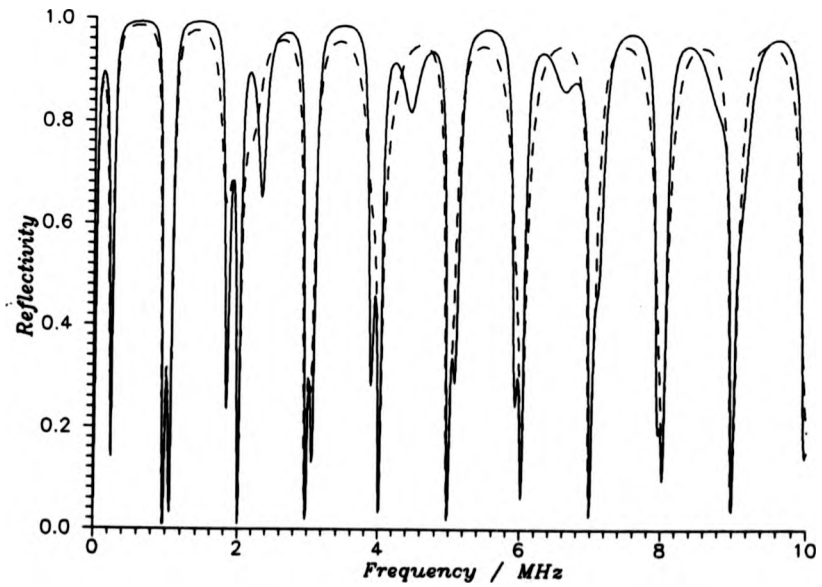

Figure 3.26 The effect of introducing a "slipping", thin oil layer into an adhesive bond.

although a factor which cannot be ignored, is of lesser importance, as the oil layer is very thin, and the impedance mismatch between the epoxy and the oil is not excessive.

The predicted shear wave reflected frequency spectrum for an adhesively bonded lap joint comprising of 1.6mm aluminium adherends and 0.25mm epoxy adhesive (shown as the solid line), together with the spectrum for the same joint incorporating a 5×10^{-6}m thick layer of oil is shown (as the dashed plot) in Figure 3.26. For this, the oil was given a density of 0.9, a longitudinal velocity of $1500ms^{-1}$, a shearwave velocity of $450ms^{-1}$, and attenuation of $-250i ms^{-1}$. The shearwave velocity had to be derived empirically; values for the shearwave velocity of liquids could not be measured (liquids are usually assumed not to support shearwaves), and so a plot of the longitudinal and shearwave velocities of a number of materials was made, and a least squares fit line was made from this data. Knowing the longitudinal velocity in oil, it was then trivial to evaluate its predicted shearwave velocity. The attenuation of the oil could not be accurately measured, and so the value used was a "best guess".

A comparison between the frequency spectra of Figure 3.26 shows that some of the peaks appear to be relatively unaffected by the addition of the oil layer (for example at 2.0MHz), whilst others are greatly attenuated by the oil's inclusion (for example at 2.2MHz). This is as expected; the resonances that had the ultrasonic energy concentrated within the epoxy layer (causing a maximum strain at the adherend-adhesive interface) were the ones that were most affected by the addition of the oil layer.

3.4.2 Experimental testing of defective adhesively bonded lap joints

A number of specimens were prepared by T.W.I. for these tests. They included a range of artificial defects, and were made to be suitable for destructive tests to assess the shear strength of the bond. The four groups of samples had their surfaces treated as follows;

i) degreased

ii) uncleaned, but wire brushed

iii) Oil contaminated

iv) wax marker contaminated

Ultrasonic waveforms were obtained from these samples with a 2.25 MHz, 0.5", hard-faced, normal incidence shearwave transducer, which was carefully coupled to the samples with a thin layer of honey. The waveforms were taken, and their frequency spectra obtained in much the same way as described in section 3.2.3 of this chapter. A typical frequency spectrum (from a degreased sample) is shown in Figure 3.27.

After the samples had been tested ultrasonically, they were destructively tested in a tensile test rig (a Monsanto tensiometer), and their shear failure strengths recorded. It should be noted that all of the samples failed at one of the adherend-adhesive interfaces, and therefore it was the interface strength that was recorded, not the cohesive strength of the adhesive.

The ultrasonic spectra were analyzed by measuring the height of a resonance that was shown by the model to be affected by the oil layer (labelled B in Figure 3.27), and then dividing this by the height of a resonance that was shown not to be affected by the oil layer in the model (labelled A). This division was

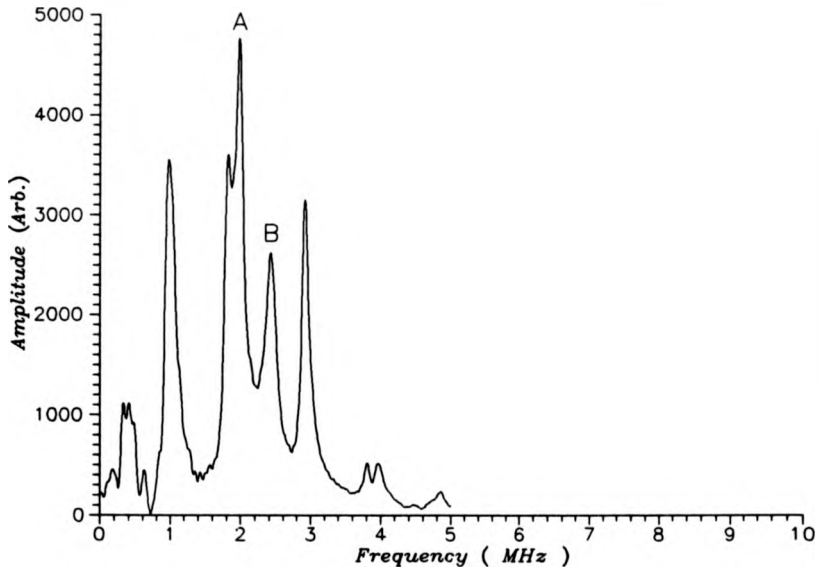

Figure 3.27 The measured frequency response of an adhesively bonded sample that was subsequently destructively tested.

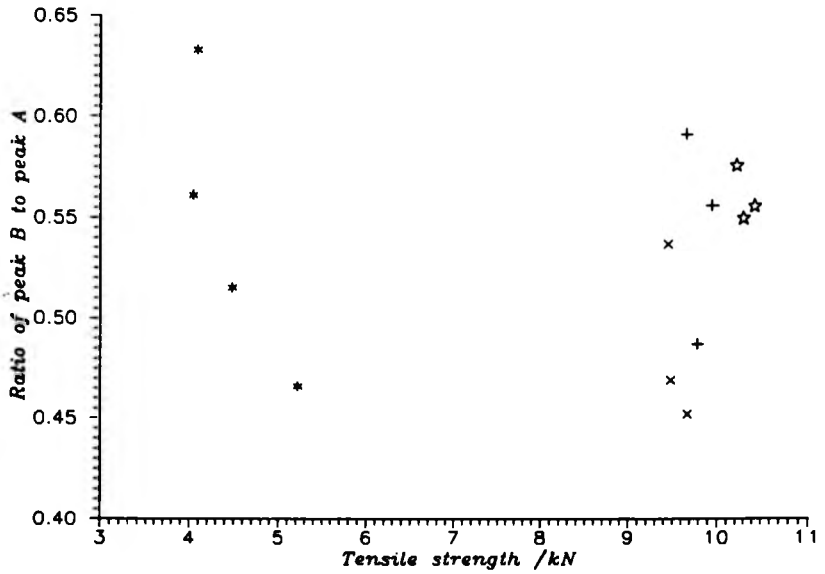

Figure 3.28 The the ratio of peak B to Peak A compared to the shear strengths of the adhesive bonds

done to effectively "normalise" the height of resonance B as the amplitude of the ultrasonic signal could not be assumed to be sufficiently constant between different samples due to many factors, the main one being the variability encountered with coupling the transducer to the samples.

A plot of this ratio against shear strength is given in Figure 3.28 for a number of samples. In this, * represented the oil contaminated specimens, ☆ represented the degreased samples, × represented the wire-brushed samples, and + represented the samples with the wax marker. It is seen that no clear correlation exists, and this might be accounted for by a combination of two factors; firstly that the reduction of the resonances that are predicted to be attenuated by the oil layer might be rather small, as the area of "slippage" in the bonds tested might also be small. Secondly there will exist a variability in the measured height of a resonance between nominally identical samples due to minute adhesive thickness variations, adhesive velocity variations, transducer coupling, and noise in the measured waveform. Future work might look at computing algorithms to compensate for variations in adhesive thickness and velocity, whilst the variability of the coupling between the transducer and sample might be eliminated by obtaining waveforms with shearwave EMATs. The next section looks at the change in the frequency response of a single sample whilst it is being stressed, and therefore overcomes a number of these factors.

3.4.3 Testing of adhesive bonds under stress.

As well as being able to detect gross defects, it was thought that spectroscopic techniques might be capable of monitoring the minute degradation

of an adhesive bond as it was stressed (for example in a tensiometer). This might, in the first instance, give extended information as to the dynamic changes in the bond whilst it was being stressed, and secondly, might lead to a technique that could be applied to the monitoring of adhesive bonds in safety critical areas, (such as aircraft panels), throughout the life of the adhesively bonded structure.

For these experiments, a 2.25MHz, normal incidence shear wave transducer coupled with a thin honey layer was rigidly clamped over the bond on the sample under test (these were similar samples to the ones used in the experiments described above). The sample was then pulled in the tensiometer to a strain of 1kN, and an ultrasonic waveform was taken and recorded. The strain on the sample was then released, and a second waveform taken. This cycle was then repeated a number of times, recording a number of waveforms, until the specimen broke. The resultant waveforms were subsequently transferred to a computer and analyzed. The sample was relaxed after being stressed to distinguish between changes in the frequency spectrum that were caused by permanent changes in the adhesive bond, and temporary changes caused by stress in the adhesive layer.

A typical time waveform and frequency spectrum from a bond are shown in Figures 3.29a and 3.29b respectively. In Figure 3.29b, the solid line was taken with the bond under 1kN of stress, and the dashed line was taken with the bond under 7kN of stress. It is clear that the amplitude of some resonances (for example those labelled B and C) have been significantly reduced by the stress, whereas others (for example the one labelled A) have not. This is as predicted by the modelling described previously. As the bonded structure was stressed, the height of the peak labelled B was divided by the height of the peak labelled A,

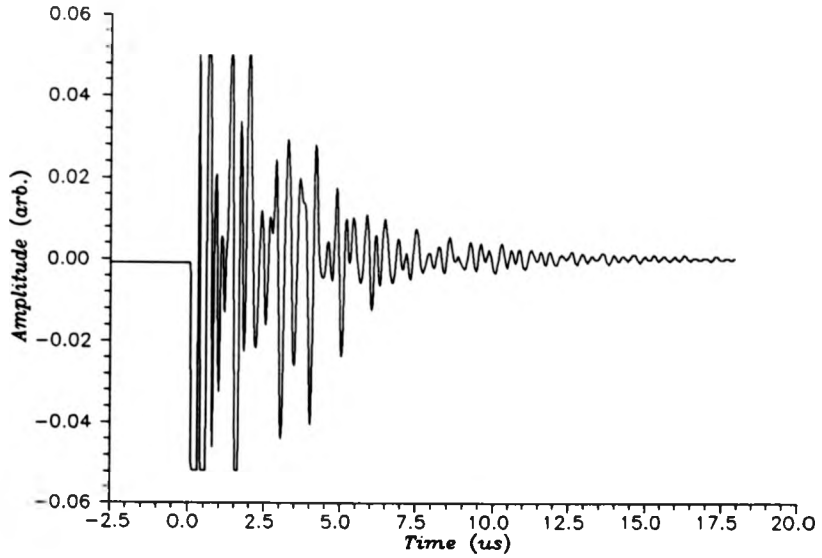

Figure 3.29a The shear waveform taken on an adhesive bond whilst under tension in a tensiometer.

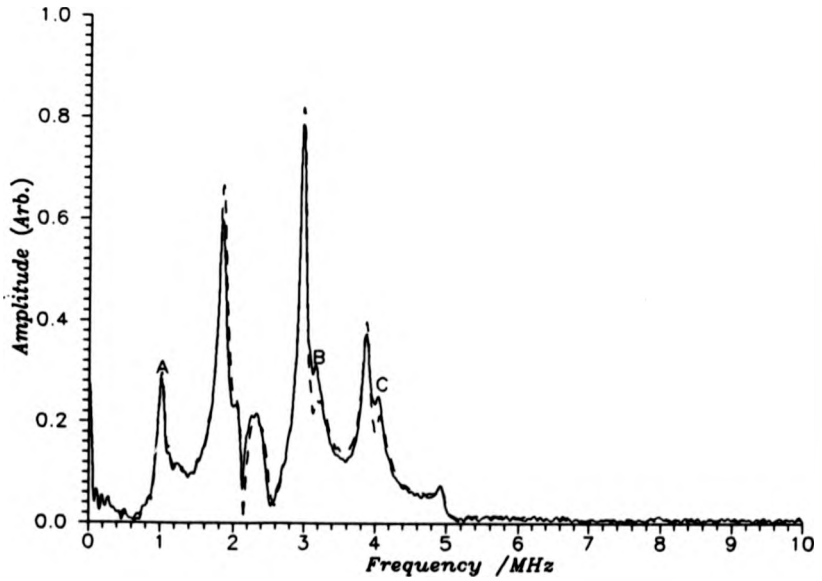

Figure 3.29b The measured frequency response of an adhesive bond before stressing (solid line), and after stressing (dashed line).

and this was plotted against the tensile force that the sample has been subjected to.

An example for a nominally good sample (one with no introduced defects) is given in Figure 3.30. Here, the measurements taken under tension are shown as an ×, and the measurements taken when the bond was unstressed are shown as a +. Figure 3.30 shows that the stressed and un-stressed results are very similar, indicating that any changes are permanent (and are not due to the stress in the adhesive layer). The ratio of the peaks (effectively the normalised height of the peak labelled B) are seen to decrease as the bond is increasingly stressed, with the gradient of this change increasing with increasing stress (which is particularly noticeable in this plot over 5kN,). The sample failed at 7.1kN. Similar results were obtained with a number of samples.

An example of a plot from a sample that had been contaminated with oil is given in Figure 3.31. Again, the amplitude of the peak ratio decreased with increasing stress, but the important thing to notice with this sample was that the final points started to *increase* in amplitude as the sample approached failure, this was not expected, but could prove to be a useful effect for a monitoring technique.

The effects shown for both of the above samples indicate that this approach could be used as a useful nondestructive monitoring technique.

3.4.4 modelling, nondestructive and destructive testing - conclusions

A comparison of the predicted frequency response between good and defective adhesive bonds predicted significant changes in the amplitude of some resonances, and negligible changes in others. This was used to see whether "poor

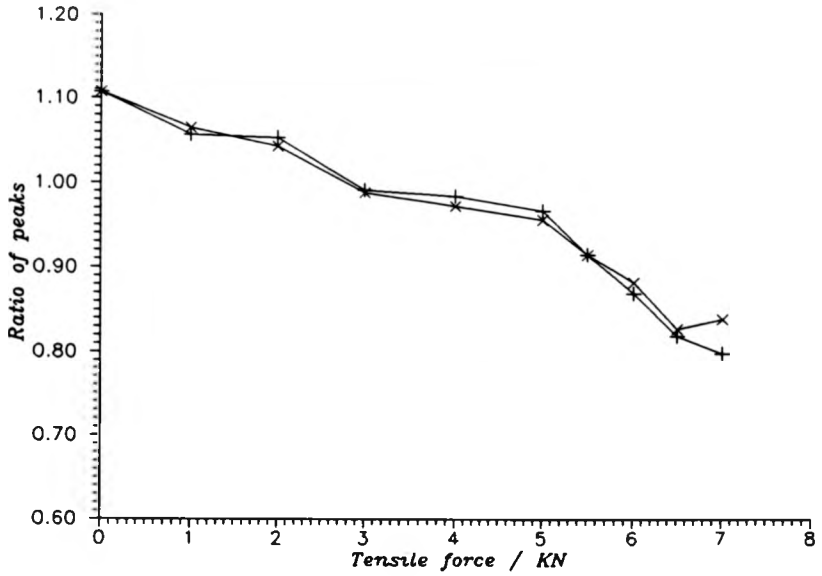

Figure 3.30 The effect of straining the sample on the relative height of a resonant peak, good sample (× represents a measurement taken under stress, and + represents a measurement taken whilst the sample is relaxed).

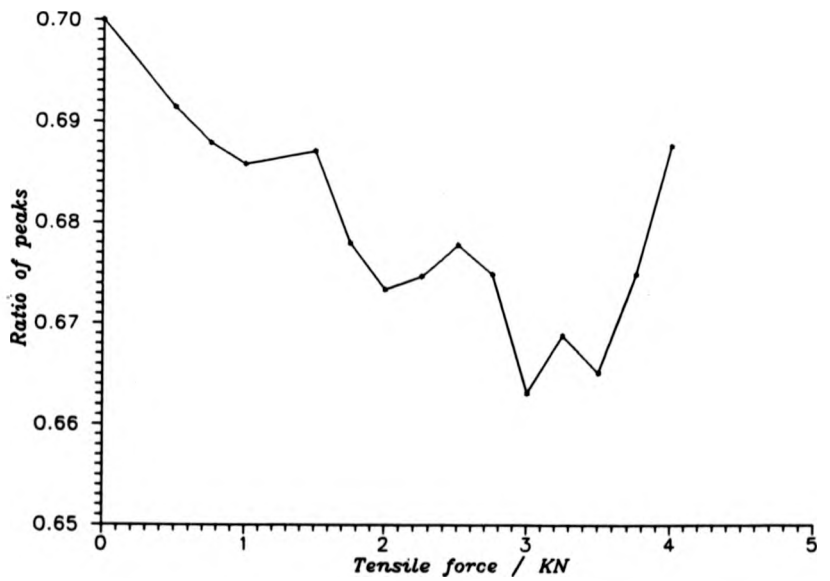

Figure 3.31 The effect of straining the sample on the relative height of a resonant peak, sample contaminated with oil.

bonds" could be detected in a variety of samples, but was found not to work. When the frequency response analysis was applied to samples as they were being stressed, the predicted changes in the frequency spectrum were observed. It is thought that this technique might therefore be developed to monitor safety critical bonds throughout their lifetime, and might be used to indicate whether the bond has been overstressed, or is approaching premature failure.

3.5 Conclusion

This chapter has followed on from Chapter 3 by experimentally investigating the frequency response of adhesive bonds. It has been shown that there is excellent agreement between the predicted, and the experimentally derived frequency spectra, for both longitudinal and shear waves (although the experimental method used for obtaining shear waveforms caused the inversion of the spectra). It has been shown that the frequency response of the bonds can clearly show the presence of gross disbonds, and this approach can therefore be used as a nondestructive testing technique that can be readily applied to detecting such defects.

It has been shown that the experimental spectra can be obtained with a variety of transduction techniques (both contacting and non-contacting), and that these techniques have been demonstrated at elevated temperatures.

This chapter concludes by looking at the problem of testing for "poor bonds", for which a method of nondestructive testing has been notoriously elusive to find. Modelling the frequency response of poor bonds predicted changes in the amplitudes of certain resonances, leaving others unaffected. Applying this to a

number of specimens, (some incorporating artificial defects), no correlation was observed between the predicted quality of the bonds, and the destructively measured strength of the bonds, this was attributed to variabilities between the different bonds masking over any effects that could have been observed. This was not the case, however when this technique was applied to monitoring the changes in a bond as it was stressed, which clearly showed the predicted changes in the frequency spectra.

Future work might include the use of improved mathematical techniques, together with EMAT transducers to try to reduce thickness and coupling effects, and thus to try to develop a technique that is sensitive to "poor bonds". These techniques might also be applied to samples in fatigue rigs to monitor their degradation.

3.6 References

1. D.R.Billson and D.A.Hutchins, "Laser - EMAT ultrasonic measurements of bonded metals", Nondestr. Test. Eval., Vol.10, (1992). pp. 43-53
2. D.R.Billson and D.A.Hutchins, "Resonance studies of bonded aluminium joints", Nondestr. Test. Eval., Vol.10, (1992). pp. 149-165.
3. R.P.Cocker and R.E.Challis, "Automatic algorithms for digital signal processing to characterise the propagation of ultrasound in thin adhesive layers", Ultrasonics International 1993 conference proceedings, pp. 299-302.
4. J.Laperre, "Dispersion of elastic waves in a bi-layer", Ph.d. Thesis, Katholieke Universiteit Leuven, 1991.
5. L.F.Bresse, M.Sc. thesis, Queens University, Kingston, Ontario, Canada.

CHAPTER 4

NONDESTRUCTIVE EVALUATION OF HYDRIDE CONCENTRATION IN ZIRCONIUM-NIOBIUM ALLOYS

4.1 Introduction

Canadian Deuterium-Uranium (CANDU) reactors each contain several hundred zirconium-niobium pressure tubes. The 97.5% zirconium, 2.5% niobium alloy, sometimes called zircalloy, is prone to hydrogen and deuterium absorption, which can lead to the formation of zirconium hydride platelets[1,2]. These make the zircalloy brittle, severely reducing its strength[3], and this has caused a number of failures leading to pressure tube leaks. Indeed, it was the cause of a major failure in one early reactor[4]. This problem has necessitated the premature retubing of the earliest Canadian reactors at a cost of several hundred million dollars each. A nondestructive method of measuring the hydride concentration in such metals is thus of great interest, in that it would allow selective, rather than complete, retubing of the reactors, thus presenting a large cost saving.

A diagram for the zirconium-hydrogen system is shown schematically in Figure 4.1 for low hydrogen concentrations in parts per million (ppm), and shows the two phase system ($\alpha+\delta$, metal + hydride)[5] becoming a single phase system (α, metal only) when heated. Thus, at the phase transition, the zirconium hydride dissociates into the metal and free hydrogen, which then has a tendency to migrate through the metal. On cooling, the reverse process occurs, i.e. the hydride precipitates, usually into the form of small platelets. These platelets have a characteristic acicular or plate morphology, which is often referred to as a "cornflake" structure[6]. In some cases, migration effects due to thermal gradients or stress cause local concentrations of hydride in the form of brittle blisters[7], which are the main cause of in-service failures. It is evident from Figure 4.1 that the temperature at which the zirconium hydride dissociates on heating, and

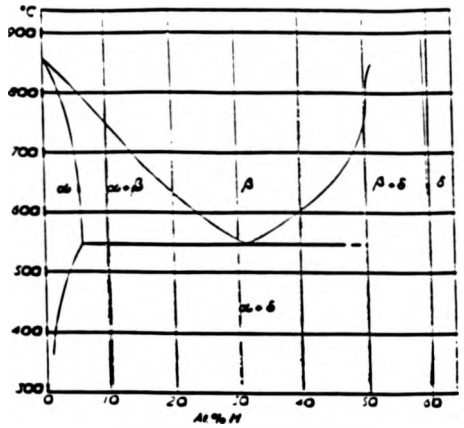

Figure 4.1 Phase diagram for the Zr-H system, after Smithells[5].

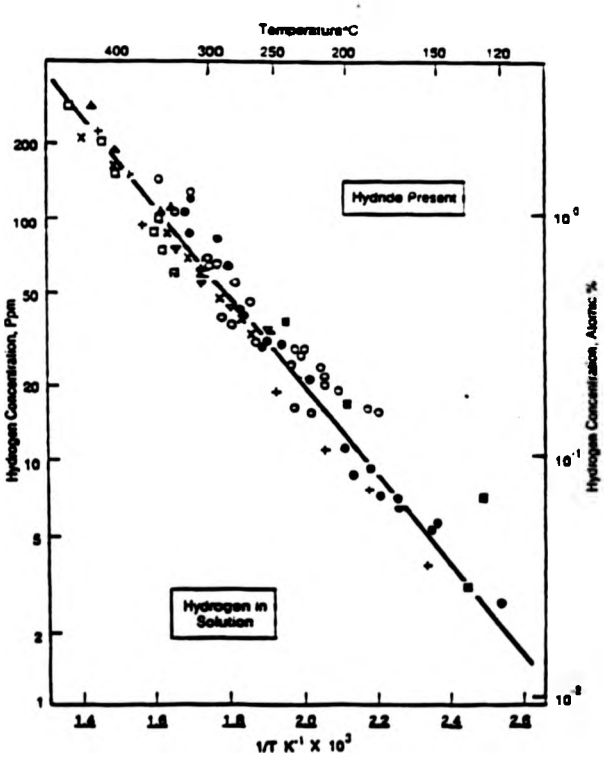

Figure 4.2 Graph of SST's Vs hydride concentration

reforms on cooling, depends on the initial concentration in ppm of the hydride in the zircalloy. Thus, if this temperature (the solid solubility temperature, SST) is known, the initial room temperature hydride concentration can be estimated[8]. A number of workers have measured the SST's for samples with known hydride concentrations, and their cumulative results are shown in Figure 4.2[9].

It was thought that there might be a change in the material characteristics of the zircalloy at this transition temperature, which would lead to a change in ultrasonic velocity. Hence, methods for measuring the transit time of both shear and longitudinal waves through samples of the alloy, as a function of temperature, have been devised. These work at temperatures of up to 550°C, and use a pulsed laser as an ultrasonic source, and specially developed high temperature electromagnetic acoustic transducers (EMATs) as receivers[10].

High temperature EMATs are well documented in the literature[11,12,13,14], but most either require water cooling for continuous use, or can only be used for short periods of a few seconds at a time. The EMAT receiver described in this paper is unusual in that it was designed to run at these high temperatures continuously, and without any cooling.

One complication in transit time studies is the effect of dimensional changes, and hence thermal expansion studies were also carried out using dilatometry. Previous studies have shown that a change in thermal expansion coefficient might be expected at the SST, but the effect reported was very small[15,16]. This seems to have been due, in part to the apparatus used, and in the methods of presentation of the acquired data.

The present work has investigated the above methods with the aim of

measuring the SST experimentally. This in turn would lead to an estimation of hydride concentration within a particular zircalloy sample. The following thus outlines the ultrasonic experiments developed to perform this measurement in small samples, with concurrent dilatometry experiments. It will be shown that either measurement could, in principle, lead to an estimation of hydride content. A discussion of how this might be implemented in practice is also given.

4.2 Apparatus and experiment

4.2.1 Ultrasonic studies

Samples of zirconium-niobium alloy were available with known concentrations of hydrogen present. At room temperature the hydrides are present in the form of platelets which have precipitated between metal crystal boundaries, and are readily visible when a prepared, polished sample of hydrided zircalloy is viewed under a microscope[17]. This is shown in Figure 4.3 for samples with (a) nominally no hydride, (b) 30ppm, (c) 60ppm, and (d) 100ppm hydride. In these photographs, the hydride platelets are visible as dark horizontal lines, and have precipitated preferentially in an axial/circumferential plane due to the metallic microstructure induced by prior rolling of the material.

The experiments using ultrasonic techniques were designed to investigate such samples in the form of flat plates of approximately 4mm thickness, these were obtained by rolling tubing material flat. Samples were available with dimensions 30mm x 25mm. These samples were to be heated to temperatures of up to 400°C, and ultrasonic data taken as the sample cooled slowly through the SST.

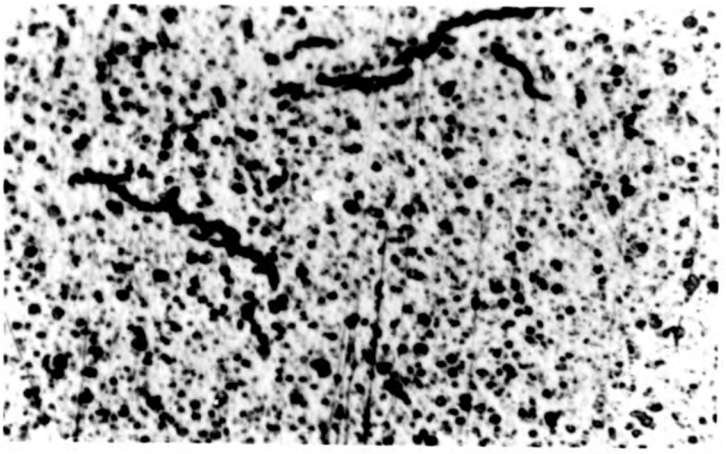

Figure 4.3c Micrograph of a polished sample of zircalloy with 60ppm of hydride concentration (×80)

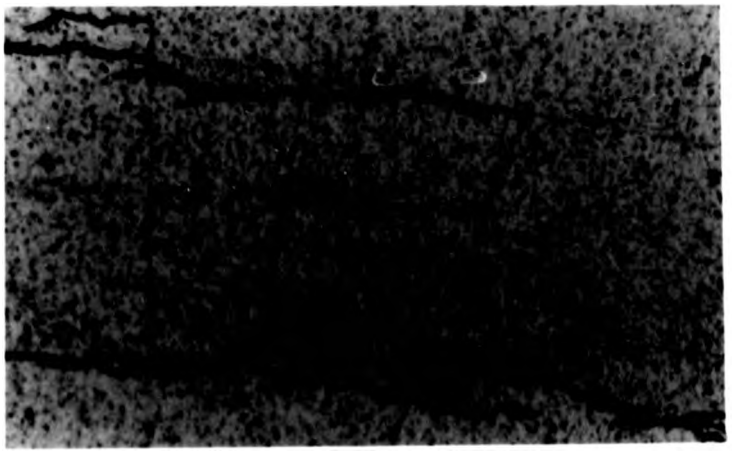

Figure 4.3d Micrograph of a polished sample of zircalloy with 100ppm of hydride concentration (×80)

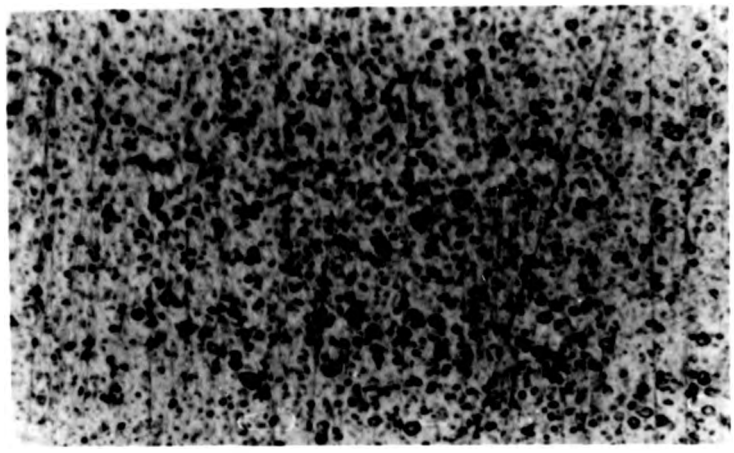

Figure 4.3a Micrograph of a polished sample of zircalloy with no hydride present (×80)

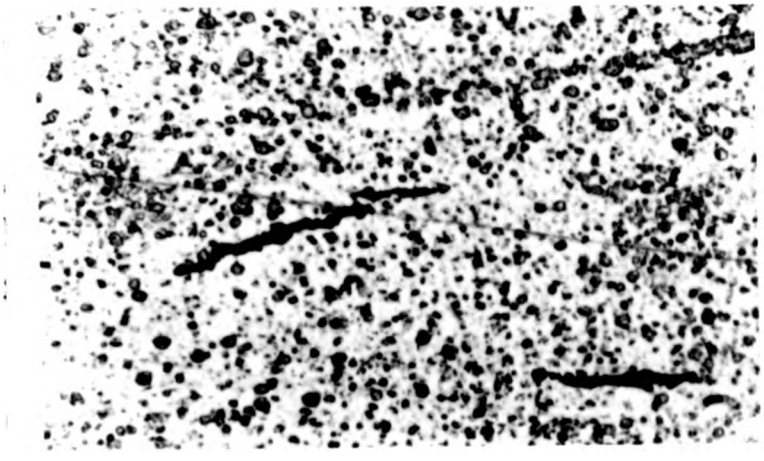

Figure 4.3b Micrograph of a polished sample of zircalloy with 30ppm of hydride concentration (×80)

The approach adopted was to use a pulsed laser as an ultrasonic source, and an electromagnetic acoustic transducer (EMAT) as a receiver. The apparatus used for this is shown schematically in Figure 4.4. The laser was a Lumonics 'mini-Q' neodymium-YAG, Q-switched laser, delivering 4ns pulses of 1060nm infra-red radiation, at energies up to 120mJ. The laser beam was focused with a 170mm focal length lens through an aperture in the brass housing onto the sample, with the sample face 300mm from the lens. The EMAT output, was preamplified by a specially developed low-noise, high-bandwidth amplifier, this was based around a ZN-459CP operational-amplifier chip, and the circuit diagram for this is given in Figure 4.5. After preamplification, the signal was digitised on a Data Precision Data 6000 oscilloscope, and after averaging, the waveform was transferred onto an IBM 30-286 computer and stored. The temperature of the sample was measured with a thermocouple attached directly to the sample face.

The EMATs had to be designed with some care. Firstly, the EMAT was optimised for either longitudinal or shear detection, and had to operate at small distances of 0.5mm or less from the zircalloy samples in order to maintain an acceptable signal. In addition, either type of detector had to have a sufficiently wide bandwidth to allow multiple reflections within the 4mm thickness of the samples to be measured accurately. Finally, the EMATs had to be designed so that they would not act as a heat sink, as this might cause thermal gradients within the samples (a transition at a specific temperature was being sought, and hence having a variation of temperature throughout the sample thickness would smooth out any results). Initial experiments showed that water-cooling the EMATs caused unacceptably large thermal gradients within the sample, and

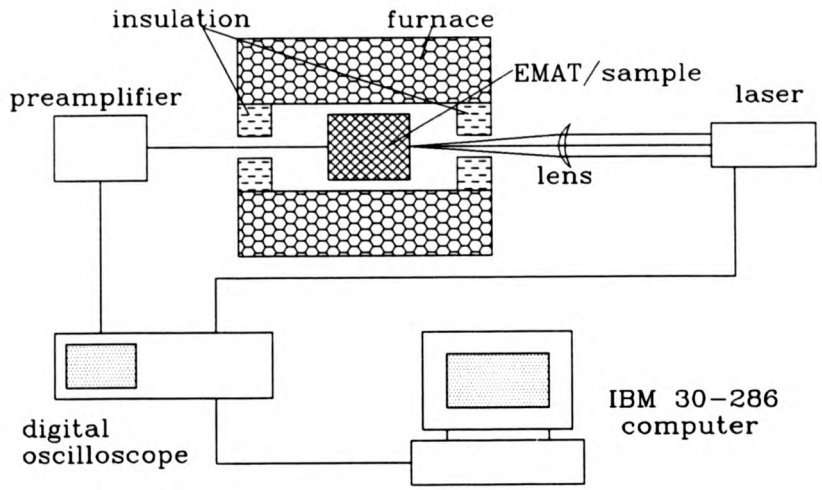

Figure 4.4 Experimental apparatus to investigate ultrasonic velocity measurements at high temperatures

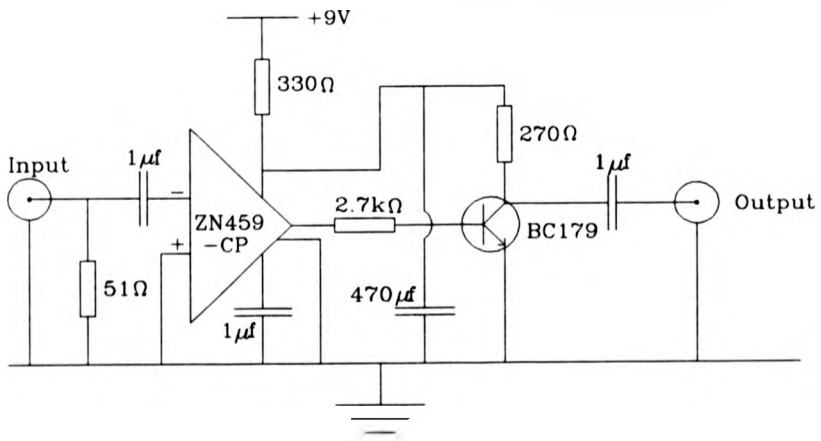

Figure 4.5 Circuit diagram for the preamplifier used in conjunction with the EMATs

hence EMATs were developed that could be maintained at the same temperature as the samples. These EMATs used alcomaxIII magnets, rated for continuous use at temperatures of up to 550°C. Although they produce a much smaller magnetic field than the more commonly used neodymium-iron-boron magnets, they were adequate for this purpose. The EMAT and the sample were enclosed together within a brass housing to ensure that their temperatures were equal, thus reducing any thermal gradients within the sample.

The EMAT coils presented considerable problems, as no sufficiently thin wire (0.1mm or less) was readily available that had insulation capable of withstanding temperatures over 150°C. This was solved by coating the wires with a high temperature ceramic paint, Duralco 252, as the wires were wound. The longitudinal EMAT (Figure 4.6(a)) used a coil wound linearly around a brass former and used steel pole-pieces that were designed to give a strong magnetic field parallel to the sample surface and perpendicular to the coil, thus optimising the conditions to detect motion normal to the surface[18] and hence longitudinal waves. The shear wave EMAT (Figure 4.6(b)) used a pancake coil which was sensitive to radial shear waves. This enabled shear waves with any particular polarization to be detected equally well, which was an important consideration as the zircalloy was elastically anisotropic, and hence acoustically birefringent for shear waves. The magnet for this detector was oriented to give a magnetic field normal to the sample surface, thus maximising the sensitivity of the device to motion parallel to the sample surface. Note that a more detailed description of the principles of operation of both longitudinal and shearwave EMATs was given in Chapter 1 of this thesis, together with a description of the mechanisms of

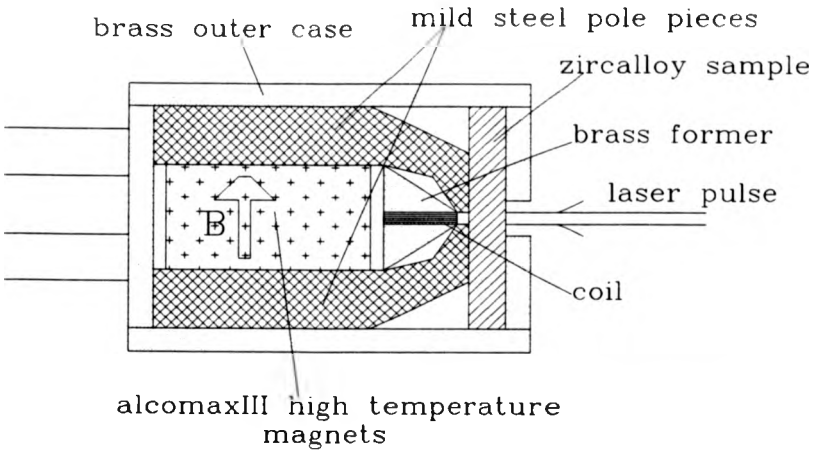

Figure 4.6a Schematic diagram of the high temperature EMAT transducer optimised for longitudinal waves

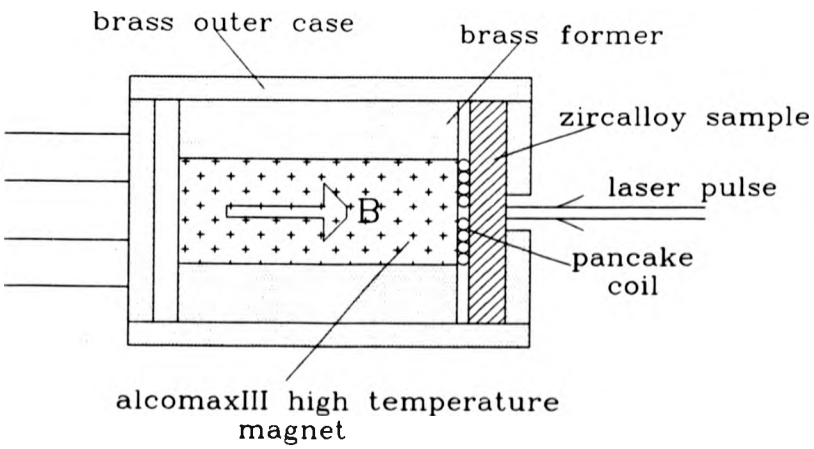

Figure 4.6b Schematic diagram of a high temperature EMAT transducer optimised for shearwave operation

ultrasonic generation by lasers.

In a typical experiment, the furnace was heated up to 400°C, and left for an hour to stabilise. The furnace was then switched off and allowed to cool slowly. The cooling rates of the sample were found to be in the range of 1.2 to 1.7°C per minute around the transition temperatures. Whilst the furnace was cooling, measurements were taken by recording ultrasonic waveforms at specific temperature intervals (usually of about 3°C). Cooling was preferred for the experiment as this gave a slow, even rate of temperature change, which could not be achieved on heating. The waveforms were analyzed on a computer, and the arrival times of some specific peaks were plotted against temperature. The experiments were performed using both longitudinal and shear wave EMATs separately, and repeated for all four samples of zircalloy.

A typical shear waveform recorded by the apparatus described above is shown in Figure 4.7. This waveform is highly complicated due to multiple reflections and mode conversions. Acoustic birefringence is also present, where the shear wave splits into two components, each having a different velocity. However, following careful studies at room temperature using a 20MHz contacting piezoelectric shear wave transducer, it was possible to identify the features in this waveform that corresponded to multiple echoes of the two shear components within the sample, namely the orthogonally polarised fast and slow shear modes.

It was found that multiple reflections of the slow shear wave component exhibited a much greater change in arrival time with temperature than those of the fast shear wave component. Thus, while either mode could have been used,

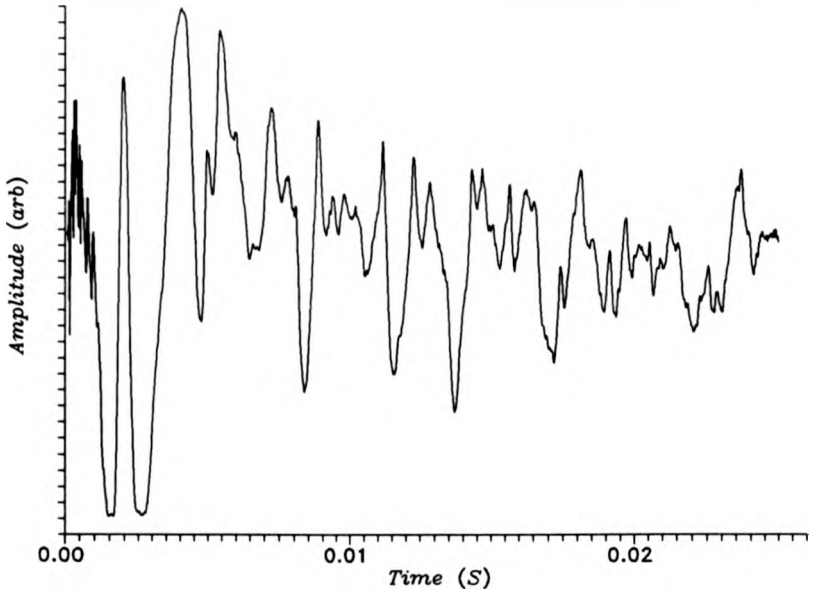

Figure 4.7 A typical shear waveform, recorded for a 60ppm hydrided sample at 298°C

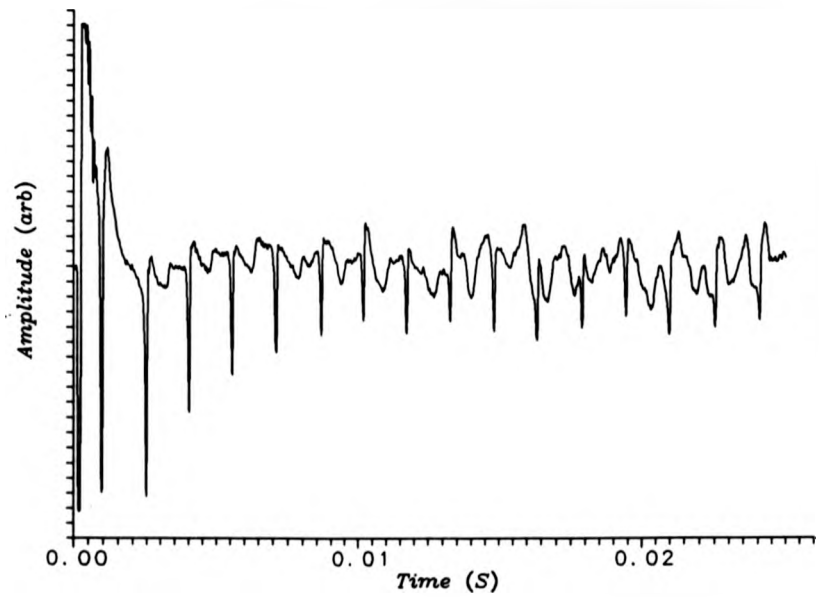

Figure 4.8 A typical longitudinal waveform, taken for a 60ppm hydrided sample at 294°C

most measurements monitored the arrival time of a selected slow shear signal as a function of temperature to minimise experimental errors. For every experiment, a slow shear wave signal was selected to optimise the measurements. This had to be at as great a time delay as possible, as this resulted in a greater sensitivity - additional multiple reflections lead to an increased propagation path length, and hence a greater time shift with a change in velocity. Conversely, accurate measurements of arrival time had to be made as a function of temperature, and this would be enhanced with a greater detection bandwidth. It was found that successive multiple reflections decreased in both amplitude and bandwidth, and hence a compromise was necessary. Typically, the 5th slow wave shear echo was used (labelled 9Ss, having experienced 9 crossings of the plate thickness without mode conversion).

Longitudinal wave experiments were performed with the EMAT of Figure 4.6(a) replacing the shear wave EMAT in the sample holder within the furnace. A typical waveform obtained with this EMAT is shown in Figure 4.8. Whilst the waveform is still rather complicated, it is easy to see the sharp, evenly spaced, monopolar longitudinal waves, which are ideal for the present type of analysis. The last of the transients shown in Figure 4.8 was used, again maximising the change in arrival time with temperature, while still maintaining an acceptable bandwidth.

4.2.2 Dilatometry experiments

Thermal expansion effects will also affect time of flight measurements, and hence needed to be investigated to ensure that any effects measured by time of

flight were due to a change in velocity. In addition, however, measurement of dimensional changes of the sample might lead to information which might supplement that from the ultrasonic data.

The apparatus used for thermal expansion measurements of the same samples is shown schematically in Figure 4.9. The dilatometer was a Netzsh electronic model 402E, incorporating a furnace to heat up the sample, and a Linear Variable Differential Transformer (LVDT) to measure the changes in length of the sample[19]. The LVDT is essentially a transformer comprising of two secondary coils set symmetrically around the primary coil, and a moveable core. The primary coil is excited with an a.c. current, and the induced voltages are measured on the secondary coils. Moving the core changes the inductance of the transformer, thus changing the voltages measured on the secondary coils, These voltage changes can then be calibrated against the core movement. The temperature of the sample was measured with a thermocouple held a short distance away from it.

It should be noted that the dilatometer actually measures the difference between the thermally-induced change in length of the sample, and the length change of the equivalent length of the alumina tube surrounding it. Normally, the correction for the thermal expansion of the alumina is neglected, as it is very small. However, when investigating zircalloy, this becomes very significant, as its thermal expansion coefficient is also very low (and is of about the same order as that for alumina). Fortunately, the (known) thermal expansion coefficient of alumina is linear within the temperature range investigated, and hence could be taken into account when conclusions were drawn from the data.

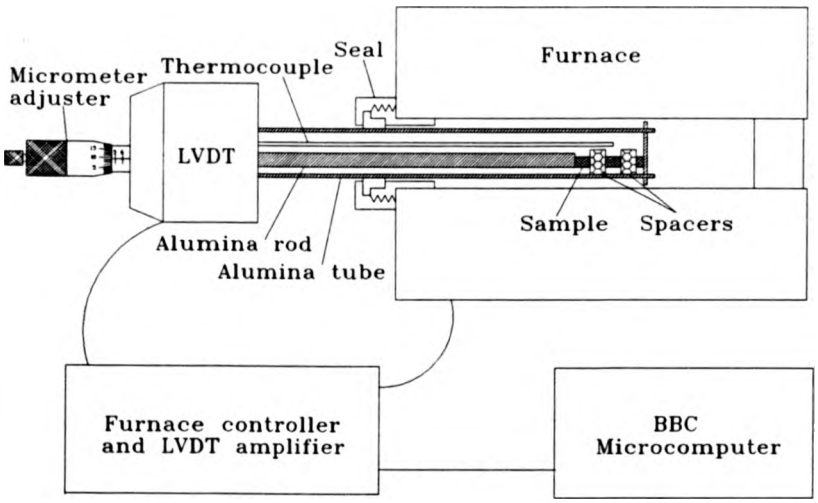

Figure 4.9 Experimental apparatus to investigate the thermal expansion of the zircalloy samples via dilatometry

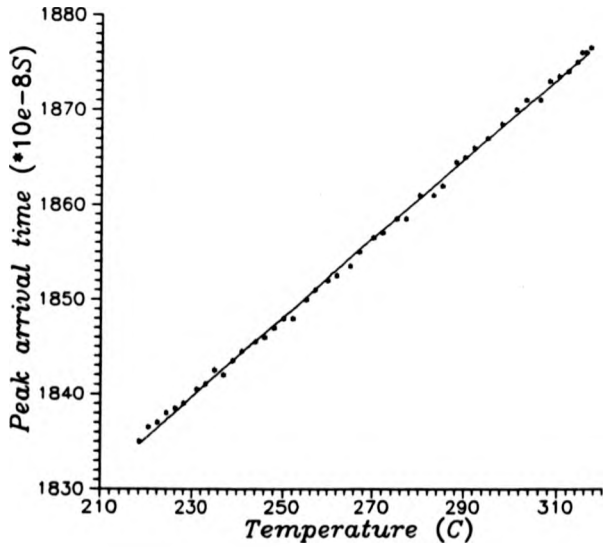

Figure 4.10a Peak arrival time as a function of temperature, using a shear wave EMAT to investigate the unhydrided sample

For dilatometry experiments, small samples were taken from the same starting material used for the ultrasonic experiments, and were cut to dimensions of 4mm by 4mm by 40mm long. Samples were cut both parallel with, and perpendicular to, the axial direction of the tubes from which the material was obtained (the axial and circumferential directions of the tube respectively). Note that samples could not be taken in the through-thickness direction, as they would not be long enough to obtain results with a sufficient accuracy, as they would be only 4mm long. Thus, a total of 4 sample pairs were prepared, with respective concentrations of nominally unhydrided, 30ppm, 60ppm and 100ppm hydride in both axial and circumferential directions.

To measure the SST on cooling, the samples were mounted in the dilatometer, and the furnace was firstly heated up to a temperature above the expected SST, at a rate of 10°C per minute. The furnace was then left to stabilise for 45 minutes, and subsequently cooled to room temperature at a typical rate of 1.5°C per minute. A microcomputer recorded both the sample temperature (using the thermocouple) and the expansion of the zircalloy (using the LVDT) at regular time intervals throughout the experiment. The effect that the cooling rates had on the results was investigated by repeating the above experiments, (using the 60ppm, axially cut sample) with varying cooling rates, and then comparing the observed transition temperatures. This was done with cooling rates of 10°C/min., 6°C/min., 3°C/min. and 1.5°C/min. A separate measurement of the SST could also be made on heating.

4.3 Results and discussion

4.3.1 Ultrasonic measurements

A series of experiments were performed at the various hydride concentrations, using the apparatus of Figure 4.4 and the appropriate EMAT to optimise sensitivity to either shear or longitudinal waves. Consider first the shear wave measurements, which resulted in ultrasonic waveforms such as that shown earlier in Figure 4.7.

The dependence of shear wave travel time on temperature is plotted in Figure 4.10(a) for an unhydrided sample, and shows that there is an approximately linear dependence of arrival time on temperature over the temperature range plotted. This is illustrated further using a linear best fit plot, superimposed on the data. As a comparison, Figure 4.10(b) shows a similar plot for the sample containing 60ppm of hydride, where it is clear that there is a change in gradient at 250°C which is not present on the unhydrided sample. Two best fit lines were plotted in this case, the intersection of which is taken to be the estimated SST, i.e. the temperature at which the hydride platelets precipitate on cooling. The measurements were repeated for the other two sample concentrations, and a graph plotted of the estimated SST as a function of hydride concentration, as shown in Figure 4.11. Here, the "×" symbols represent the shear wave results, with the "+" symbols representing the data described below.

The longitudinal EMAT, shown earlier in Figure 4.6(a), was used to repeat the experiments described above, using the type of waveform shown earlier in Figure 4.8. The data was then analyzed in the same way as for the shear wave data. The results for an unhydrided sample are shown in Figure 4.12(a). As for

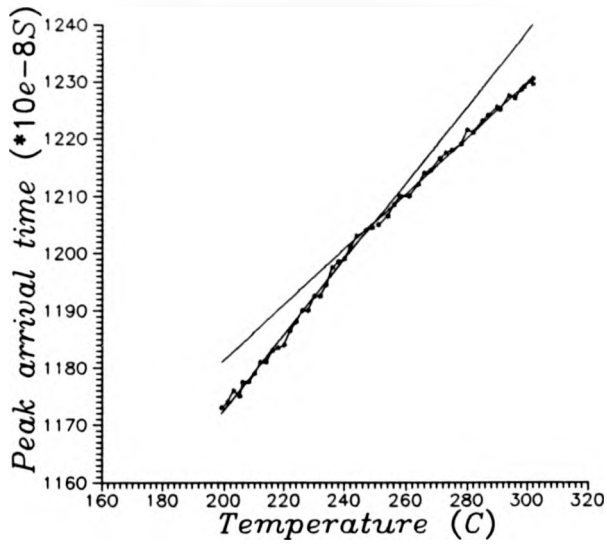

Figure 4.10b Peak arrival time as a function of temperature, using a shear wave EMAT to investigate the sample hydrided to 60ppm

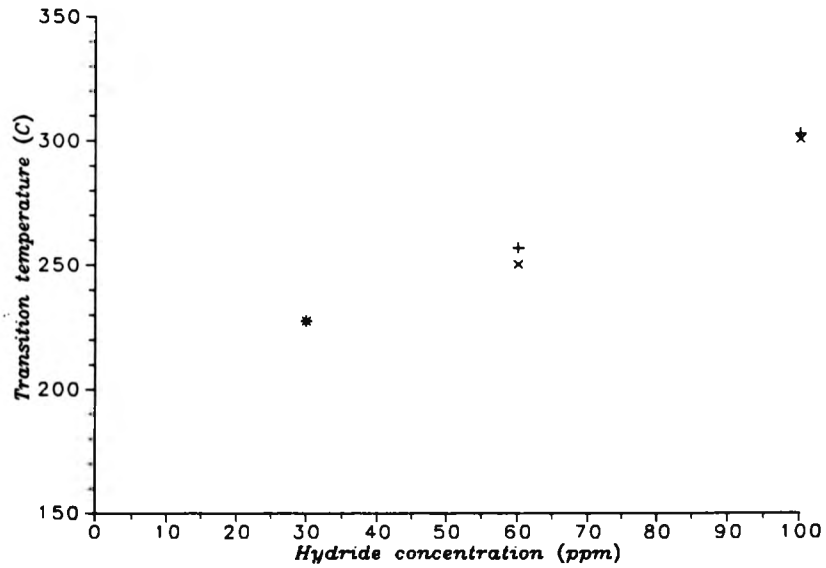

Figure 4.11 Solid solubility temperatures as a function of hydride concentration, obtained from ultrasonic data from a shear wave (×) and longitudinal experiments(+)

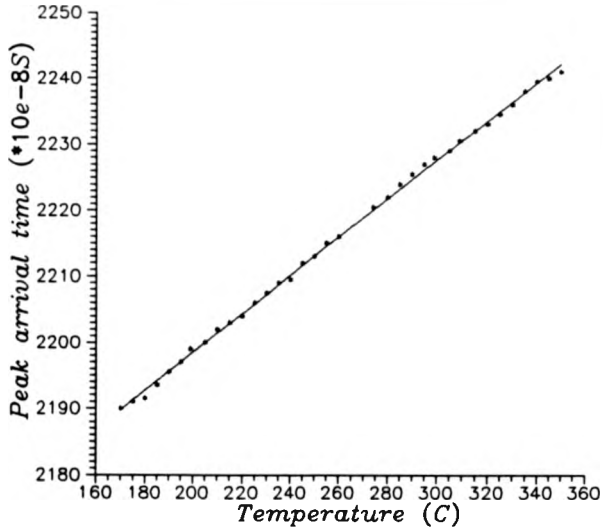

Figure 4.12a Peak arrival time as a function of temperature, using a longitudinal wave transducer to investigate the unhydrided sample

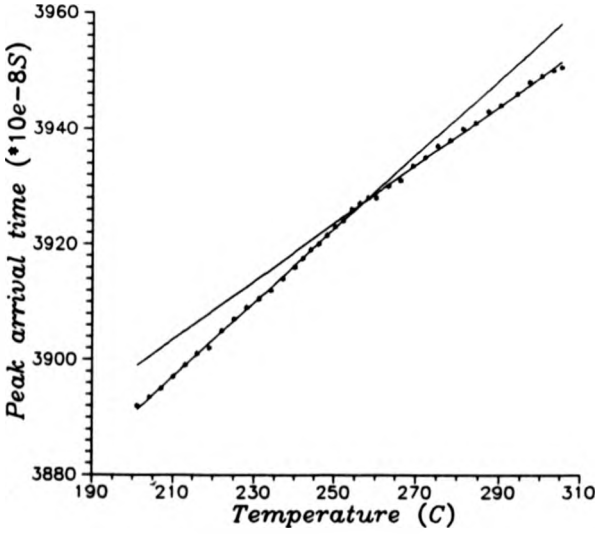

Figure 4.12b Peak arrival time as a function of temperature, using a longitudinal wave transducer to investigate the sample hydrided to 60ppm

the case using shear waves, the graph shows a linear dependence of arrival time with temperature, with no evidence of any discontinuity or phase transition. This was again compared to the result obtained with the sample hydrided to 60ppm, the result being shown in Figure 4.12(b). This shows a definite change in linear gradient at 257°C, again indicative of the SST of the sample following hydride precipitation. This analysis was repeated for all four samples, and the measured SST plotted against hydride concentration together with the shear wave data in Figure 4.11, with the longitudinal wave results represented by a "+".

It is clear from Figure 4.11 that the longitudinal and shear ultrasonic data are in reasonable agreement, and that at the cooling rates used, the SST is a function of nominal hydride concentration. This dependence is also in good agreement with the general trend known from metallurgical studies on this system, as summarised in Figures 4.1 and 4.2. It is thus concluded that the ultrasonic measurements are giving a good indication of the temperature at which the hydride precipitates on cooling, and that this could possibly form the basis for a nondestructive method for determining hydride levels in zirconium alloy tubing material.

4.3.2 Dilatometry

Dilatometry was carried out on the samples used in the above ultrasonic experiments, using the apparatus shown earlier in Figure 4.9. The expansion plot for the axially cut unhydrided sample, with a heating rate of 5°C/min., and a cooling rate of 10°C/min. is shown in Figure 4.13(a). The graph shows a large degree of hysteresis, which is thought to be due to a real effect in the metal, and

has been reported by other workers in the field[16]. There appears to be a slight change in the gradient at about 240°C on the lower section of the graph, where temperature is increasing, but otherwise no significant changes are seen, and there is no evidence of a phase transition in either the heating or cooling phases.

The equivalent thermal expansion data for the samples with 30ppm and 60ppm hydride concentration are shown in Figures 4.13(b) and 4.13(c) respectively. Again, the graphs show a large amount of hysteresis, but the important features to note are that on heating there are large discontinuities in the gradient at 270°C (in 4.13(b)) and at 315°C (in 4.13(c)), and on cooling at 190°C (in 4.13(b)) and at 225°C (in 4.13(c)), these points are marked with an "X" in the figures. These discontinuities are thought to be caused by the solid solubility transition, and this is discussed more fully below.

The expansion plots for the samples cut perpendicular to the principal anisotropic direction gave results that were similar to the plots shown above in Figure 4.13. There were differences in the absolute values of thermal expansion, and in the hysteresis effects, but these can be explained by the anisotropic metallurgy of the sample, caused by the rolling of the tube during manufacture. However, changes in the thermal expansion gradient occurred at temperatures very close to those observed with the samples cut in the axial direction; hence the measurement again seemed to be sensitive to the phase transition caused by the presence of hydrogen.

The above measurements were repeated for all four hydride concentrations, and the temperature at which discontinuities in slope on heating and cooling occurred was measured. The results are plotted in Figure 4.14. Here

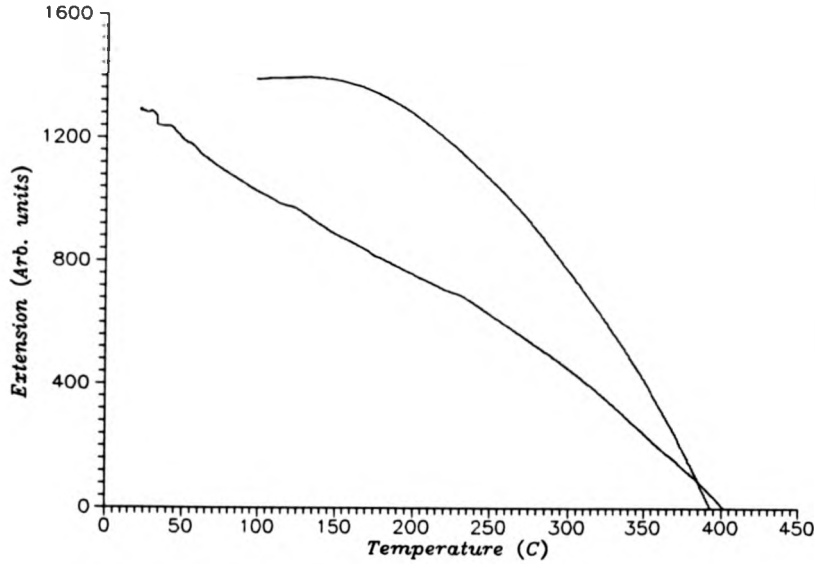

Figure 4.13a Thermal expansion data for the unhydrided sample

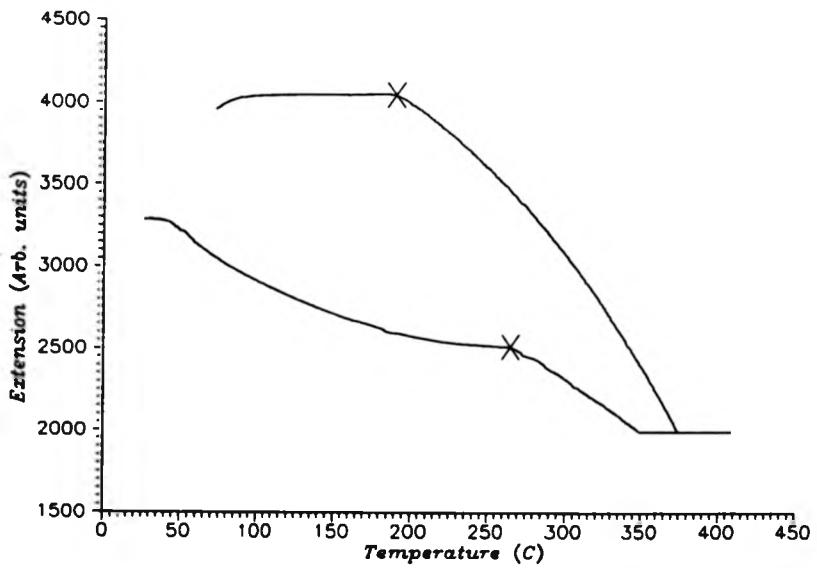

Figure 4.13b Thermal expansion data for the sample with 30ppm hydride

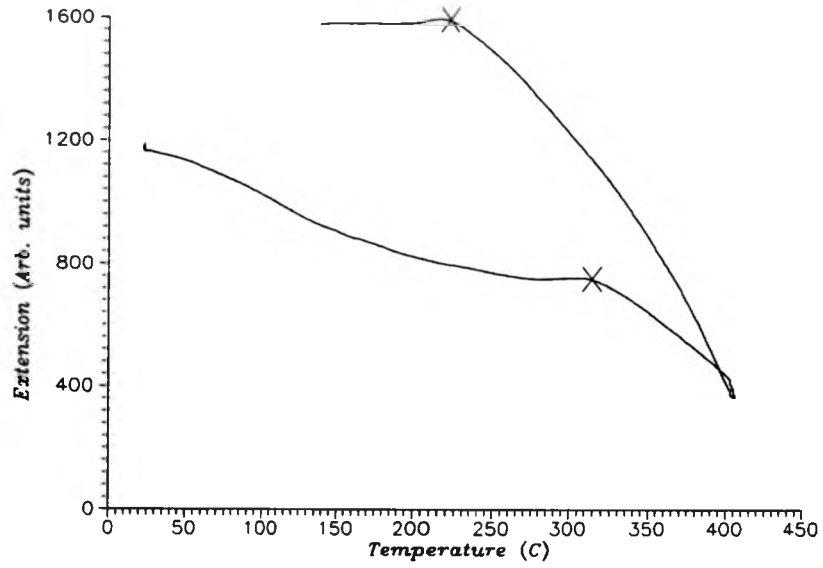

Figure 4.13c Thermal expansion data for the sample with 60ppm hydride

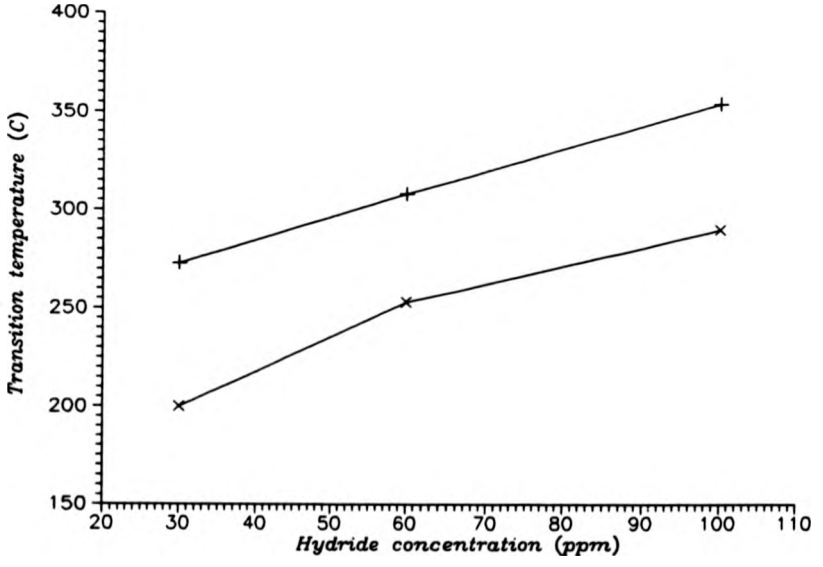

Figure 4.14 Zirconium hydride solid solubility temperatures measured by thermal expansion, (+) representing the measurements taken on heating, and (×) representing the measurements taken on cooling

the results obtained are shown as + on heating and as × on cooling. It is seen that the values of SST estimated from thermal expansion effects increase as the hydride concentration increases, as expected. As mentioned above, in all cases the transition temperature on heating is at a higher temperature than on cooling. This results from thermodynamic considerations, and would be an expected effect. In addition, the rate of heating and cooling would also be expected to affect the transition temperature. The effect of varying the cooling rate was investigated using the 60ppm sample, and the results obtained from this study are illustrated in Figure 4.15. This indicates that the measured SSTs increase as the cooling rate decreases, as expected. The cooling rate of 1.5°C per minute was used in other dilatometry experiments, as this was the slowest cooling rate that could be used on all of the samples, using the apparatus available.

The ultrasonic and dilatometry measured SST's (for cooling) are shown on one graph in Figure 4.16, with the ultrasonic results marked ×, and the dilatometry results marked +. The graph shows that the two sets of data are consistent. The temperatures at which these transitions take place are also consistent with results obtained by other workers in the field, summarised in Figure 4.1. It should again be noted that the ultrasonic data is dominated by effects due to ultrasonic velocity variations, rather than to thermal expansion changes, which are orders of magnitude too small to account for the observed change in arrival time gradients. It is interesting to note, however, that dimensional changes could still be observed by dilatometry with appropriate instrumentation. We thus have two independent methods for estimating the effect of phase transitions due the presence of hydrogen in zirconium alloys.

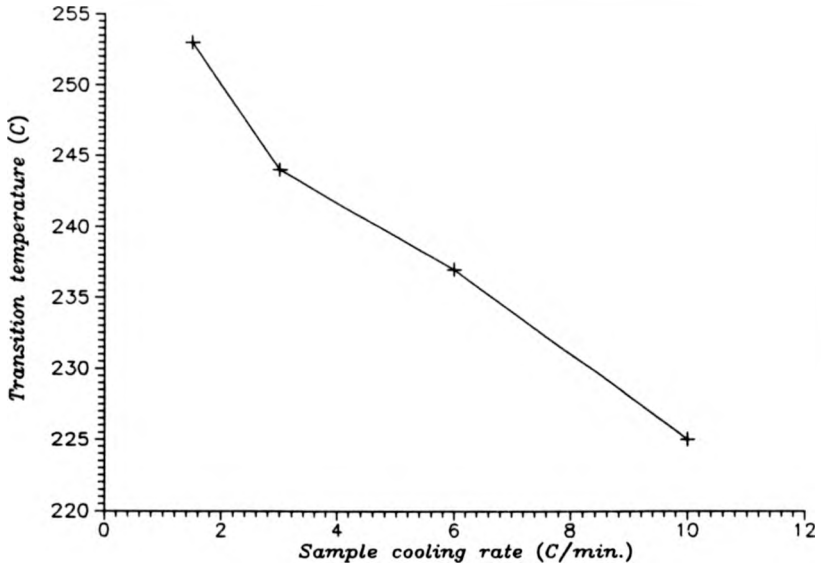

Figure 4.15 The effect of cooling rates on measured solid solubility temperatures for the sample hydrided to 60ppm

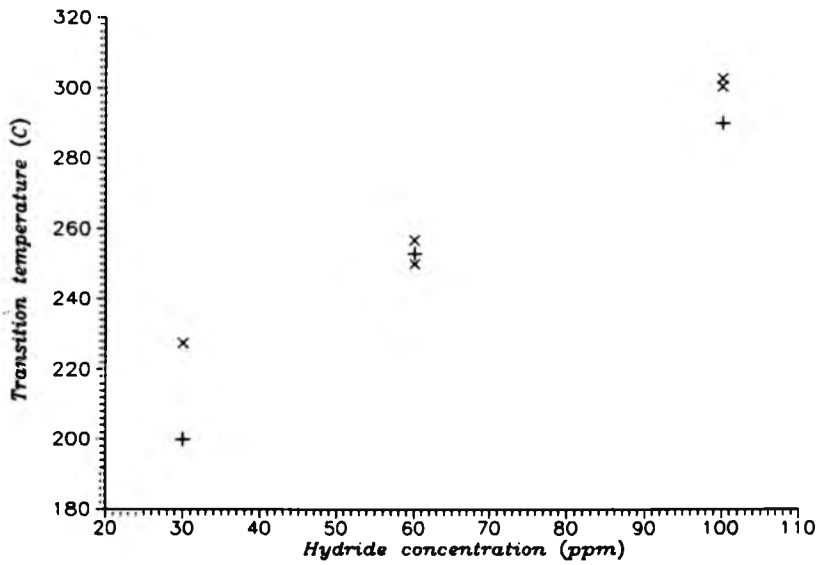

Figure 4.16 A comparison between the transition temperatures observed by both ultrasonic velocity measurements (×) and dilatometry measurements on cooling (+)

By comparing the thermal expansion of the zircalloy samples with that of a platinum sample with a known thermal expansion coefficient, an idea of the magnitude of the zircalloys' thermal expansion coefficient was estimated. This was found to be about 6×10^{-6} °C^{-1}, and compared well with values quoted in the literature[20]. Calculations using this figure showed that effects of expansion and contraction are sufficiently small that they did not unduly affect the ultrasonic measurements.

4.4 Conclusions

A pulsed laser source and specially designed EMAT detectors have been used to investigate the change in ultrasonic velocity with temperature in zirconium alloy samples, for both shear and longitudinal waves. This was performed over a temperature range from room temperature to 400°C. The EMATs were developed to operate at continuous temperatures of up to 550°C, without the need for external cooling. The shift in time of both shear and longitudinal wave arrivals on cooling of the sample was used to show a phase transition in various hydrided zircalloy samples. The temperature at which these transitions occurred was consistent with previous metallurgical studies, and may be used to estimate the room temperature hydride concentration within the alloy. A dilatometer was also used to observe a change in the thermal expansion coefficient of hydrided zircalloy samples, at temperatures related to the predicted phase transitions for the individual samples, forming the basis for a separate measurement.

For either of the above physical effects to be used practically, test methods

using these phenomenon will have to be developed to be able to inspect the pipe wall from inside the pressure tubes (of 94.6mm inside diameter and 6m long), through a layer of corrosion, and whilst the tubes are in situ inside a nuclear reactor (a highly radioactive environment). Test methods will have to be both reliable and economical, and must be able to either inspect large areas in full, or must be applied to a sufficient number of points along the tube to allow confidence in the tube's integrity. Future work will indicate whether these effects can form the basis for a practical measurement.

4.5 References

1. V.Perovic, G.C.Weatherly and C.J.Simpson, "Hydride precipitation in α/β zirconium alloys", Acta metall. Vol 31, No.9, pp. 1381-1391, (1983)
2. G.C.Weatherly, "The precipitation of α-hydride plates in zirconium", Acta metall. Vol 29, pp. 501-512, (1981)
3. W.L.Mudge, Jr., "Effect of hydrogen on the embrittlement of Zirconium and Zirconium-Tin alloys" in Zirconium and zirconium alloys (ASTM, Cleveland, Ohio, 1953), pp. 146-167
4. M.D.C.Moles and S.M.Kramer, "Ultrasonic measurement of hydride platelet concentration in zirconium pressure tubes", ASME pressure vessels and pipeline conference, Honolulu, Hawaii, July 23-27, 1989, Ed. R.D.Streit, pp. 205-211.
5. C.J.Smithells and E.A.Brandes "Metals reference handbook", Butterworths, 1976
6. V.Perovic and G.C.Weatherly, "The nucleation of hydrides in a Zr-2.5 wt%

Nb alloy", J. Nuc. Mat., 126, pp.160-169, (1984)

7. V.Perovic, G.C.Weatherly and C.J.Simpson, "The role of elastic strains in the formation of stacks of hydride precipitates in zirconium alloys", Scripta Metallurgica 16, pp.409-412 (1982)

8. C.E.Coleman and J.F.R.Ambler, "Solubility limit of hydrogen in zirconium alloys", Seminar on Fuel Channel Technology, Toronto, Ont., June 1981.

9. reference for SST-hydride concentration graph (Fig.4.2)

10. D.A.Hutchins, "Ultrasonic generation by pulsed lasers", in Physical Acoustics Vol. XVIII (Academic Press, New York, W.P.Mason and R.N.Thurston, eds., 1979), pp.277-407

11. D.A.Hutchins and D.E.Wilkins, "Elastic waveforms using laser generation and electromagnetic acoustic transducer detection", J. Appl. Phys., Vol. 58, pp. 2469-2477, (1985)

12. P.T.Cole, "The generation and reception of ultrasonic surface waves in mild steel at high temperatures", Ultrasonics, pp. 151-155, July 1978

13. B.W.Maxfield, "Using EMATs for high temperature ultrasonics", Proceedings, American Institute of Mechanical Engineers, Chicago, Il., 1984, Mechanical working of iron and steel, pp. 289-298

14. B.W.Maxfield, A.Kuramoto and J.K.Hulbert, "Evaluating EMAT designs for selected applications", Mat. Eval., Vol. 45, pp. 1166-1183, (1987)

15. L.Espagno, P.Azou and P.Bastien, "Etude dilatometrique du systeme zirconium-hydrogene", Memoires Scientifiques Rev. Metallurg. 57, pp. 254-259 (1960).

16. F.D.Manchester and G.C.Weatherly, "The terminal solid solubility of

hydrogen in Zr-2.5 wt.% Nb pressure tube alloys", Final report for Ontario Hydro Research contract, 1979.

17. F.M.Cain, Jr., "A simplified procedure for the metallography of Zirconium, and Hafnium and their alloys", In Zirconium and zirconium alloys (ASTM, Cleveland, Ohio, 1953), pp. 146-167

18. R.B.Thompson, "Physical principles of measurements with EMAT transducers", in Physical Acoustics, Vol.XIX (Academic Press, New York, W.P.Mason and R.N.Thurston, eds., 1990) pp. 157-200

19. Horowitz and Hill "The art of electronics", second edition, (Cambridge University press, 1989).

20. Miller, "Zirconium", second edition, (Butterworths, London, 1957)

21. D.R.Billson and D.A.Hutchins, "Ultrasonic shearwave measurements of phase transitions in zircalloy at elevated temperatures", Rev. Prog. Quant. NDE., Vol.12, New York, (1993), pp.1661-1666

CHAPTER 5

DEVELOPMENT OF NOVEL TRANSDUCERS

5.1 Introduction

During the course of the research that was undertaken for this thesis, there arose a need for ultrasonic transducers that could not be obtained commercially. Some of these transducers, such as the high temperature EMATs described in chapters 4 and 5, and the apertured EMAT used with a laser beam in chapter 4, were successfully developed and manufactured, and were adequately described in previous chapters. A number of other transducers were developed during the course of this research that are not described elsewhere in this thesis, and are thought to be sufficiently interesting to be included in this chapter. These transducers include a couplant-free (or "dry coupled") transducer, three novel types of ultrasonic airborne transducers, and an optical device for characterising the ultrasonic airborne transducers.

The "dry coupled" transducer is essentially a conventional 5MHz centre frequency, normal incidence, longitudinal wave piezoelectric transducer that does not need a couplant. This is achieved with a new low loss, synthetic rubber delay line, which is sufficiently compliant to be able to couple ultrasonically to a variety of test samples. Other "dry coupled" transducers have been manufactured in the past, but this transducer is novel in that it operates at 5MHz, which is a much higher frequency than has been possible with previous "dry coupled" probes. Experiments are presented using this transducer, which is shown to give good results when used in the pulse-echo mode on various samples of industrial interest.

The ultrasonic airborne transducers described here work on a different principle to the more commonly used airborne ultrasonic transducers. Two of the

new transducers use Lorentz effects (a moving conductor in a magnetic field) to convert the ultrasonic energy into electrical energy, and vice-versa, and the third is based on capacitance effects. There are two designs of the Lorentz type of transducer considered; in the first, a hand wound coil is placed very close to a thin aluminium membrane, and in the second, a coil is etched onto an aluminised polymer membrane. The novel capacitance transducer is manufactured from a mica wafer, and uses delaminated mica layers rather than a separate membrane as the ultrasonic source. The designs, theory and experimental results obtained with these transducers are described.

It was found that the ultrasonic waves generated by the new air transducers could not be satisfactorily characterised by the existing transducers, due to their natural resonant characteristics and corresponding narrow bandwidths. This led to a decision to develop a transducer that did not exhibit these limitations. The result of this is an optical detector that uses the change of refractive index in an airborne ultrasonic wave to vary the reflectivity at a glass-air interface. The designs of this detector, together with the theory and experimental results obtained with it are presented in this chapter.

5.2 A novel dry coupled transducer

5.2.1 Background

Ultrasonic testing is one of the established methods for the nondestructive testing (NDT) of materials and structures. In the usual implementation of the technique, a piezoelectric ultrasonic transducer (or probe) is applied to the surface, and in the pulse-echo mode acts as both source and receiver[1,2]. The necessity of using a liquid couplant with ultrasonic contact probes during this process can be a nuisance, and indeed precludes the use of this technique in many applications. For example, the use of a couplant might be unacceptable because of the danger of contaminating the component under test. In addition, use of a couplant might be a disadvantage when hazardous materials are tested, as the used couplant could itself become dangerously contaminated, and would require disposal which could be both expensive and environmentally undesirable. It is anticipated that couplant free probes will be of particular use with ultrasonic thickness gauges, as applying and removing couplant from a large number of samples represents a time consuming, and therefore costly part of the testing procedure. A number of transducer designs exist which can be used to both generate and detect ultrasound in materials without the use of a couplant. These are often referred to as "dry coupled" probes. Existing commercial devices based on contacting piezoelectric transducers either attempt to impedance match the device to a solid, using a rigid polymer layer, or use a very lossy rubber. The former design is relatively inefficient, whereas the latter can only be used at relatively low frequencies and with a poor bandwidth, because of losses in the rubber material. There are, however, other existing designs which do not rely on

contact to the material at all. Some are air-coupled devices, whereas others use optical or electromagnetic methods. These methods, although well suited to the laboratory, are rarely applied in an industrial environment because of factors such as cost, safety and convenience.

The vast majority of conventional ultrasonic testing uses a contacting piezoelectric probe, and a liquid ultrasonic couplant. The couplant is necessary to reduce the possibility of an air gap existing between the transducer and the component under test. Because of the large acoustic impedance mismatch between air, and both the solid material under test and the probe, very little acoustic energy will be transmitted across even a small air gap, and so a liquid ultrasonic couplant normally has to be used in this gap between the transducer and the sample to reduce the acoustic impedance mismatches, and thus allow adequate transmission of the acoustic wave through the interface.

The effect of this process may be illustrated by reference to Figure 5.1, which shows the interface between two media with acoustic impedances, z_1 and z_2. The intensity transmission coefficient across the interface may be written as[1,3]

$$\frac{J_t}{J_i} = \frac{4z_1z_2}{(z_2+z_1)^2} \qquad (5.1)$$

where J_t and J_i are the transmitted and incident sound intensities respectively. The ratio J_t/J_i represents the proportion of the energy transmitted through the interface. Substituting the acoustic impedance values for steel and air into this equation, ($z_{steel} = 45\times10^6$Kg m^{-2}s^{-1}, $z_{air} = 430$Kg m^{-2}s^{-1}), we get a value of 3.8×10^{-5} for the transmission coefficient of the sound intensity at the interface. If we substitute water for the air in the above equation ($z_{water} = 1.5\times10^6$Kg m^{-2}s^{-1}), we

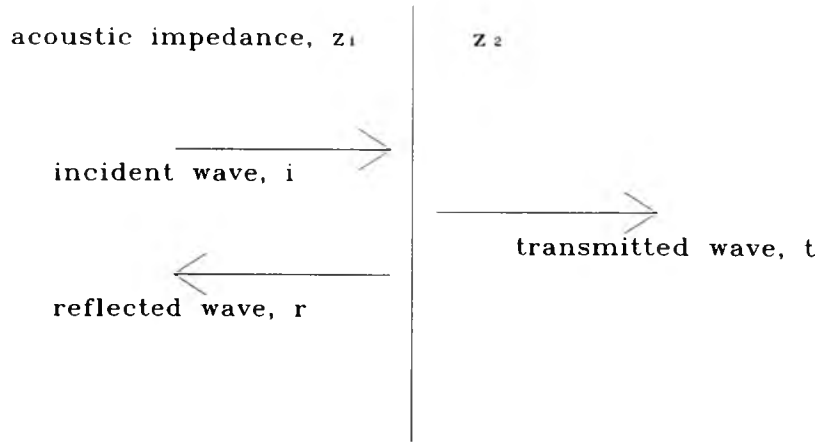

Figure 5.1 Reflection at an interface

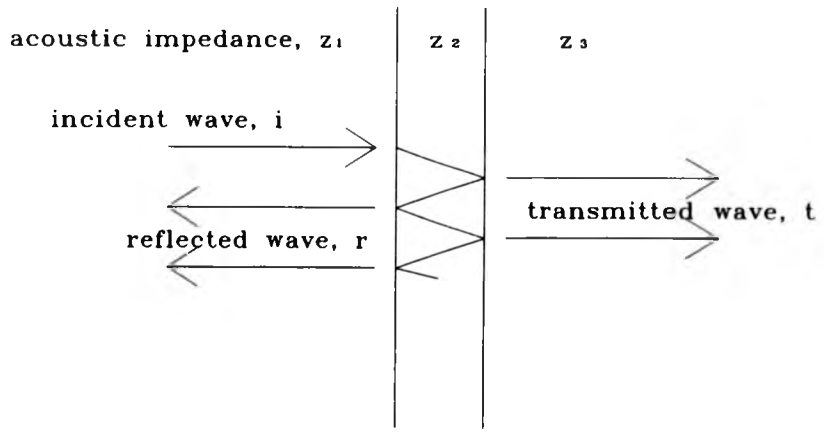

Figure 5.2 Reflection at a thin gap

get a value of 0.12 for the transmission coefficient. This shows that a water-steel interface presents much less of a barrier to the transmission of ultrasound than does an air-steel interface.

In the practical case of a transducer coupled to a solid via a layer of third material, a more complicated expression can be used for transmission through a layer of thickness L and impedance z_2 between two thick materials of impedances z_1 and z_3 (see Figure 5.2), written as[4]

$$\alpha_t = \frac{4z_3z_1}{(z_3+z_1)^2\cos^2 k_2L + \left(z_2+\frac{z_3z_1}{z_2}\right)^2 \sin^2 k_2L} \qquad (5.2)$$

where k_2 is the wavenumber in the layer medium at the particular frequency of interest, and is given by $k_2 = 2\pi/\lambda_2$, where λ_2 is the wavelength in the layer.

There are several important implications of this equation. First, transmission is optimised when the thickness $L = n\lambda_2/2$, where n is an integer, although imperfect transmission will still result if z_1 and z_3 are not the same. Perfect transmission can, in fact, be achieved using a quarter wavelength thick layer (sometimes called a matching layer) of impedance $(z_1z_3)^{1/2}$. In the case encountered in coupling a transducer to the solid, these conditions are rarely satisfied, and the full expression must be used. This predicts that a big difference in impedance between the layer material and that of the surrounding media leads to low transmission from medium 1 to 3, a condition that is met if air is trapped between the transducer and a solid material. This can only be mitigated if the layer thickness is made extremely small. To see the effect of this, consider the transducer and sample to be of the same acoustic impedance (that of steel) with

an air gap between them. A prediction of the transmission coefficient as a function of thickness for very thin layers of air is shown in Figures 5.3a and 5.3b for a 5MHz continuous ultrasonic wave. It is seen that, in order to enable a reasonable transmission of ultrasound through the gap, a thickness of less than 10^{-8}m would have to be maintained. This could not be achieved on practical samples without a prohibitive cost factor. It should be noted that this function does not take into account the finite bandwidth of ultrasonic pulses, which would require the application of more complicated mathematical techniques, involving finding the impulse response of a layered system using an approach such as that of Brekskovikh[5].

5.2.2 Experimental method and preliminary design

(a) The basic design of the transducer

As alluded to above, it would be impractical to get two solid surfaces polished sufficiently to reduce the air gap between transducer and sample to a point where conventional testing is possible. However, if the transducer surface was sufficiently compliant to allow the air in the gap to be squeezed out, and allow the surfaces to come into intimate contact, then this problem could be overcome. This is the basic advantage of using a compliant face on a transducer, and is adopted in the transducer design to be described in this paper. It should also be noted that the finite thickness of couplant used with conventional transducers makes the reproducibility of pulse-echo waveforms difficult (as the shape of an ultrasonic pulse transmitted through a couplant filled gap is very dependant on its thickness)[8,9]. By using a couplant-free transducer, and thus

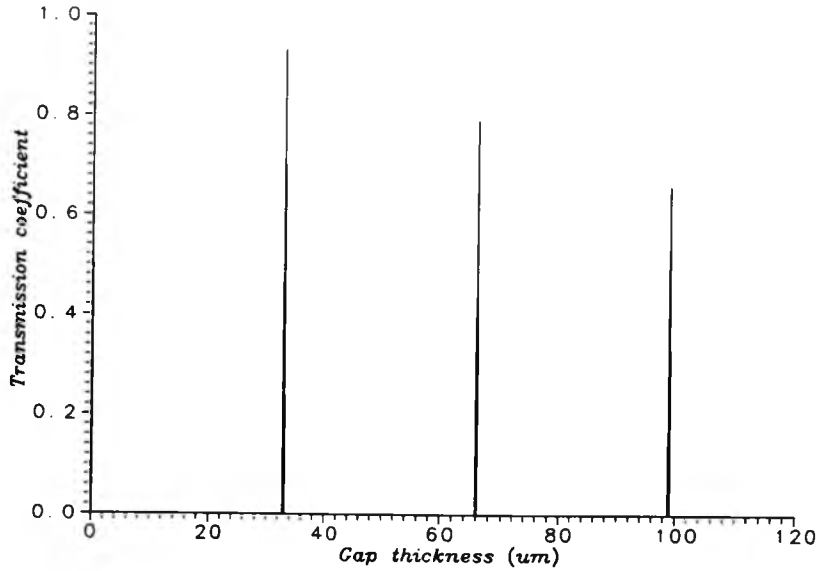

Figure 5.3a Transmittivity at a thin gap, varying gap thickness

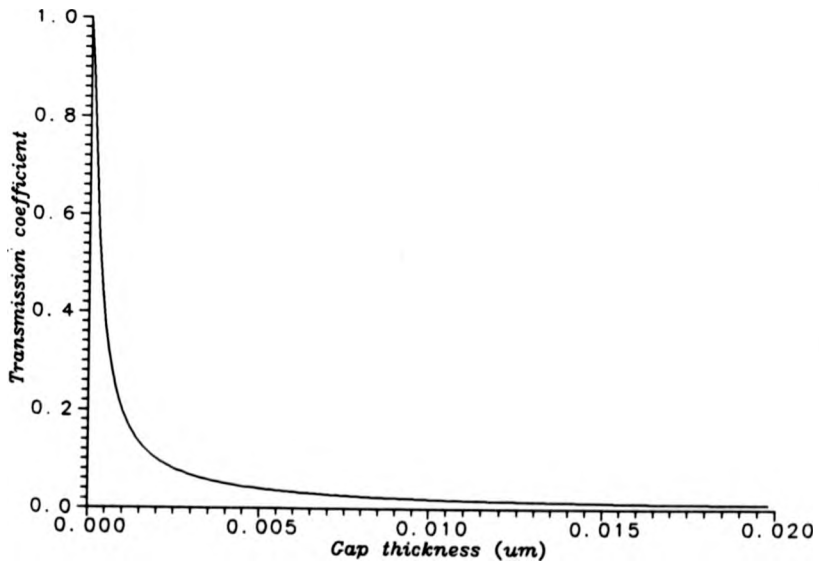

Figure 5.3b Transmittivity at a thin gap, expansion at small gap thicknesses

eliminating this gap, variations in transmitted pulse shape and bandwidth should be reduced.

To avoid reflections within the delay line masking signals from the sample, the transducer facing material needs to be thick enough for the first echo within the delay line to arrive after any relevant signals from the sample have arrived. Previous couplant free probes used materials which were highly attenuative of ultrasound at frequencies above 1MHz (natural rubber being a common example). This meant that low frequency, narrow band ultrasonic pulses had to be used to overcome this attenuation, the result being a poor quality pulse with very low resolution. A material has been discovered, however, that is both compliant and has very low ultrasonic attenuation at frequencies of up to 5MHz (compared with materials used previously). This has enabled a normal incidence, longitudinal wave transducer to be built, with a nominal centre frequency of 5MHz, capable of high quality nondestructive testing without a liquid couplant.

A schematic diagram of the transducer is shown in Figure 5.4. This used a commercial piezoelectric material (PZT) as the active element, backed with tungsten-loaded epoxy to provide damping (and hence increase the bandwidth and decrease the pulse-length). The nominal centre frequency of operation was 5MHz. The low loss rubber material was then used to fabricate a delay-line to the sample under test, which operated without couplant on the sample surface. The whole assembly was mounted in an earthed case, to which the usual connectors were attached, and electrical matching was provided for the transducer element. The device operates as a conventional transducer fitted with a delay line, and could act in either through-transmission or in pulse-echo mode.

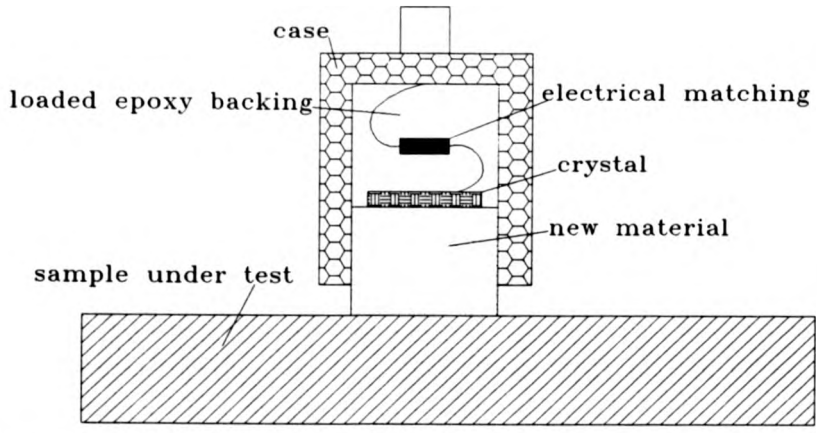

Figure 5.4 Schematic diagram of the couplant-free probe

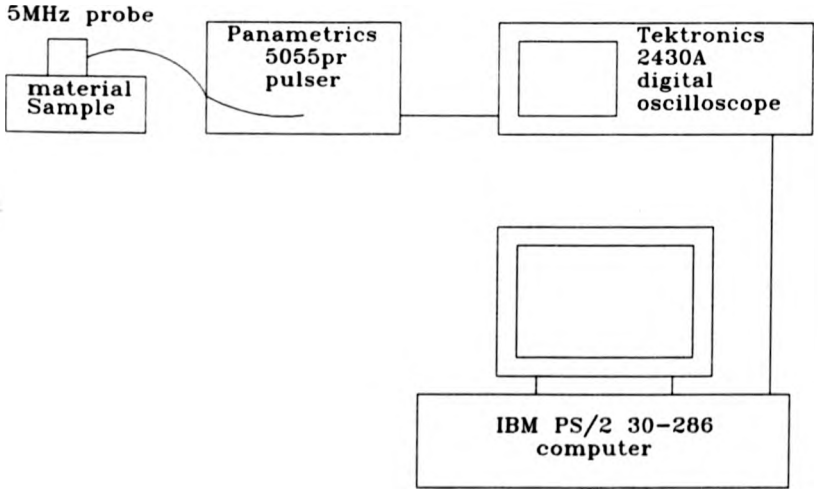

Figure 5.5 Experimental configuration to compare the attenuation of the new material against natural rubber

(b) Tests of delay line characteristics

The operation of any similar device is very sensitive to the acoustic propagation characteristics of the delay line material, and hence a series of tests were performed to estimate the ultrasonic attenuation of this new material, compared with that of a material used in a number of commercial couplant-free probes (natural rubber). These tests used a normal incidence broadband Panametrics 5MHz longitudinal transducer of ½" diameter, which was used in a pulse-echo mode to get a waveform through samples of different materials (Figure 5.5). The experimental set-up used a Panametrics 5055PR pulser/receiver, and the waveforms were recorded using a Tektronics 2430A digital oscilloscope, and transferred subsequently to an IBM PS/2 model 30-286 microcomputer for storage and analysis. Tests were performed on a standard aluminium sample, natural rubber and the present delay-line material, with typical sample thicknesses being 26±2mm. In all cases, a Fast Fourier Transform (FFT) was performed on the waveforms to give the corresponding frequency spectra.

The ultrasonic transmission response can be described by the following convolution[10];

$$V_0 * T(t) * R(t) = D(t) \qquad (5.3)$$

where $V_0(t)$ = pulser output

$T(t)$ = transducer time response

$R(t)$ = impulse response of the material

$D(t)$ = displacement signal

As a convolution of time responses is equivalent to multiplying the frequency spectra, we can obtain an equivalent expression in the frequency domain (in terms of frequency ω) from (3) to give

$$V_0(\omega)\times T(\omega)\times R(\omega)=D(\omega) \tag{5.4}$$

For aluminium we can write

$$D_A(\omega)=V_0(\omega)\times T(\omega)\times R_A(\omega) \tag{5.5}$$

whereas for the new material we get

$$D_M(\omega)=V_0(\omega)\times T(\omega)\times R_M(\omega) \tag{5.6}$$

Dividing (5) by (6)

$$\frac{D_A(\omega)}{D_M(\omega)}=\frac{R_A(\omega)}{R_M(\omega)} \tag{5.7}$$

The assumption is now made that the attenuation at the frequencies of interest in the aluminium sample is negligible, i.e that the time response of the aluminium sample is a delta function, and hence that its spectrum is flat, so that

$$R_A(\omega)=1 \tag{5.8}$$

Therefore;

$$R_M(\omega)=\frac{D_M(\omega)}{D_A(\omega)} \tag{5.9}$$

and the response of any other material in frequency is given simply by the division of its spectrum by that for aluminium. The effects of the pulser and the transducer response are removed, and other complications such as diffraction corrections are minimised.

Figure 5.6 shows time waveforms recorded with the apparatus of Figure 5.5, for samples of the new material and natural rubber. The first back-wall echo from each sample is shown, and it is immediately evident that the received amplitude was much more highly attenuated in the natural rubber sample. (Note that the velocities and densities (and hence acoustic impedances) of the two materials were very similar, and hence the acoustic impedance mismatch between the Panametrics transducer and each sample would also be similar, allowing a direct comparison of amplitudes to give qualitative information). This can also be illustrated by windowing the backwall echo and performing an FFT to get the received spectra of Figure 5.7. Again, qualitatively it is clear that the new material affected the transmitted broadband acoustic pulse to a much lesser degree.

More quantitative information was then obtained, using the procedure above, where comparison was made with an aluminum sample via equation (9). The result was the attenuation curves for the two materials given in Figure 5.8. It is seen that the ultrasonic attenuation curve of the new material is superior to that of natural rubber. The latter exhibits high attenuation at frequencies in excess of ~1MHz, whereas the new material transmits ultrasound satisfactorily at frequencies of up to 5MHz, and would have a useful operational bandwidth up to 6MHz.

5.2.3 Results and discussion

An ultrasonic probe has been manufactured following the design of Figure 5.4, incorporating the new material as a delay line. The performance of this device has been investigated on some common engineering materials, and has

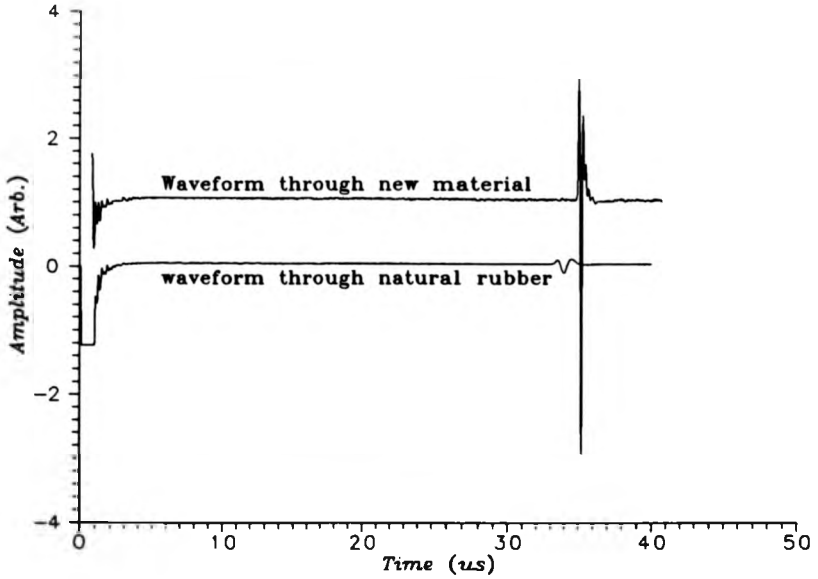

Figure 5.6 Ultrasonic waveforms after propagating through probe material samples

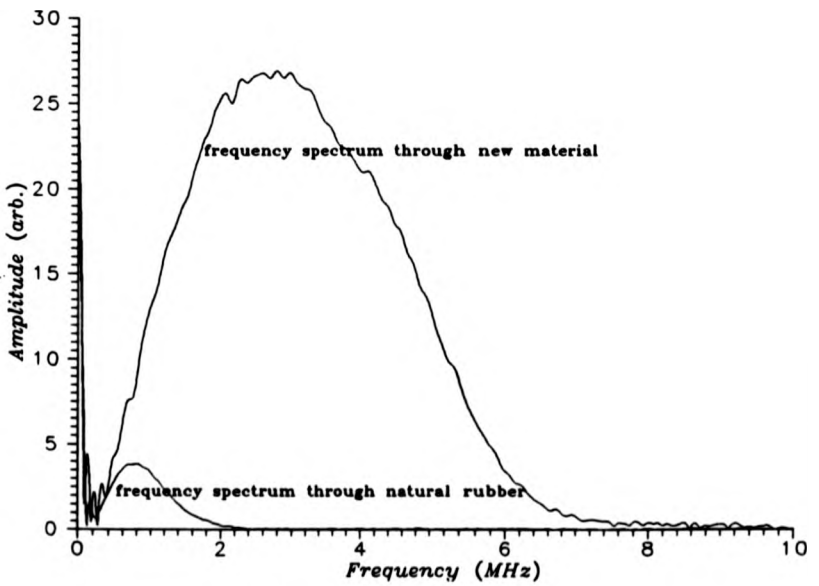

Figure 5.7 Frequency spectra after propagating through probe materials

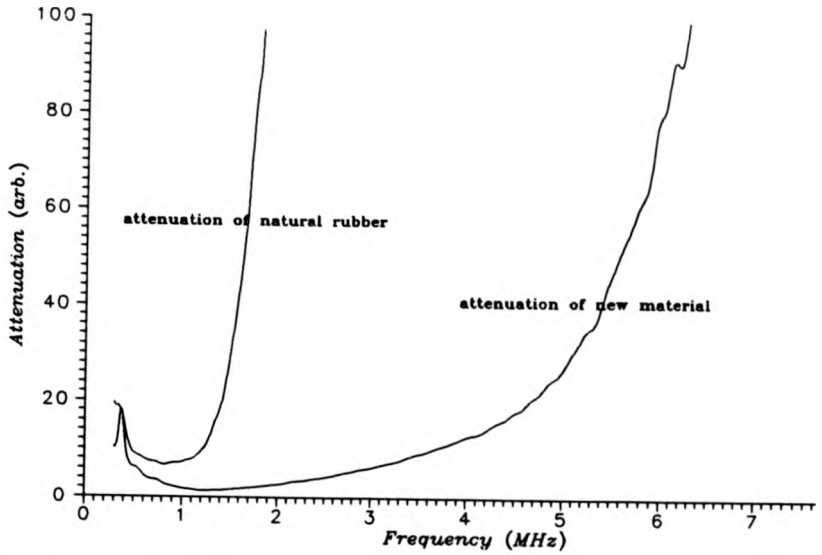

Figure 5.8 Attenuation curves of the probe materials

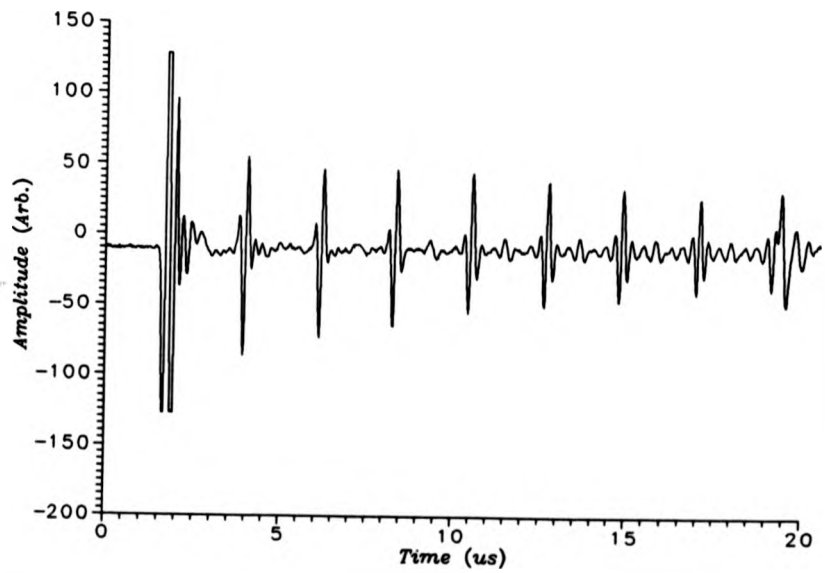

Figure 5.9a Ultrasonic waveform taken with the new probe through a 6.44mm thick steel plate

then been used to perform ultrasonic NDT tests on various samples, without using a couplant between the probe and the sample.

The first tests were performed to establish the performance of the device on some common materials of industrial interest. The experimental set-up used a Panametrics 5055PR pulser/receiver connected directly to the probe, with received waveforms being recorded on a Tektronics 2430A digital oscilloscope before being transferred to an IBM PS/2 model 30-286 microcomputer. The first of the samples was a steel plate, 6.4mm thick, with an "as received" surface condition. The second sample was a welded sample of titanium, being comprised of two 3.5mm thick sheets, joined together in places by resistance welding. This sample also had an "as received" surface condition. The third sample was a 5.10mm thick plate of unidirectional carbon fibre reinforced polymer (CFRP) composite, the surface of which was smooth. The last sample was a block of aluminium, with a 3mm diameter hole drilled 43mm away from the top surface. The surface of this sample was typical for an extruded aluminium bar.

Typical waveforms from these samples, none of which were processed in any way, are shown in Figures 5.9(a) to 5.9(d). Figure 5.9(a) shows the waveform taken through the 6.4mm thick steel plate. The multiple reflections within the steel are clearly distinguishable, and occur well before the first reflection within the delay line (which is apparent towards the right of the waveform). It should be noted that a delay has been introduced into the waveforms, and the first signal in the waveforms is the first reflection from the delay-line to sample interface. Figure 5.9(b) shows the waveform obtained through the welded section of the titanium sample, where similar features are evident. In Figure 5.9(c), the same

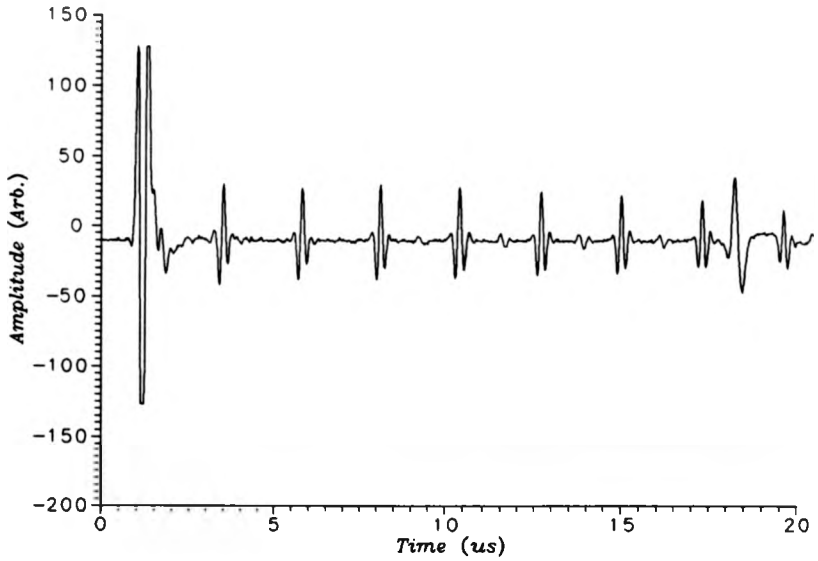

Figure 5.9b Ultrasonic waveform taken with the new probe through a resistance welded titanium sample, test done in the center of the weld

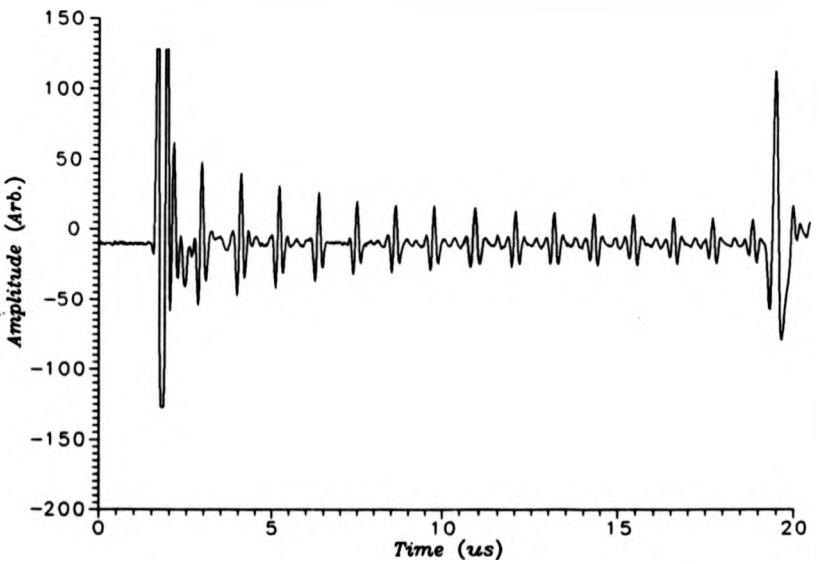

Figure 5.9c Uitrasonic waveform taken with the new probe through a resistance welded titanium sample, test done away from the center of the weld

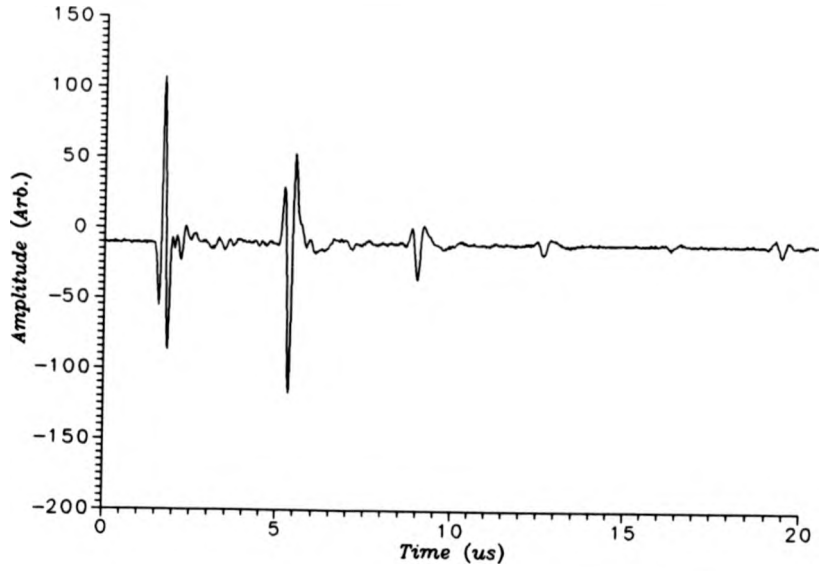

Figure 5.9d Ultrasonic waveform taken with the new probe through a 5.10mm thick CFRP plate

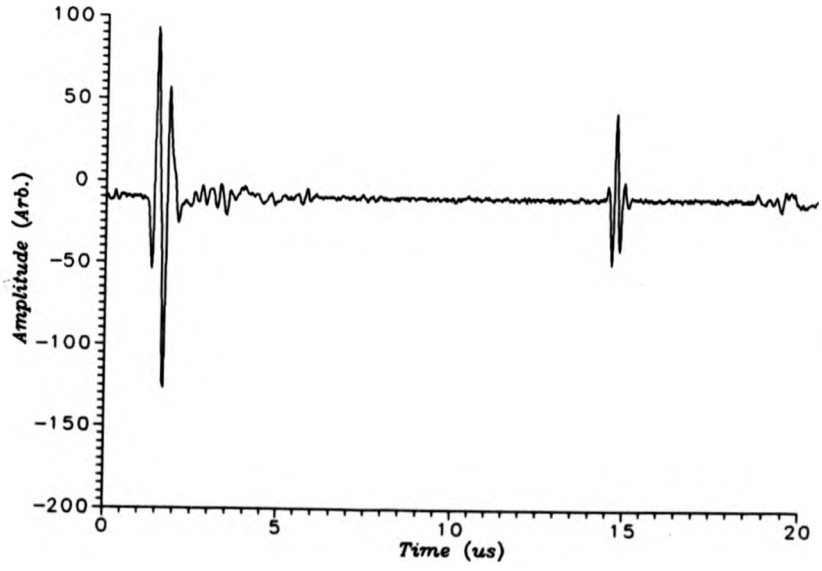

Figure 5.9e Ultrasonic waveform taken with the new probe on an aluminium sample with a 3mm hole drilled 43mm from the surface

sample is tested, but away from the centre of the weld. Here the multiple refections are more closely spaced, indicating that the ultrasound is reflecting from an interface between the plates, showing that they have not been joined by the welding process. Figure 5.9(d) shows multiple reflections within the CFRP plate. Attenuation within the CFRP is now evident, with only 3 or 4 multiple reflections being present. These are, however, still clearly visible. Lastly Figure 5.9(e) shows the reflection from a side drilled hole in aluminium, this shows that the probe could be used for defect detection as well as for thickness gauging. The waveforms in Figure 5.9 show that the new probe can be used to obtain high quality ultrasonic waveforms in samples of interest in NDT, without using a couplant.

5.2.4 Application of couplant-free transducers to adhesive bond testing

The novel couplant free transducers described in this chapter were applied to the testing of adhesive bonds in the manner described in chapters 3 and 4 of this thesis. Couplant-free transducers are thought to be particular advantageous when used on adhesive bonds, as a number of adhesives cannot withstand contact with water, or other contaminating couplants.

The 5MHz couplant-free transducer was used to obtain longitudinal waveforms on adhesively bonded samples using a Panametrics 5055PR pulser-receiver, a Tektronics 2430A digitising oscilloscope, and an IBM model 30-286 computer. These were subsequently analyzed in the fashion described in chapters 3 and 4.

Examples of two of the waveforms obtained are shown in Figures 5.10a

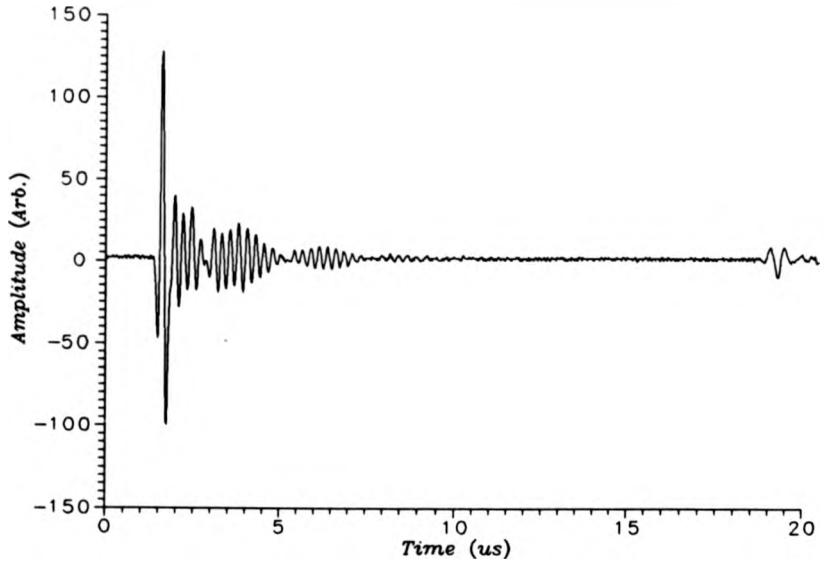

Figure 5.10a Ultrasonic waveform taken on a "good" portion of an adhesive bond with the new couplant-free transducer.

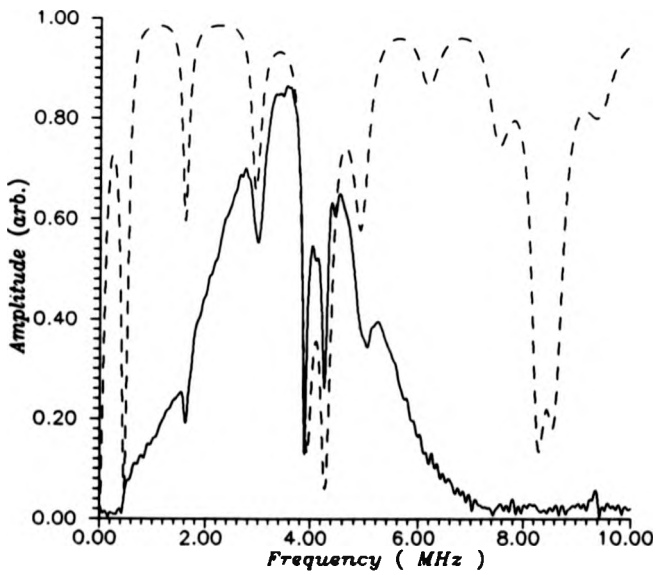

Figure 5.10b The frequency spectrum of the previous waveform (solid line), together with the frequency spectrum predicted for this bond (dashed line).

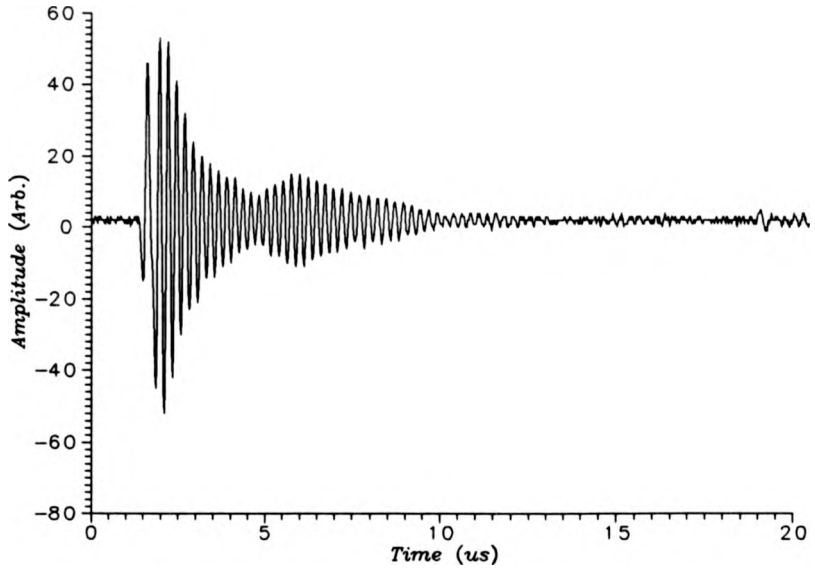

Figure 5.11a Ultrasonic waveform taken on a "bad" portion of an adhesive bond with the new couplant-free transducer.

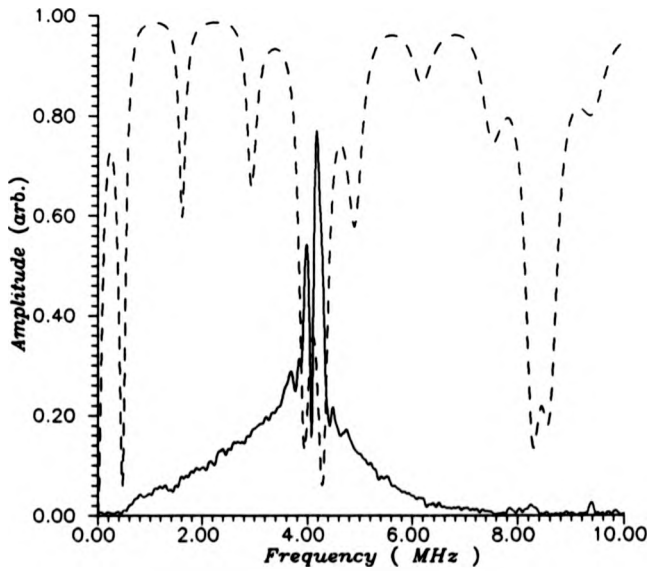

Figure 5.11b The frequency spectrum of the previous waveform (solid line), together with the frequency spectrum predicted for this bond (dashed line).

and 5.11a. These were taken on the same adhesively bonded structure (with 0.754mm aluminium adherends, and 0.84mm epoxy based adhesive), but the first waveform was taken on a "good" area of the sample, whilst the second waveform was taken on a "bad" area of the sample, (i.e. containing an artificially induced delamination at the lower adhesive-adherend interface). The waveforms appear strikingly similar, and by looking at these alone, no information pertaining to the state of the bond could be implied. This is not the case when considering the frequency spectra of these waveforms (shown in Figures 5.10b and 5.11b respectively). The frequency spectrum from the good area of the structure corresponds well with the predicted frequency spectrum (shown as the dashed plot in the same graph). This is not the case with the second spectrum from the "bad" area, which is completely different from the predicted frequency spectrum, having lost a number of resonances, and in this case being inverted. This shows that the couplant free probe can be used with spectroscopic analysis methods to clearly detect gross disbonds in adhesive bonds.

5.2.5 Conclusions

A novel couplant-free, high frequency (5MHz) contacting ultrasonic longitudinal wave transducer has been built using a new delay line material, and has been shown, using conventional techniques and flaw detecting equipment, to work well on samples such as steel, aluminium, carbon fibre composite and titanium. This probe has also been shown to provide excellent results when used to test adhesive bonds using the analysis techniques described in chapters 3 and 4 of this thesis.

The probe described above is now undergoing final development, and an improved model will be available commercially very shortly. Also under development are twin crystal probes, and roller probes which are hoped to be available commercially later this year.

5.3 Novel ultrasonic air transducers, and a novel optical detector for their characterisation.

5.3.1 Background

Airborne ultrasound is used by bats for distance ranging at night, in contrast to humans who have used airborne ultrasound for only the last half century or so, for devices such as television remote-control systems, motion sensors for intruder detection systems, and for distance ranging devices (commonly used by estate agents for measuring the dimensions of rooms). These applications required ultrasound at frequencies below around 200kHz. In more recent years, interest has grown in the exploitation of airborne ultrasound for high precision distance-ranging (for example for robotic applications), and for non-contacting nondestructive testing. This has generated a requirement for transducers that operate at increasingly higher frequencies, and with much higher sensitivities.

The author's interest in these transducers (in the context of this thesis) is for non-contacting, nondestructive testing of difficult materials; specifically adhesive bonds, and zircalloy. To allow non-contacting testing of the adhesive bonds investigated in chapters 3 and 4, frequencies of at least 2MHz will be necessary (and 10MHz would be desirable), together with a useable sensitivity.

This is not achievable with current technology, though it is hoped that air transducers might be developed sufficiently in the near future to facilitate their use for the nondestructive testing of adhesive bonds, the novel transducers described here attempt to contribute to the development of such transducers. For zircalloy, not only will the transducers have to perform as described above, but they will have to do this in an extremely hostile environment (a hot, radioactive nuclear reactor) to be effective. To this end, two transducers have been investigated that could be suitable for this environment.

The principal of using airborne ultrasound for nondestructive testing seems, in the first instance, to be ideal for a variety of non-contacting applications. This technique has, however one major flaw, namely that of transmitting ultrasound across the interface between the air and the sample under test. Because of the very large acoustic impedance mismatch between most solids and air, only a very small proportion of the ultrasonic energy is transmitted across this boundary. This is compounded when testing materials with the transducer acting as both transmitter and receiver, as the ultrasonic signal needs to cross the boundary between air and the sample twice, introducing significant losses, often prohibitively, into the received signal. Because of these massive losses, most samples cannot currently be tested in such a way. However, experiments have shown that nondestructive testing with airborne ultrasound can now be usefully employed in three situations; Firstly if another method (for example a laser) is used to generate the ultrasound (removing the losses encountered at one interface)[13]. Secondly, when materials with low acoustic impedances (such as paper and wood) are tested. Thirdly where the air is under high pressure

(increasing the acoustic impedance of the gas). This latter situation is of particular interest to the gas pipeline-pigging industry, where gas pipelines need to be tested in service for corrosion thinning, the pipes conveniently having gas pressures of up to 200 bar inside them. A working airborne ultrasonic system could overcome many of the coupling problems encountered when using ultrasound (currently, most testing of these pipes is done by magnetic flux leakage techniques).

Both nondestructive testing, and distance ranging require much higher sensitivities and frequencies than have been necessary in the past, leading to a requirement for transducers that fulfil these criteria. This has instigated research in this field by a number of groups throughout the world[14], who have generally concentrating on two main competing designs for such transducers, commonly referred to as piezoelectric composite, and capacitive membrane transducers. It is hoped that the work described here will contribute to this field by introducing three new types of transducers.

The piezoelectric composite transducer attempts to match the impedance of a piezoelectric transducers' active element to air. This is usually achieved by using a piezoelectric ceramic\polymer composite material, the characteristics of which can be modified to optimise either generation or detection characteristics, further improvements have been made to this type of transducer by the addition of matching layers to the front face made from a wide variety of materials. Whilst this increases sensitivity of the device, this usually results in a more resonant waveform, giving a correspondingly narrower bandwidth[15-20] .

The capacitive transducer (which is arguably more sensitive than the

piezoelectric composite transducer) uses an electrostatic mechanism, comprising of a solid electrically-conducting backplate, and a thin polymer membrane (metallised on its front face). The device operates on electrostatic forces; when a transient voltage (usually in the form of a "top hat function") is applied between the backplate and the metallised membrane, a force results. This force is attractive if the charge on the two conductors is opposite, and repulsive if the charges are similar. The force moves the membrane, resulting in ultrasonic generation. With these devices, an air layer is usually engineered between the backplate and membrane, which can significantly affect the performance of the device in ways that are not yet fully understood. This air layer is created by either roughening the backplate, or by etching pits into the backplate. Often, a d.c. (bias) voltage is applied between the backplate and membrane, pulling the membrane taut into the backplate. This changes both the mechanical properties of the membrane, and the form of the air layer beneath the membrane, and usually has the effect of increasing both the bandwidth, and the sensitivity of these devices[21-28].

Two of the new types of air-transducer described here use electro-magnetic forces (Lorentz forces) to convert ultrasonic motion to an electrical signal. The third type of transducer operates as a source in a similar way to the conventional capacitance transducers, but is different in that it is manufactured from a single wafer of mica. The optical detector was developed to characterise the airborne transducers, and measures the change in the refractive index of air (caused by an ultrasonic wave) at an air-glass interface.

5.3.2 Theory and design of the novel air transducers and the optical detector

(a) The Lorentz air transducers

The electromagnetic theory behind the novel air transducers is analogous to the theory of operation of the EMATs described more fully in chapter 2 of this thesis, and the reader is therefore referred back to this chapter for a more complete understanding of these air transducers.

To understand the operation of the first of the transducers (which will subsequently be referred to as a Lorentz-foil transducer), consider the schematic diagram in Figure 5.12. This shows an *aluminium membrane* above a *coil* in a *magnetic field*.

Consider first the situation where the transducer is used as an ultrasonic receiver. The airborne ultrasound impinges on the aluminium foil, causing it to move. As the foil is moving in a magnetic field (generated by the Nd:Fe:B permanent magnets and modified by the steel pole piece), a current will be caused to flow within it (Lorentz). This current (by a process of mutual inductance) induces a current to flow within the coil wound below the foil, which can then be amplified to give a useful signal. This device can essentially be thought of as a longitudinal EMAT with a very thin sample in front of it. The device operates in a generation mode by passing a current pulse through the coil, which in turn induces a current to flow within the aluminium membrane. Because it is in a magnetic field, the membrane moves, thus generating airborne ultrasound.

The foil needs to be carefully designed, and aluminium was chosen as the material with which it was made, as this is both light (reducing the inertia of the

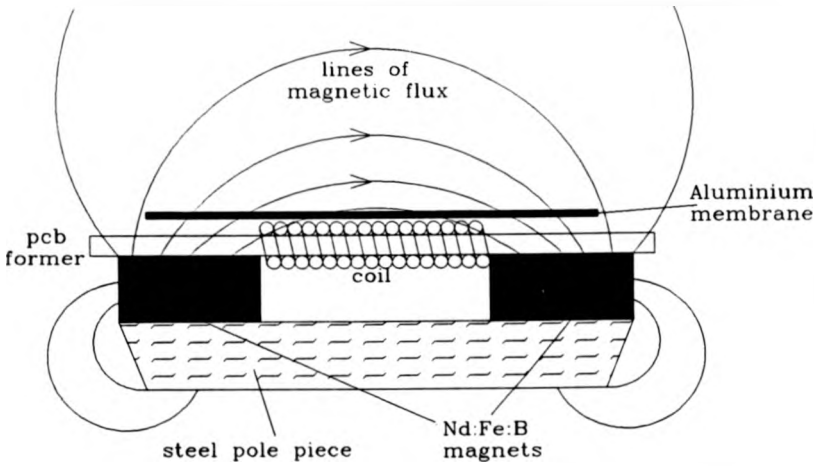

Figure 5.12 A schematic diagram of the Lorentz-foil airborne ultrasonic transducer.

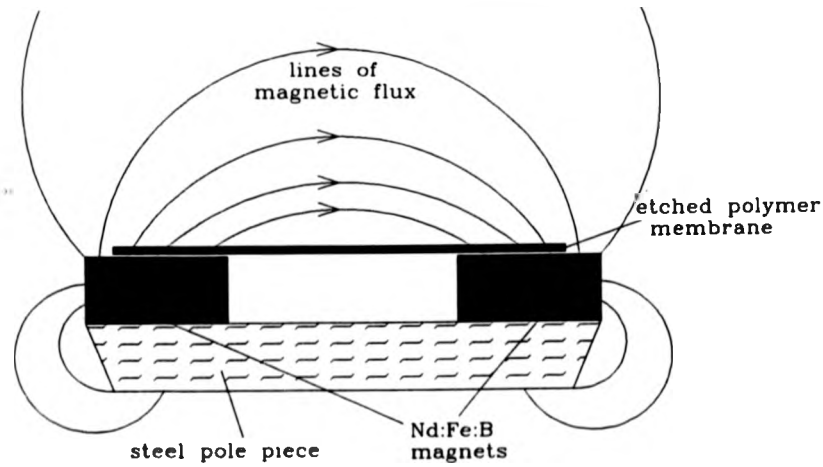

Figure 5.13 A schematic diagram of the Lorentz-membrane airborne ultrasonic transducer.

foil allows, in effect, a greater impedance matching to the air) and with high electrical conductivity (to allow a large current to flow within it without resistive losses). For similar reasons, the thickness of the foil needed to be carefully chosen as two competing processes affect the performance of the EMAT; the foil needed to be sufficiently thin to reduce its inertia, but needed to be sufficiently thick to allow a current to flow within it. As high frequencies are involved, the thickness of the aluminium can be can be thought of in terms of a "skin depth". The formula for skin depth, δ is given by Feynman[29] as:

$$\delta = \sqrt{\frac{2\varepsilon_0 c^2}{\sigma \omega}} \qquad (5.10)$$

where:

ε_0(permittivity of free space) $= 8.85*10^{-12}$ Fm^{-1}

c (speed of light in vacuo) $= 2.997*10^{8}$ ms^{-1}

σ (conductivity of Aluminium) $= 3.77*10^{7}$ $(\Omega m)^{-1}$

ω (angular frequency of the E.M. wave) $= 2\pi*10^{6}$ at 1MHz

This gives a skin depth of 82μm for aluminium at 1MHz. Experiments were undertaken with a variety of thicknesses of aluminium foil, showing that the optimum thickness for the foil is around 13μm, corresponding to about 16% of the calculated skin depth. Fortunately, quantities of foil of this thickness were readily available in the form of "Kit-Kat" wrappers.

The performance of the device was found to depend quite heavily on the number of turns in the coil; three effects had to be considered when choosing the coil parameters. Firstly increasing the number of turns increased the impedance

of the coil, limiting its bandwidth. Secondly reducing the number of turns reduced the amplitude of the signal from the device, and thirdly, the change in impedance encountered when varying the number of turns on the coil affected the electrical matching between the device and the preamplifier (or pulser), distorting the first two effects in a particularly complicated fashion. After much experiment, 120 turns was chosen as optimum for the coil in reception, and 20 turns was chosen as optimum for the coil in generation.

Many other factors affected the performance of the device, such as the magnet separation, the coil dimensions, and the coil-foil stand-off. These were optimised by hand, and then left constant for all of the experiments undertaken on this device; a full investigation into the factors affecting these transducers is a research programme in its own right, and time did not allow for their full investigation in this thesis, although it is hoped that research into this type of transducer will continue in the future.

The second design of the Lorentz transducers (which will be referred to as the Lorentz-membrane transducer) is schematically shown in Figure 5.13. The operation of this is similar to that of the previous transducer, but has replaced the wound coil and aluminium foil with a coil etched onto the front face of a thin polymer membrane. The design of the etch pattern that was used is shown in Figure 5.14; with this, the electrodes were attached to the two dark rectangles, and the active area was the area between these rectangles. (In this Figure, the dark areas were aluminised, and the blank areas were etched free of aluminium). This design improved on the last as the signal came from the membrane itself, and no eddy-current effects were needed to generate a current in a separate coil.

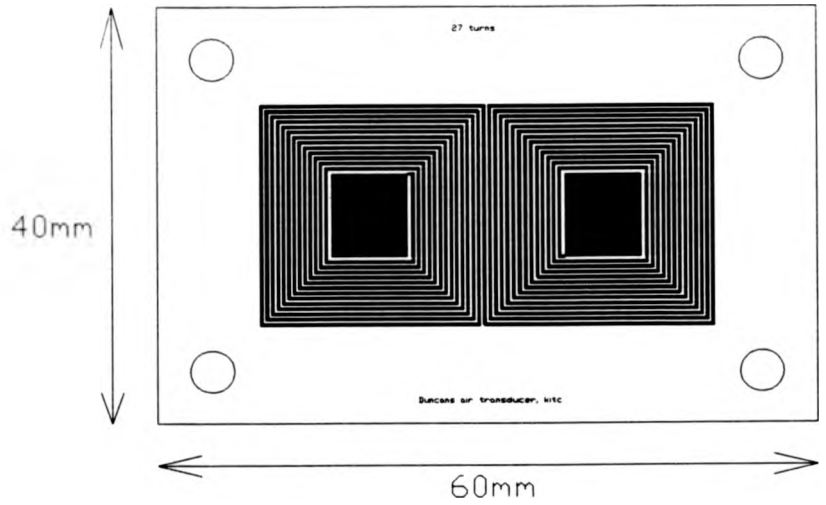

Figure 5.14 The etch pattern used for the polymer membrane in the Lorentz-membrane air-transducer.

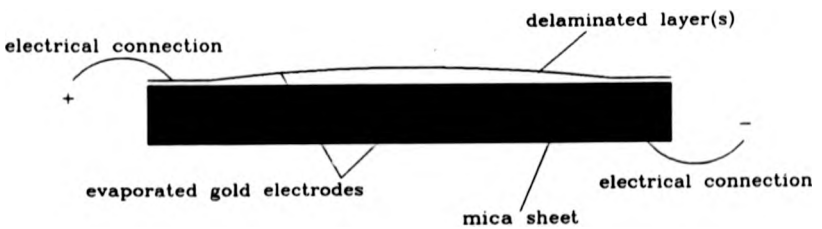

Figure 5.15 The ultrasonic transducer based on a mica sheet

This eliminated the need for large currents to flow in the foil, allowing a much thinner membrane than was practical with the previous device (increasing the bandwidth of the device, as well as improving its sensitivity). It has been suggested that this device is, in effect, a modified ribbon microphone.

(b) The mica-capacitance transducer

The mica-capacitance transducer is schematically shown in section in Figure 5.15. This operates in a similar way to the more conventional polymer-membrane capacitance devices, in that a voltage transient is applied between the upper and lower gold electrodes, either attracting (opposite polarities) or repelling (similar polarities) the two electrodes. This force acts on the delaminated layers, moving them, and therefore generating ultrasound.

Ideally, the delaminated layer (the "active" component of the transducer) should be a single molecule thick, maximising both sensitivity and bandwidth. The delamination in the transducer investigated here was made in a very crude way, involving placing the mica sheet in a butane flame; this delaminated the mica, but in an uncontrolled manner, resulting in a relatively thick, uneven active layer. Subsequent experiments have shown that (what appears to be) a very thin layer can be delaminated from the bulk by careful irradiation with a (pulsed) TEA CO_2 laser (this is strongly absorbed by the mica, causing thermal expansion of the uppermost layers, which produces the delamination). Obviously, a great deal of work remains to be done with these transducers, however these preliminary results are considered important enough to be included in this thesis.

Mica possesses three particular physical properties that make it an ideal material for the manufacture of air transducers; firstly it can be readily cleaved

(allowing thin delaminated layers to be easily produced), secondly it possesses a high dielectric breakdown strength, allowing large voltages to be applied across a thin layer, (allowing the mica transducer to be driven much harder than other devices) and thirdly mica can withstand both elevated temperatures and a high background radiation level (allowing it to be used in a hostile environment).

(c) The optical detector

A schematic diagram of the optical detector monitoring the ultrasonic airborne wave from a capacitive transducer is given in Figure 5.16. This diagram shows a He-Ne laser beam impinging on a glass prism, with the output from the air transducer aimed at the main face of the prism. The prism has been oriented to very nearly totally-internally-reflect the laser beam at its main face, and the transmitted beam (that is nearly extinguished at this angle) is detected on a photodiode. The optical detector works because, at the air-glass boundary, (the point where both the light beam emerges from the prism, and the ultrasound beam hits the prism), the reflection/transmission of light will change with the refractive index of the air. This will result in the amplitude of the light arriving at the photodiode varying as the ultrasonic wave impinges on the glass. The output from the photodiode is preamplified, averaged and subsequently stored on a digitising oscilloscope.

To understand the processes in a little more detail, first consider Figure 5.17, showing a diagram of light reflecting at a glass-air interface. For light with its E-vector perpendicular to the plane of incidence, Feynman gives us the equation:[29]

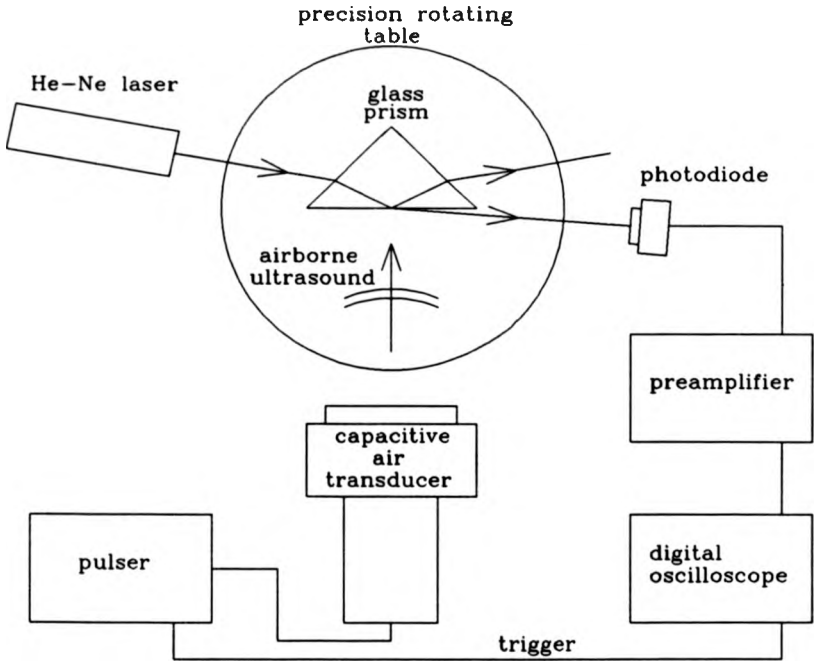

Figure 5.16 Diagram showing the layout of the optical detector.

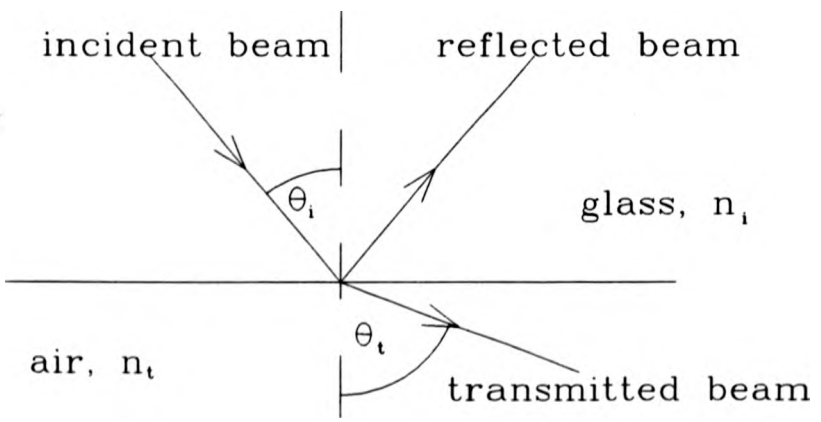

Figure 5.17 Reflection of light at a glass-air interface.

$$R_{\perp}=\frac{\sin^2(\theta_i-\theta_t)}{\sin^2(\theta_i+\theta_t)} \qquad (5.11)$$

where $R_{\perp}$ is the (perpendicular) reflection coefficient. For light with its E-vector parallel to the plane of incidence, the equation:

$$R_{\parallel}=\frac{\tan^2(\theta_i-\theta_t)}{\tan^2(\theta_i+\theta_t)} \qquad (5.12)$$

is also given. The transmission coefficient for these two cases can be evaluated from the above equations and by the equation:

$$T=1-R \qquad (5.13)$$

(Which is a consequence of the law of conservation of energy). Where T is the transmission coefficient. It must be also remembered that the angles, θ_i and θ_t are related by Snell's law;

$$\frac{\sin\theta_i}{\sin\theta_t}=\frac{n_t}{n_i} \qquad (5.14)$$

where n_t and n_i are the refractive indices for the transmitted, and incident beams respectively. Both the reflection (solid line) and transmission (dashed line) coefficients for light at a glass-air interface (using equations 11 to 14), varying θ_i between 0° and 90°, are plotted in Figures 5.18a (E-perpendicular) and 5.18b (E-parallel).

Both graphs show the change in reflectivity/transmittivity with increasing angle, leading to total internal reflection at about 42°. It is interesting to note that Figure 5.18b shows the Brewster effect, where the reflection coefficient is zero,

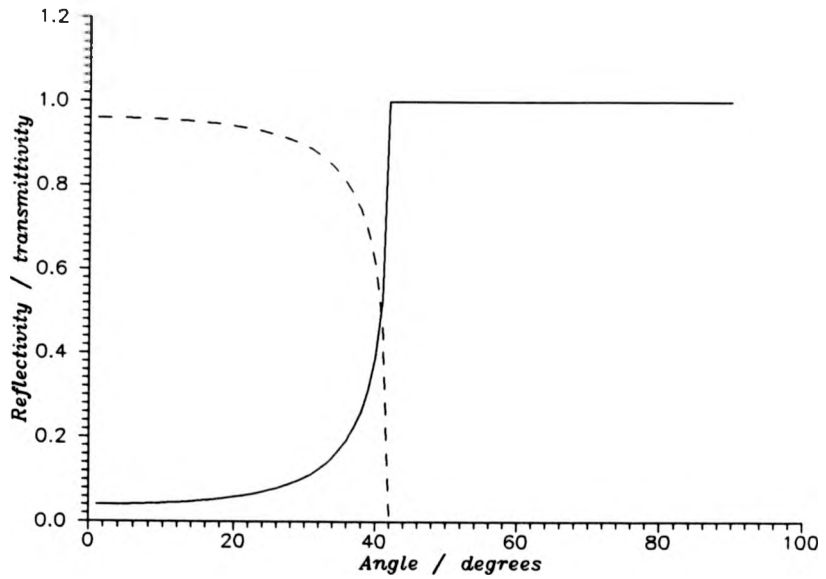

Figure 5.18a Reflection and transmission coefficients for an air-glass interface, E perpendicular to the plane of incidence.

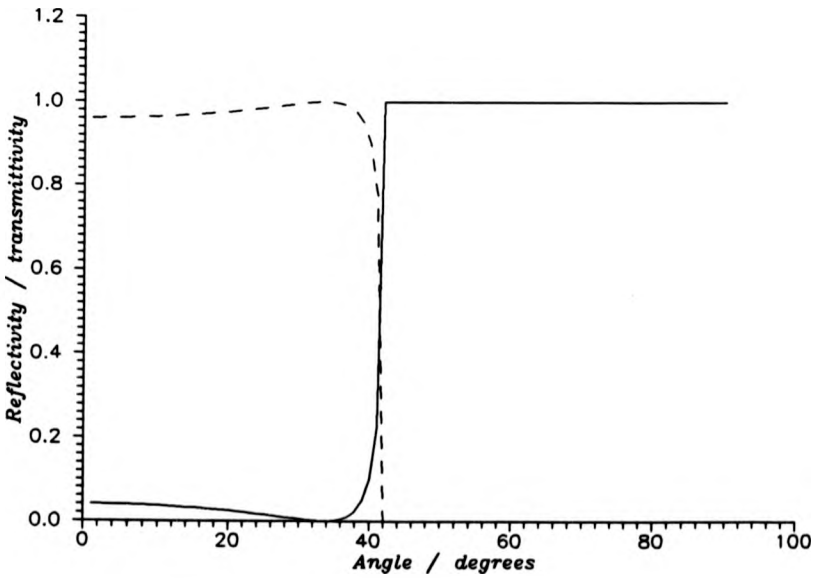

Figure 5.18b Reflection and transmission coefficients for an air-glass interface, E parallel with the plane of incidence.

and the transmission coefficient is 1, at about 34°. Both graphs show the maximum change of transmission coefficient with angle (the maximum gradients of the graphs) at just under the critical angle for total internal reflection. This suggests that operating in this region would give the maximum sensitivity for the optical detector.

To show this, the reflection coefficient of the interface was calculated whilst varying the refractive index of the air (n_t), and was repeated at a number of angles of incidence (θ_i). This is shown for angles of 10° and 41° in Figures 5.19a and 5.19b respectively. These graphs were calculated with the refractive index of the glass being 1.5. The refractive index of the air was varied between 1 and 1.0006 (the refractive index of air at S.T.P. is around 1.0003[30]). Both Figures show a straight line, suggesting that the output from the optical detector will be linear within this region. The important difference between these graphs is the gradient: The gradient with θ_i=10° is around 5% of that with θ_i=41°, suggesting that the detector is 20 times more sensitive at 41° than at 10°.

5.3.3 Results obtained with the new airborne ultrasonic transducers and optical detector

A number of tests were devised to investigate the performance of the new airborne ultrasonic transducers, using conventional capacitance devices as a reference (these actual devices are described in reference 13). The optical detector was used to measure the output from the conventional capacitance transducers.

For all the tests, the ultrasonic transmitter was held close to the receiver,

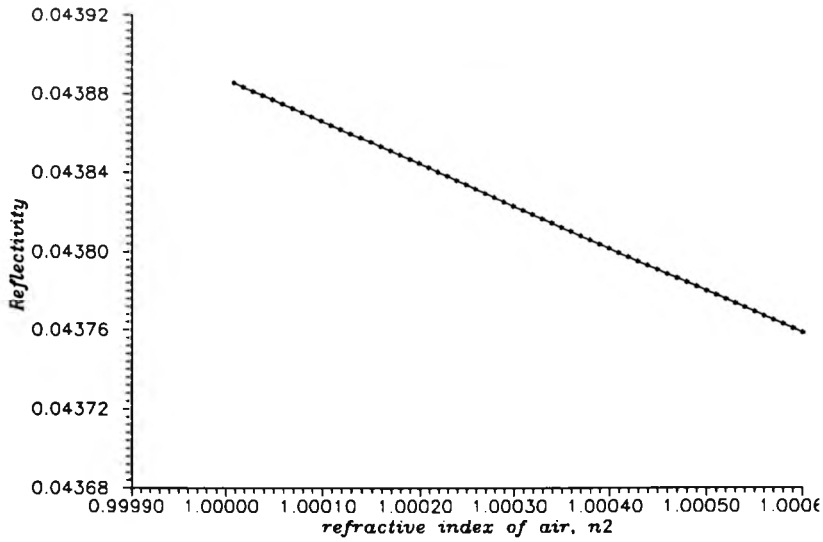

Figure 5.19a Variation of reflectivity with the refractive index of air (air-glass interface with an incident angle of 10°).

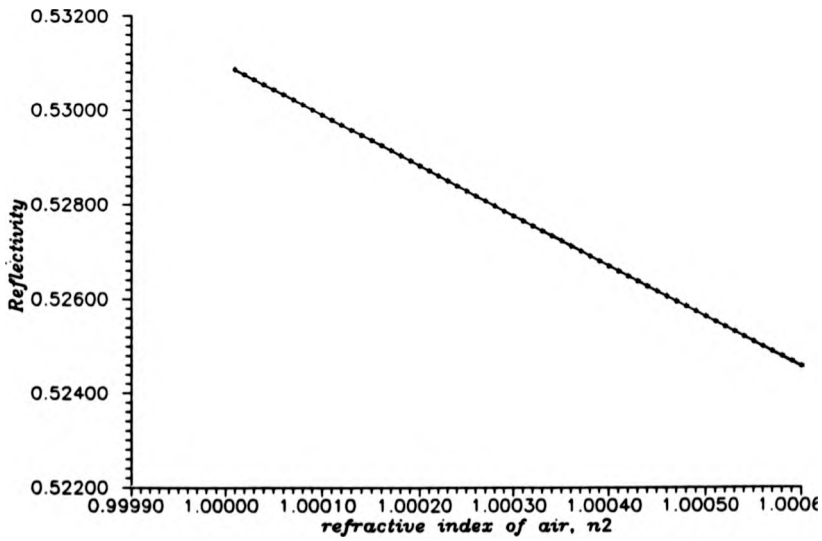

Figure 5.19b Variation of reflectivity with the refractive index of air (air-glass interface with an incident angle of 41°).

and the faces were carefully aligned so as to maximise the amplitude of the signal. It is understood that the tests shown here represent only a very crude picture of the overall performance of the transducers, however this is considered sufficient to establish an idea of the capabilities of these transducers.

For ultrasonic generation, the capacitance transducers were driven by an AVTEK pulser, type AVRH-1-C, with an output Voltage of 350V, a variable pulse duration (which was optimised for the particular transducer), and no D.C. bias. When the capacitance transducers were being used as receivers, they operated with 100V bias and, the signals were amplified with a Cooknell Charge amplifier type CA6 / SU2. The waveforms were recorded on a Tektronix type TDS540 digital oscilloscope, and transferred to a 30-286 IBM microcomputer for analysis.

Figure 5.20a shows the waveform from the conventional capacitance device, as recorded by the optical detector. Two separate pulses are clearly seen, separated by 3μs (the pulse-duration). This waveform was attributed to the ultrasound from the transducer being generated only by the leading and trailing edge of the voltage transient. When the pulse duration was varied, the separation of these peaks were seen to change accordingly. The waveform is seen to be rather noisy, especially when the fact that this has been averaged over 40000 times is considered!; as was explained earlier, this might be attributed to the very slight change in refractive index of the air when insonified. The observation of these "twin peaks" was thought to be a useful contribution to the understanding of the operation of these silicon-backplate capacitance air transducers. The frequency spectrum of this waveform, given in Figure 5.20b, is (as would be

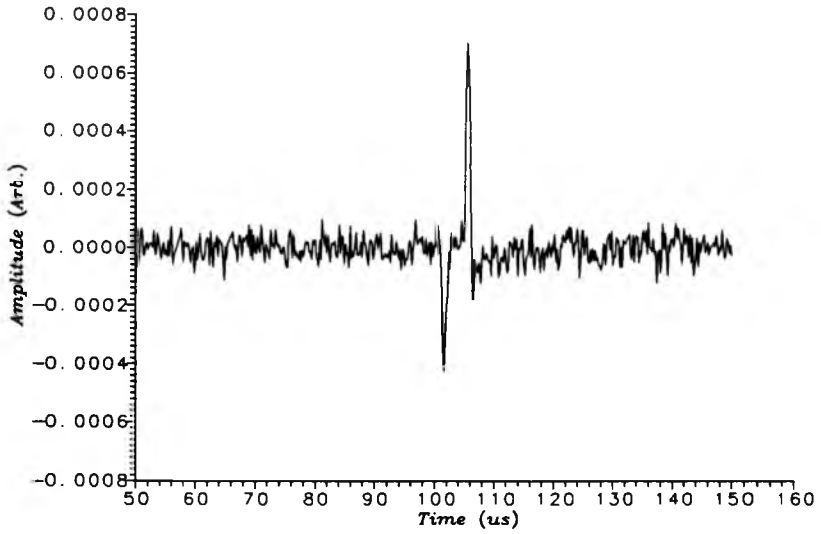

Figure 5.20a Waveform obtained from a silicon-backplate capacitance transducer using the optical detector.

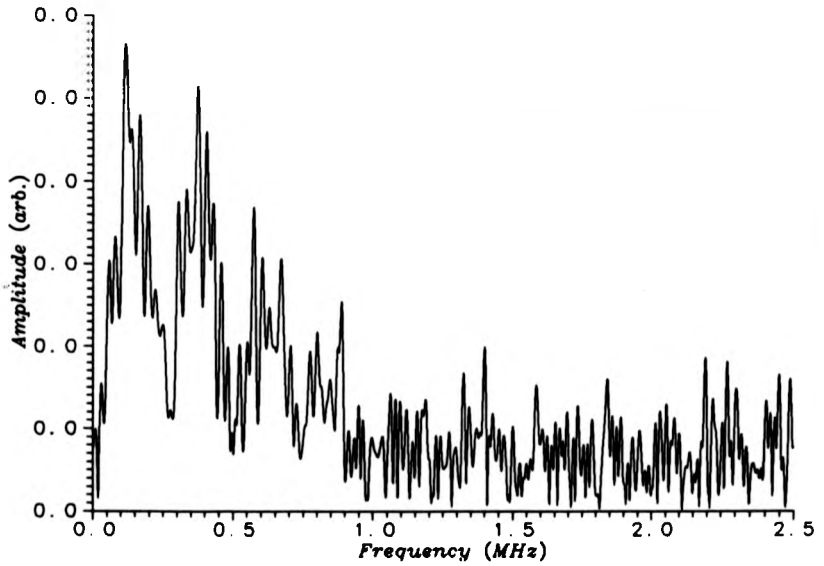

Figure 5.20b Fourier transform taken of the waveform obtained from a silicon-backplate capacitance transducer using the optical detector.

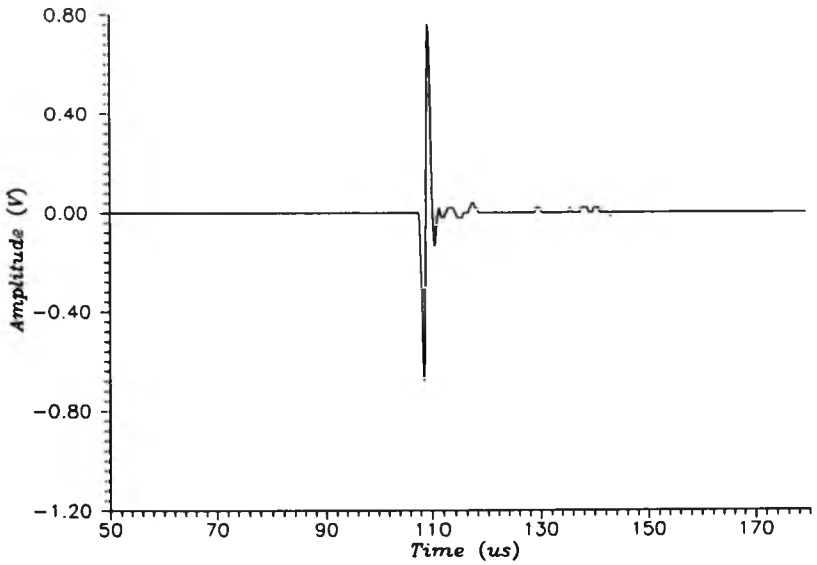

Figure 5.21a Waveform obtained with a pair of silicon-backplate capacitance transducers to generate and receive airborne ultrasound.

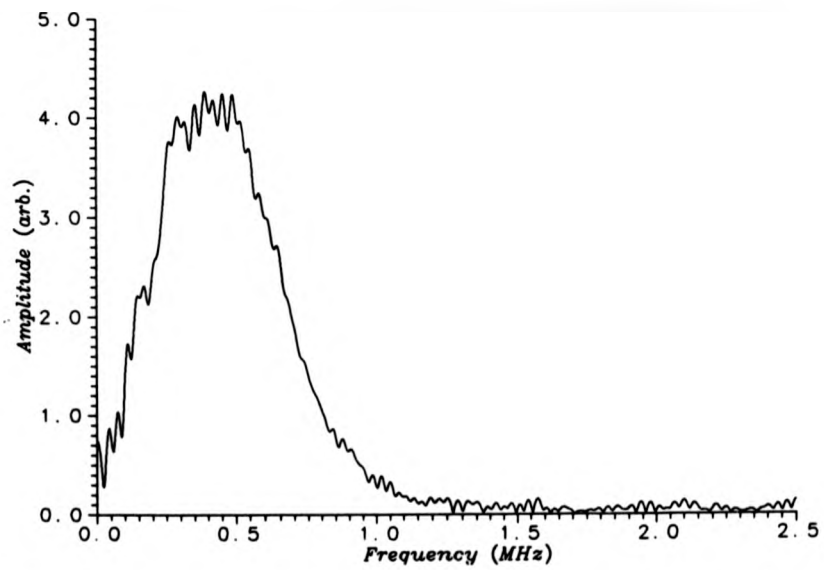

Figure 5.21b Frequency spectrum taken of the waveform obtained with a pair of silicon-backplate capacitance transducers to generate and receive airborne ultrasound.

expected with such a noisy waveform) noisy itself, however it can still be seen that the ultrasound has a useful component up to 1MHz.

Figure 5.21a shows the waveform from a pair of silicon-backplate transducers (which can be taken, in effect as the reference against which the transducers described in this chapter are compared). The drive pulse was 350V, and 0.5μs long. It can be seen that the pulse is very clean, with a large signal amplitude. The corresponding frequency spectrum (Figure 5.21b) shows that this pulse has a useable bandwidth up to around 1MHz.

Figure 5.22a replaces the silicon-backplate transducer that was being used as an ultrasonic generator with the mica transducer. The drive pulse was still 0.5μs, but the amplitude was increased to 1000V. It should be noted that 350V was chosen as the maximum voltage that could safely be applied across the polymer membrane in the silicon-backplate transducers, whereas the mica transducers easily withstood 1000V, which was the maximum output from the pulser. This waveform shows a sharp initial peak with a similar amplitude to that generated by the previous transducer, but with an inferior second (inverted) peak, and considerably more noise. The corresponding frequency spectrum (Figure 5.22b) is inferior to that of Figure 5.21b, but still has a useable bandwidth up to 1MHz.

Figure 5.23a was taken with the silicon-backplate transducer as the ultrasonic source (which was driven with a 3μs, 350V pulse), and the Lorentz polymer-membrane transducer as the receiver. This gave a nice clean pulse (successive pulses were due to multiple reflections within an air space in the transducer), but with a much reduced amplitude, and (as can be seen from the

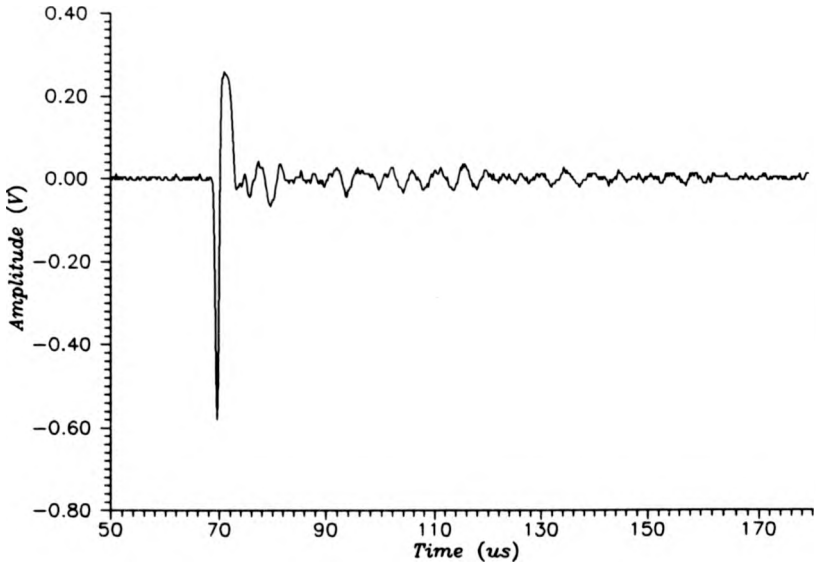

Figure 5.22a Ultrasonic waveform obtained with a mica based transducer as ultrasonic generator, and a silicon-backplate capacitance transducer as a receiver.

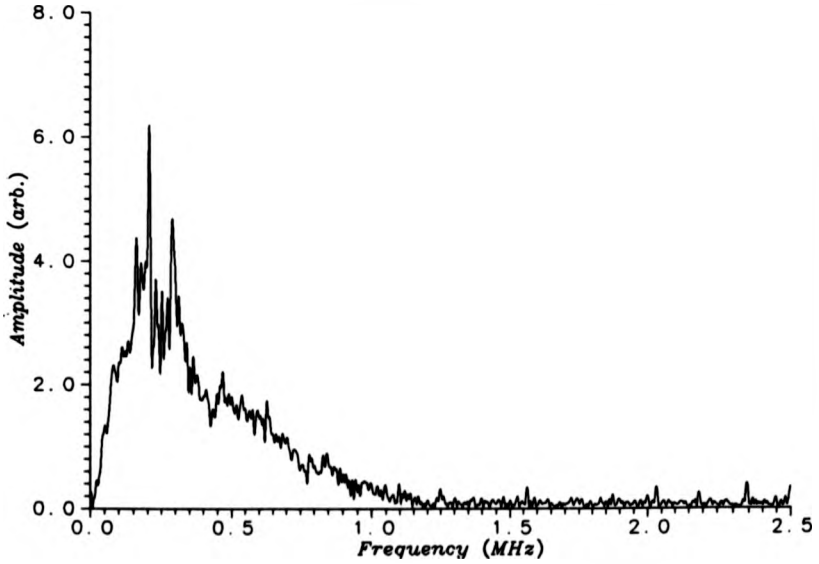

Figure 5.22b Fourier transform taken from the waveform obtained with a mica based transducer as a generator, and a silicon-backplate capacitance transducer as a receiver.

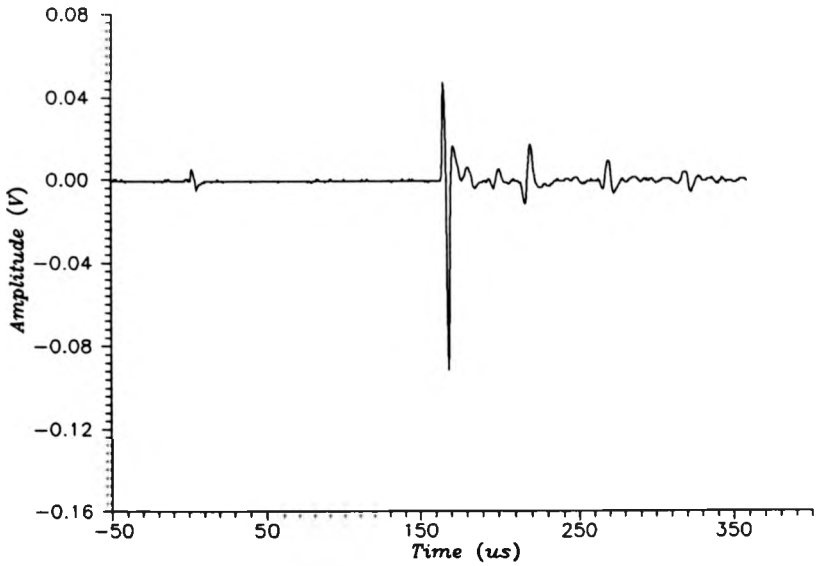

Figure 5.23a Waveform obtained with a silicon-backplate capacitance transducer as a generator, and a Lorentz membrane transducer as a receiver.

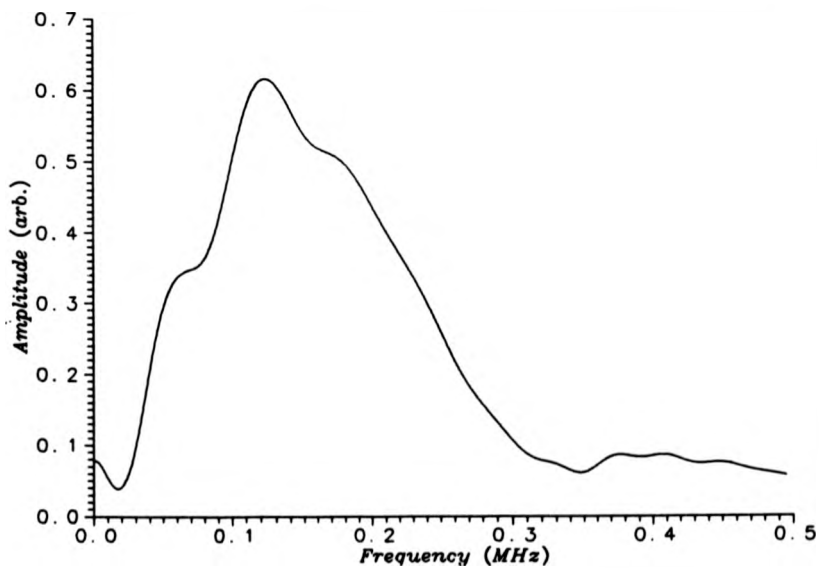

Figure 5.23b Fourier transform taken from the waveform obtained with a silicon-backplate capacitance transducer as a generator, and a Lorentz membrane transducer a receiver.

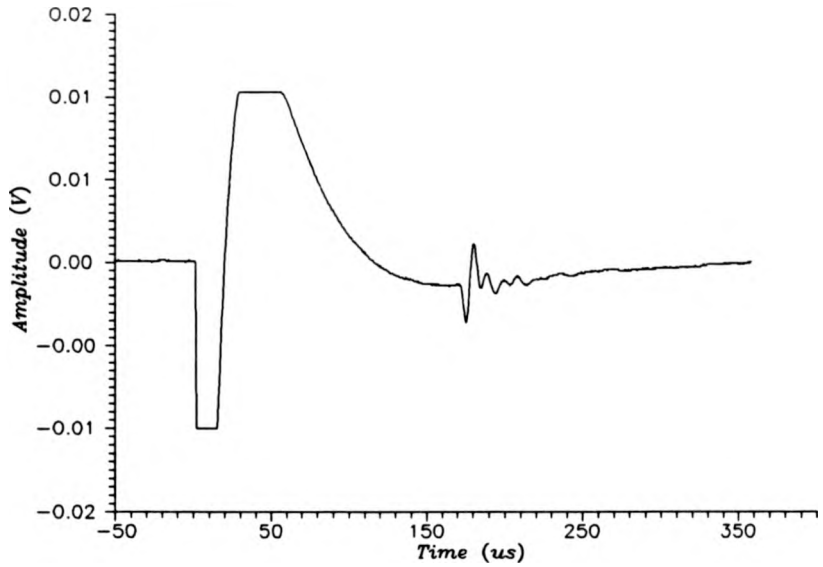

Figure 5.24a Ultrasonic waveform obtained with a Lorentz-foil based transducer as ultrasonic generator, and a silicon-backplate capacitance transducer as a receiver.

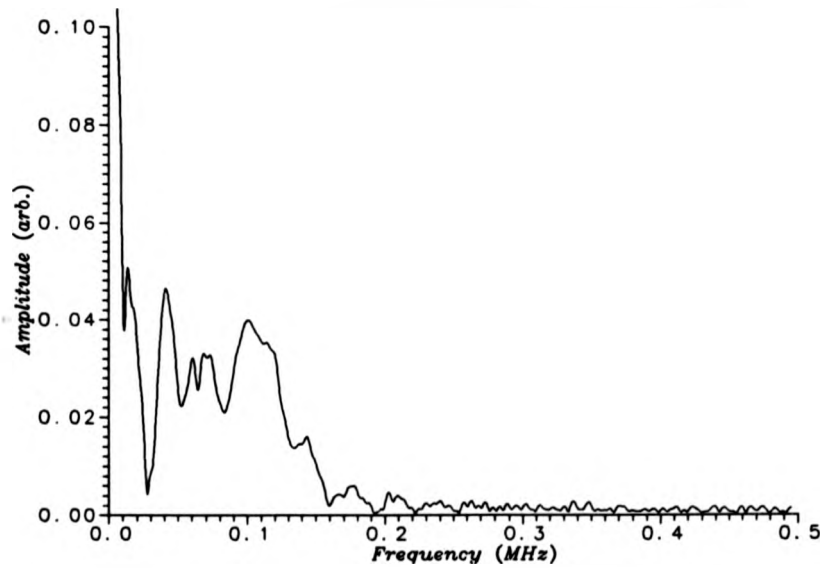

Figure 5.24b Fourier transform taken from the waveform obtained with a Lorentz-foil based transducer as a generator, and a silicon-backplate capacitance transducer as a receiver.

frequency spectrum in Figure 5.23b) a much reduced frequency response (with an upper limit of around 350kHz).

Figure 5.24a shows the waveform generated by the Lorentz foil transducer, and received with the silicon-backplate transducer. Whilst the signal is still useable, it is much reduced in amplitude when compared with the other transducers, and has a lower frequency content (up to 150kHz).

Figure 5.25a shows the waveform generated by the silicon-backplate transducer, and received with the Lorentz foil transducer. As above (Figure 5.24a), the signal is still useable, though it is also of relatively low amplitude, and has a low frequency content (up to 200kHz).

5.3.4 Discussion and future work - The air transducers and the optical detector

The optical detector has been shown to give useful results with air transducers. The detector is thought to work at a very small point, with a large bandwidth, and with a linear response, in fact, if it were not for the very low sensitivity, this could be an ideal transducer. The low sensitivity of these devices in air may be attributed, at least in part, to the low refractive index of air (around 1.0003). The refractive index of water is much higher (around 1.33), and this type of detector should be much more sensitive to detecting ultrasonic waves in immersion. It is therefore hoped that further work will be undertaken to develop this detector in both air, and in immersion, which could be, initially, for high precision transducer characterisation, and could subsequently have applications for acoustic holography work.

The results obtained with the new types of transducer show that they do

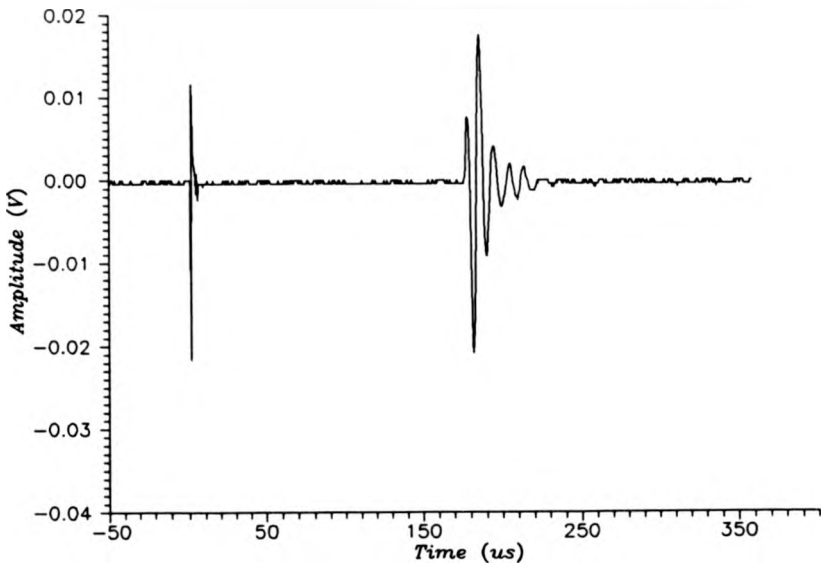

Figure 5.25a Ultrasonic waveform obtained with a silicon-backplate capacitance transducer as an ultrasonic generator, and a Lorentz-foil based transducer as a receiver.

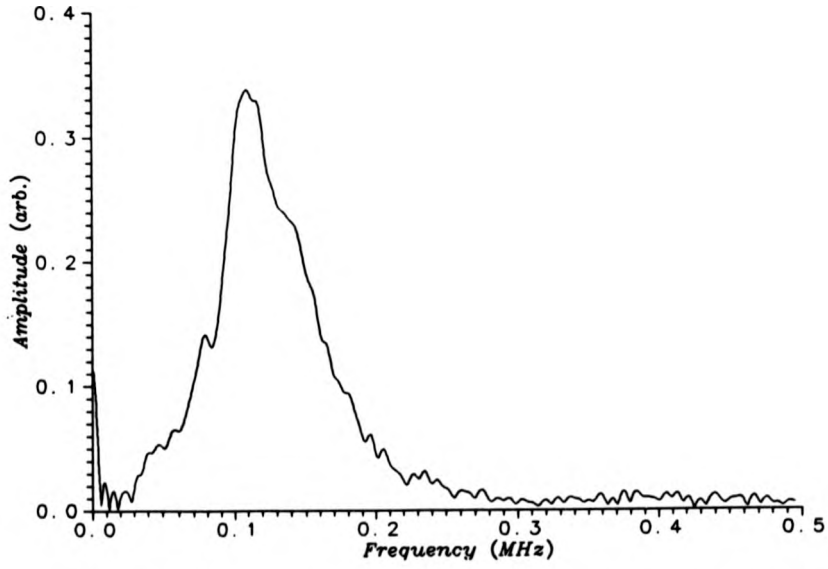

Figure 5.25b Fourier transform taken from the waveform obtained with a silicon-backplate capacitance transducer as a generator, and a Lorentz-foil based transducer as a receiver.

not show an improvement in either sensitivity, or bandwidth when compared with polymer membrane, silicon backplate capacitance transducers. It must however be remembered that the capacitance transducers have been developed now for a number of years, and therefore more research needs to be undertaken on these new transducers (on improving both their sensitivity and their bandwidth) to give a fairer comparison. It must also be kept in mind that the new transducers might have applications in situations where silicon backplate transducers could not be used, for example in hostile environments, or where a passive device is necessary.

For the Mica transducers, the first efforts in improving their performance must be directed towards achieving a better delaminated layer (thinner and more even), and efforts are continuing in using a $C0_2$ laser to achieve this. Further improvements should also be achievable by using thinner mica sheets (increasing the electric field strength). At present, these transducers have not operated as receivers. However it is hoped that they will if the improvements described above can be achieved. It is intended to investigate the use of this type of transducer as a high temperature receiver for hostile environments.

The Lorentz-membrane transducer should be improved by firstly improving the quality, and number of turns on the coil (considerable difficulty was encountered when trying to fabricate this). By combining a better coil with an increase in the magnetic field, (which can be achieved by slight changes to the magnetic circuit design) and improving the amplifier electronics, it is hoped that improvements of orders of magnitude can be made to the sensitivity of this device, it is yet to be seen, however, whether the performance of this transducer will rival that of the polymer membrane, silicon backplate capacitance

transducers. This transducer does have the advantage in that it is completely passive (requiring no bias voltage), and may find applications in potentially explosive environments.

The Lorentz-foil transducers could be improved in similar ways as the Lorentz membrane transducer described above, in that the first improvements will probably involve a re-design of the coil and magnetic circuit, (the magnetic circuit used in these transducers is very crude, being designed for flexibility, rather than to maximise the magnetic field at one magnet separation). Further improvements will also need to be made to both the driving, and preamplification circuitry. This design of transducer should be adaptable for operation at elevated temperatures using the techniques described in chapter 4 of this thesis, and it is proposed to do this in the near future.

5.4 References

1. J.Krautkramer and H.Krautkramer, "Ultrasonic testing of materials", (1969), Springer-Verlag, New York.
2. R.Halmshaw, "Non-destructive testing", (Edward Arnold) (1987).
3. J.D.Achenbach, "Wave propagation in elastic solids", North Holland, (1973).
4. L.E.Kinsler and P.Frey, "Fundamentals of acoustics", 2nd ed, (Wiley, New York), (1962).
5. L.M.Brekhovskikh, "Waves in layered media", 2nd edition (Academic press, N.Y., 1980).
6. W.T.Thompson, "Transmission of elastic waves through a stratified solid

material", J. Appl. phys. 21, 1215-1222 (1950)

7. D.A.Hutchins, L.F.Bresse and D.R.Billson, "Resonance studies of bonded Aluminium joints", Nondest. Test. Eval., Vol. 10, 1993, pp. 149-165

8. G.Canella, "The effect of couplant thickness in ultrasonic contact testing", Brit. J. of NDT, Nov. 1974, pp. 179-182

9. A.Vincent, "Influence of wearplate and coupling layer thickness on ultrasonic velocity measurement" Ultrasonics, Vol.25, July 1987, pp.237-243

10. W.Sachse, N.N.Hsu, "Ultrasonic transducers for materials testing and their characterisation", in Physical Acoustics Vol. XIV (Academic press, N.Y., W.P.Mason and R.N.Thurston, eds., 1979), pp. 277-407

11. M.Silk, "Ultrasonic transducers for nondestructive testing", (Adam Hilger, Bristol, 1984).

12. D.R.Billson and D.A.Hutchins, "Development of novel piezoelectric ultrasonic transducers for couplant-free non-destructive testing" , Brit. J. of NDT, Vol. 35, No. 12, Dec. 1993. pp.705-709

13. W.M.D.Wright, D.W.Schindel, and D.A.Hutchins, "Studies of laser generated ultrasound using a micromachined silicon electrostatic transducer in air", Submitted to J.A.S.A.

14. W.Manthey, N.Kroemer and V.Magori, "Ultrasonic transducers and transducer arrays for applications in air", Meas. sci. techni, 3, (1992), pp. 249-261

15. J.A.Hossack and G.Hayward, "Finite-element analysis of 1-3 composite transducers", IEEE Trans. Ultrason., Ferroelectrics, Freq. Contr. UFFC-38, pp. 618-629 (1991).

16. T.R.Gururaja et al, "Piezoelectric composite materials for ultrasonic transducer applications. Part I: Resonant modes of vibration of PZT rod-polymer composites", IEEE Trans. Son. and Ultrason., Vol. SU-32, No.4, July 1985, pp. 481-498.

17. T.R.Gururaja et al, "Piezoelectric composite materials for ultrasonic transducer applications. Part II: evaluation of ultrasonic medical applications", IEEE Trans. son. and ultrason., Vol. SU-32, No.4, July 1985, pp. 499-513.

18. M.Luukkala and P.Meriläinen, "Metal plate testing using airborne ultrasound", Ultrasonics, Sept. 1973, pp. 218-221.

19. G.Hayward and J.A.Hossack, "Unidirectional modelling of 1-3 composite transducers", J. Acoust. Soc. Am., 88, (2), August 1990, pp.599-608.

20. J.A.Hossack and G.Hayward, "Finite element analysis of 1-3 composite transducers", IEEE Trans. Ultrason., Ferro. freq. contr. **UFFC-38**, (1991), pp. 618-629.

21. D.W.Schindell, D.A.Hutchins, L.Zou, and M.Sayer. "Capacitance devices for the generation of air-borne ultrasonic fields", Proc. 1982 IEEE ultrasonics symp., (1988) pp. 843-846.

22. D.A.Hutchins and J.D.Macphail, "A new design of capacitance transducer for ultrasonic displacement detection", J. Phys. E. 18, (1985) pp. 69-73.

23. D.W.Schindel and D.A.Hutchins, "Capacitance devices for the controlled generation of ultrasonic fields in liquids", Proc. IEEE Ultrason. symp., (1991), pp. 301-304.

24. H.Carr and C.Wykes, "Diagnostic measurements in capacitive transducers",

Ultrasonics, (1993), Vol.31, No.1, pp.13-20.

25. D.W.Schindel, D.A.Hutchins, L.Zou and M.Sayer. "The design and characterisation of micromachined air-coupled capacitance transducers", Submitted to J.A.S.A.

26. W.S.H.Munro and C.Wykes, "Arrays for airborne 100kHz ultrasound", Ultrasonics, (1994), Vol.32, No.1, pp.57-64.

27. W.Kuhl, G.R.Schrodder and F.K.Schröder, "Condenser transmitters and microphones with solid dielectric for airborne ultrasonics", Acustica, Vol.4, No.5, (1954), pp.519-532.

28. K.Suzuki, K.Higuchi and H.Tanigawa, "A silicon electrostatic ultrasonic transducer", IEEE Trans. ultrason., Ferro., freq. contr., Vol. 36, No.6, November 1989, pp.620-627.

29. R.P.Feynman, R.B.Leighton and M.Sands, "The Feynman lectures on Physics", (1964), Addison-Wesley, Volume 2, 32-11.

30. R.M.Tennent, "Science data book", Oliver and Boyd, 1971.

CHAPTER 6

VISUALISATION OF ULTRASOUND USING PHOTOELASTIC AND SCHLIEREN TECHNIQUES

6.1 Introduction

It was thought that a method of visualising ultrasound directly might give a valuable insight into the physics of the phenomena studied in other chapters in this thesis. This chapter presents some new results on the use of visualisation techniques in liquids, gases and solids. Firstly, the fields given by conventional piezoelectric transducers will be visualised to show the capabilities of the techniques. Then the fields generated by a pulsed laser will be investigated, after this, other measurements of the field in air of capacitance transducers will be shown, this is followed by the visualisation of the field given by a couplant free transducer, and lastly by the visualisation of the ultrasonic field around an adhesive bond.

Even the simplest ultrasonic wave is a highly complicated moving stress pattern, propagating rapidly in all three dimensions. As time progresses, this wave is invariably complicated further by many other phenomena including reflections, diffraction, refraction, transmission and mode conversions. Normally, these ultrasonic waves are detected by ultrasonic transducers, and the path of the ultrasound through the test medium implied from the resultant waveform. The waveform given by the detector usually represents only one component of the stress from the ultrasonic field, this is averaged over the active area of the transducer, and is further distorted by the non-ideal response of the transducer and the electronic circuitry. Therefore, when a transducer is used to detect an ultrasonic wave at the surface of the object, the estimated path of the ultrasound through the medium cannot always be assumed to be wholly correct.

Standard theory exists to predict the path of this propagating ultrasound,

but is generally difficult to apply for anything but the simplest situations (for example, an infinite plane wave impinging on a plane boundary). For real situations, it can be rather difficult to predict an accurate model of the field. Propagating ultrasonic wavefronts have been modelled using computer intensive techniques based on the finite difference method, but these are slow, laborious and expensive. For these reasons, methods of optical visualisation have been described in the literature. Such methods as direct visualisation can be fast, and can give an accurate two dimensional picture of the field (the sample can be rotated to give three-dimensional information, and in fact, three dimensional analysis of the ultrasonic field has been undertaken by other authors in the field[1,2]) at any time after the generation of the ultrasound. There are, in fact, many optical approaches to field visualisation, but those that have received most interest and which have been used in the present work are schlieren techniques and photoelasticity.

The schlieren technique has been used for the investigation of materials with varying refractive indices for many years, With Hooke's works of 1665 and 1672 being regarded as the first in this field[3,4]. The first visualisation of ultrasound was probably done by Wood in 1900[5], who used a spark source to generate sound waves in air (and used a second spark source to image these). Brillouin suggested that the diffraction of light by ultrasound was possible in 1922[6], and in 1932, Debye and Sears published a paper at the same time as Lucas and Biquard, showing that the diffraction of light by ultrasound had been observed[7,8]. The next advance in the field was reported in papers by Raman and Nath in 1935 and 1936[9,10], these papers solved much of the mathematics associated with the

diffraction of light by ultrasound. Much of the more recent work in the field of ultrasonic visualisation has been carried out in Britain, with the main authors including V.M.Baborovski and D.M.Marsh (T.I.)[11,12,13], K.G.Hall (B.R.)[14,15] and D.R.Andrews[16,17] (Cambridge and Kings college, London), who pioneered the use of LED's for light sources. A number of papers have been published which describe the theory of schlieren and photoelastic systems in great detail[18], and these are supplemented by papers which describe applications of these techniques[19,20,21,22]. A paper of note, relevant to the work described in this chapter, is by Emmony[23], who analyzed CO_2 generated pulses in water using the schlieren method.

6.2 Ultrasonic visualisation methods

The photoelastic and schlieren visualisation methods are well known in the literature, for clarity however, brief descriptions are presented below of their method of operation.

6.2.1 The Photoelastic Technique

Consider light propagating (from left to right) as in Figure 6.1. Unpolarised light passes from the left through a plane polariser (a sheet of polaroid film) and produces linearly polarised light at A. If the sample (made from an optically transparent, isotropic material, such as glass) is stressed by an ultrasonic wave, then this can cause it to become optically birefringent. Plane polarised light that passes through this birefringent part of the sample will, in general, be split into ordinary and extra-ordinary components. As the ordinary and extra-ordinary optic

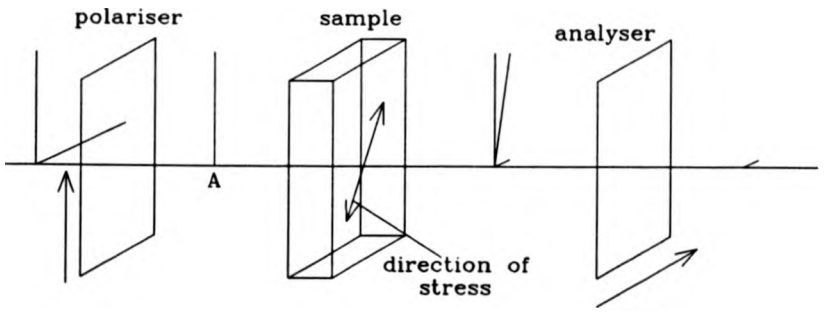

Figure 6.1 The physics of visualising ultrasound using a photoelastic system.

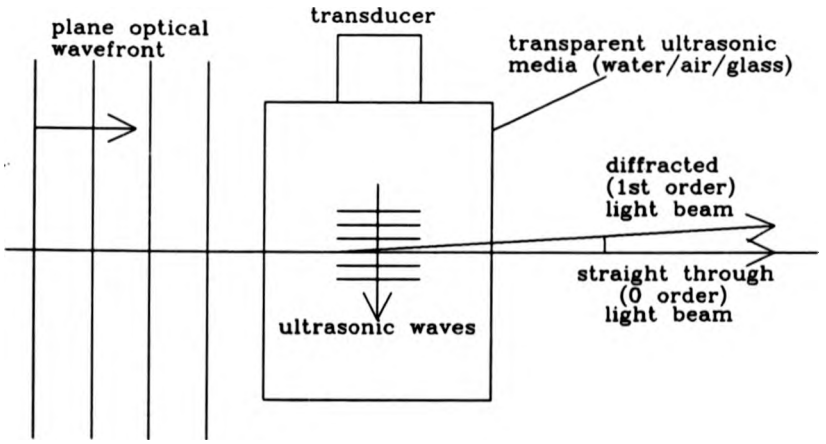

Figure 6.2 Deflection of the plane optical wavefront by an ultrasonic field.

axes have different refractive indices, the two components will not be in phase when they leave the sample; they will re-combine to produce elliptically polarised light, which will now have a component that can pass through the analyzer. This can then be imaged to the right of the analyzer, using suitable lenses. Continuous illumination gives a time averaged image of the ultrasonic field, however, if a stroboscopic light source is used, and the time delay between the light source and the ultrasonic source is varied, then the movement of the ultrasonic waves can be followed.

Because the apparatus has maximum sensitivity to stresses at 45° to the light polarisation direction (and is insensitive to stresses either parallel or perpendicular to the light), two images are usually taken, with the polaroids rotated 45° for the second image. It has been reported that the use of a pair of circular polarisers using quarter wave plates, allows stresses in any direction to be seen. This works by aligning a quarter wave plate to convert the plane polarised light at A into circularly polarised light. After then passing through the sample, a second quarter wave plate, of opposite handedness to the first, is aligned to convert this circularly polarised light back into plane polarised light, finally, it is then extinguished by the second polariser (the analyzer). Stresses in the sample, in any direction, would change the circularly polarised light into elliptically polarised light, which would not be turned into plane polarised light to be extinguished by the analyzer. It was found that the use of this more complicated setup (which would have made alignment difficult) was not necessary for the experiments undertaken here, and the advantages of viewing stresses in all directions did not warrant the extra effort needed.

6.2.2 The Schlieren Method

The basic phenomena underlying the schlieren method for ultrasonic visualisation are illustrated in Figures 6.2 and 6.3. In Figure 6.2, a plane optical wavefront is travelling from left to right. An ultrasonic wave propagating through an optically transparent media will cause a variation in its refractive index. This will slightly deflect the path of the light beam passing through it. As shown in Figure 6.3, the optical wavefront is now focused down to a point where a knife edge is placed. The light that has been deflected by the ultrasound misses the knife edge and is subsequently imaged by an imaging lens. As this light has originated from a deflection by the ultrasonic wave, it will form an image representing the ultrasonic field. As with the photoelastic system, varying the time delay between the light source and the laser enables the progression of the ultrasonic waves to be observed.

6.3 The light source and camera

6.3.1 The light source

Much effort was taken to find suitable light sources for the visualisation systems, which had to fulfil the following criteria:

a) For visualising ultrasound of 5MHz or less, the duration of the light source had to be less than 100nS per pulse. Failure to do this would prevent individual ultrasonic wavefronts from being distinguished (a 5MHz ultrasonic wave will travel half a wavelength in 100nS, and the bright lines corresponding to, say, the compressions, will merge into each other if a light source with a length greater than 100ns is used).

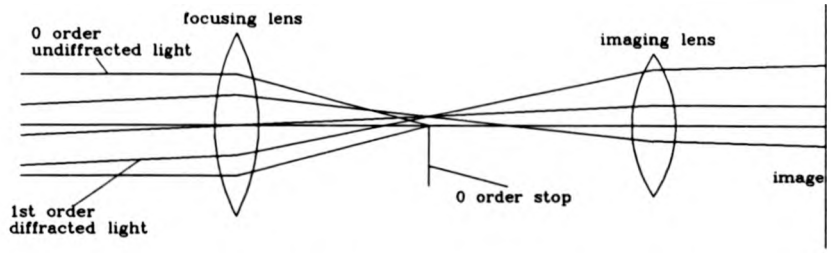

Figure 6.3 Imaging the deflected light in the schlieren system.

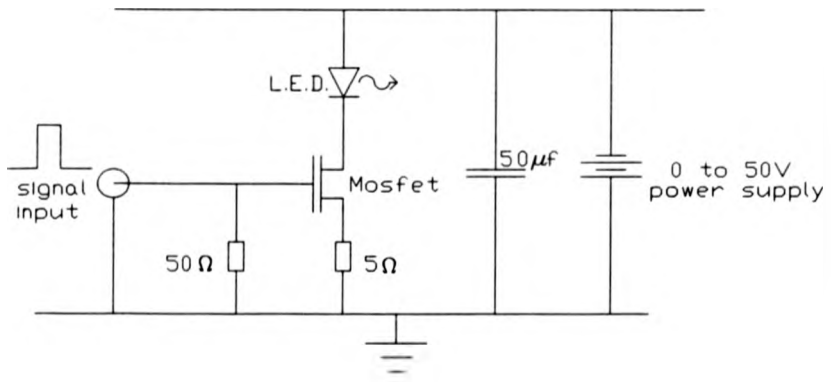

Figure 6.4 Diagram of the circuit used to drive the light-emitting diode.

b) The light from the source must be bright enough to be seen with both the eye and a video camera after passing through either of the two systems.

c) It must be possible to trigger the light pulse with a variable delay so that the progression of the ultrasonic field can be followed.

d) The jitter on firing the light source must be less than +/- 50nS to avoid smearing of the individual ultrasonic wavefronts.

e) The light source for the schlieren system needs to be as small as possible (0.75mm or less) to get the maximum practical sensitivity of the system. The mirrors of the system focus the light source to a 'point'. At this point the knife edge (stop) is placed to just obstruct the light focused to this 'point' (see section 6.2.2). The minimum theoretical size of this 'point' depends on the size of the source, and the smaller this 'point' is, then the less the light has to be diffracted / refracted away from the normal in order to pass the knife edge, and thus the system becomes more sensitive. With a source size of less than 0.75mm, the size of this spot tends to be limited by other factors, such as the quality of the mirrors, the quality of the sample, and the movement of air through the system.

f) The light source should not be excessively expensive

g) The repetition rate of the light source should, ideally, range from individual pulses (to investigate laser generated ultrasound) to 2kHz (a typical repetition rate for commercial piezoelectric ultrasonic pulsers)

h) The light source should ideally, operate in the visible part of the electromagnetic spectrum. Using visible light firstly makes the alignment of the two systems much easier, and secondly makes photography much easier (infra-red films are available, but are much more difficult to work with).

The following possible sources were investigated:

i) a flashlamp system

ii) a pulsed laser

iii) a continuous wave (c.w.) laser, passed through an acousto-optic modulator

iv) a light emitting diode (L.E.D.) emitting in the visible part of the electromagnetic spectrum

v) a light emitting diode (L.E.D.) emitting in the near infra red part of the electromagnetic spectrum

vi) a laser diode

i) Flashlamps: The use of flashlamps for ultrasonic visualisation has been well documented in the literature[11,14,15,24,25,26]. Flashlamps can give very intense flashes of light from relatively small sources (1.5mm)[27], with a spectral distribution ranging from the U.V. to the I.R. The main drawback of choosing a flashlamp system is its cost, however such a system is being considered for future work.

ii) Pulsed laser: The use of a pulsed laser was investigated, as these have been reported in the literature[28,29]. This method can produce a very bright (tens of Megawatts with a 100mJ pulse), very short (4nS) light pulse, with a very small source size (of a few μm). The beam would also be very easy to manipulate. The only two theoretical limitations in the ability of a laser to produce an excellent light source are that firstly, because of the highly coherent nature of laser light, any images would have problems with speckle. Secondly, (unless a copper vapour, or a gold vapour laser could be used) the repetition rate would only be 10Hz or less. In practice, however, the cost of a pulsed laser would be tens of thousands

of pounds, and this expense was not warranted when another light source was found that was adequate.

iii) The possibility of using a 2 Watt argon ion c.w. laser with an acousto-optic modulator (a.o.m.) was looked into. This was found to be not suitable for two reasons; firstly, acousto-optic modulators were not readily available that could take 2W of power and still switch fast enough to give light pulses of 100nS or less, and secondly, the power output of such a device was considered inadequate to use as a light source. With a 10% efficient a.o.m., giving 100nS light pulses, at 2kHz, the light output from a 2W laser would average only 0.04mW. Also, as with the case of a pulsed laser, the cost of the argon ion laser, together with an a.o.m. and driving electronics was prohibitive.

iv) A 660nm (visible) light emitting diode was investigated, and was eventually chosen as the main light source for both the schlieren and the photoelastic systems. L.E.D.'s have been successfully used in a number of visualisation systems[16,30,31], and with the recent development of double heterojunction GaAlAs L.E.D.'s, they fulfil all of the criterion listed above (a-h), although a larger light output would still be desirable.

Many of the earlier experiments were undertaken with a Stanley high-super bright L.E.D. (H2000L). This was rated to give a 2cd output when driven continuously, and was found to give out light pulses that were adequate for both of the systems. One problem with these L.E.D.'s was that their output degraded with use, and so needed regular replacement.

Some work was undertaken to try and increase both the lifetime and the light output of the L.E.D. by cooling it with a Peltier-effect element, however

problems were encountered with condensation on the output window of the device. To overcome these problems, a complex vacuum system would have had to have been built. This would not have warranted the time, expense, and effort to improve the durability and light output, (which experimentation proved to be small, even down at liquid nitrogen temperatures). The problem of limited lifetime seems to have been reduced, at least in part, by both the improved reliability of newer batches of super-bright L.E.D.'s, and by a change in the electronics used to drive the L.E.D.

v) An LED in the near infra-red (880nm) was successfully used with a video camera in the schlieren system. This source was seen to be more intense than its visible analogue for two reasons, Firstly that infra red LED's are inherently more efficient devices than visible LED's, giving a greater power output. Secondly, the semiconductor band gap energy levels in the charge coupled device (CCD) in the video camera are energetically closer to near infra red wavelengths than visible wavelengths, making the video camera more sensitive. Despite their success in this application, These light sources couldn't be used for photography as no suitable film was available, and could not be used for in photoelastic rig as no suitable polarising film was available that could work at 880nm.

vi) Attempts were made to use a laser diode as a light source as it was thought to have a number of benefits[32]. Pulsed laser diodes are known to have very bright light outputs, they have easily collimated beams (there is a large selection of custom optics available specifically for collimating laser diodes), they are relatively cheap (of the order of £100 each), and are available at wavelengths in the visible part of the spectrum. Laser diodes are relatively easy to drive (the only

problem with them is that they are rapidly degraded by voltage transients), and the time delay can be simply controlled. Unfortunately, the Laser diode bought for the experiments was found to degrade very quickly, and as a suitable light source (an L.E.D.) was already working, it was thought that the purchase of a number of £100 laser diodes was not warranted.

6.3.2 Light source driving system

At the start of the project, the L.E.D. was driven by the simple circuit shown in Figure 6.4. In this, the signal input turns on the MOSFET (type VN66AFD), which allows current to flow through the L.E.D., The length of this current pulse (and therefore the duration of the light output) was determined by the length of the input signal, provided by a signal pulse generator/delay unit (Farnell type PG5222). The MOSFET had to be driven with a larger than normal voltage input signal (10V) because of the large gate-drain capacitance inherent with these devices. The duration of the light pulse is determined by a combination of the length of the input pulse, and by the capacitance / resistance characteristics of the L.E.D. It was found that the circuit in Figure 6.4 gave an optical pulse duration short enough for the experiments undertaken here, but it is thought that in order to obtain shorter pulses, it should be possible to change the circuit by putting in a resistance of a few ohms in parallel with the L.E.D., thus reducing the effective resistance of the device. This would reduce the time that the diode-capacitance took to discharge, and would therefore reduce the length of the light pulse. Unfortunately, this would also reduce the light output. The amplitude of the current pulse was determined by the drive voltage, which was found to have an

optimum value of 30V. During the course of the project, a commercially made laser diode pulser became available. This was used in preference to the above circuit, as, even though it could not vary the pulse duration (which would increase the light output when looking at lower frequency ultrasound), it was found not to degrade the L.E.D.'s as fast as the circuit described above.

A Photodiode circuit, used to look at the light from the L.E.D. is shown in Figure 6.5. The light pulse, as measured with this photodiode circuit, is shown in Figure 6.6.

6.3.3 Camera System

The images from the two systems were stored in the form of either a photograph, or a video image.

The photographs were taken with a Miranda MS-2 super S.L.R. camera, using Kodak pan technical film. This is a black and white panchromatic negative film which has micro-fine grain and extremely high resolving power. Kodak technical pan film has extended red sensitivity, with a reasonably uniform spectral sensitivity at all wavelengths out to 690nm. (The L.E.D. used in the visualisation systems emits light at 660nm; normal film could not be used as it is relatively insensitive at this wavelength). Photographs were normally used to take a permanent record of the ultrasonic images as they had a much greater resolution than could be achieved with the video camera. There were also a number of experiments (for example with low repetition rate ultrasonic sources) where the photographic camera had to be used, as the video camera wasn't capable of capturing any images.

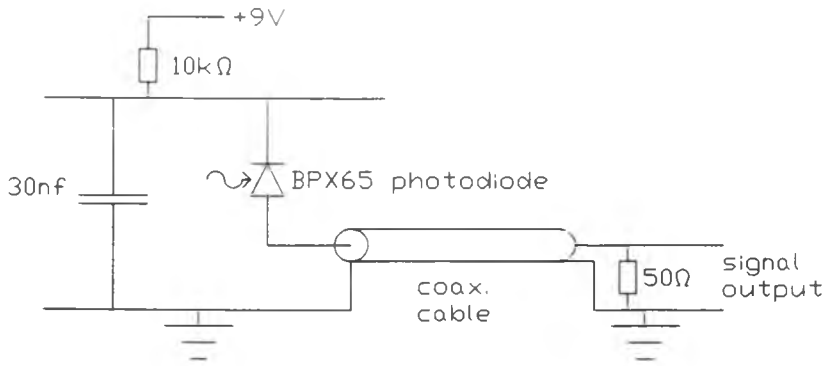

Figure 6.5 Diagram of the photodiode circuit used to investigate the LED output.

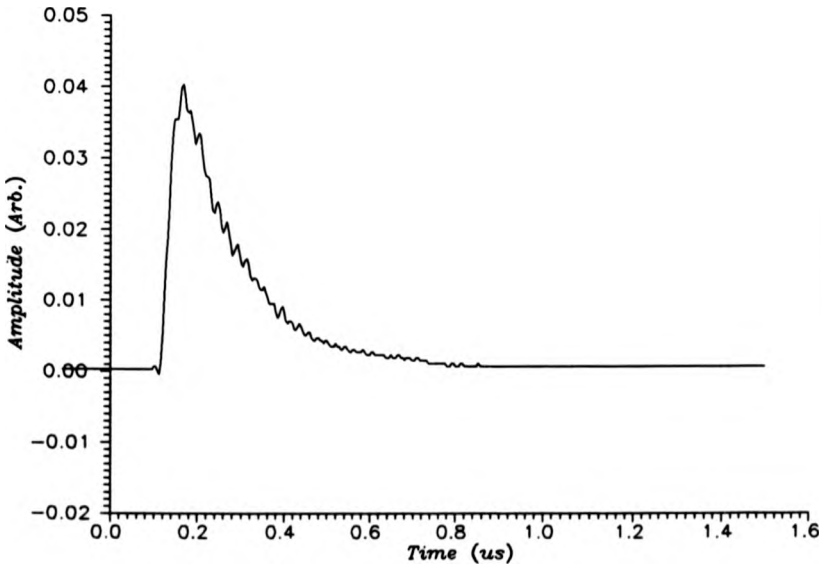

Figure 6.6 LED light output, as measured by the circuit in Figure 6.5.

The Video camera used was a monochrome Ikegami ICD42EAC which had a resolution of 520 T.V. lines, and a light sensitivity of 0.1 lux. For most applications, the video camera was simply connected to a monitor, however when a permanent record of the images was required, the output from the camera could either be connected to a video recorder, or to a frame grabber in a computer. The video recorder used was a simple VHS unit (although a better record could have been taken with a SVHS machine) and had the advantage that the moving ultrasonic field could be followed as it propagated through the sample. The frame grabber used was a Matrox IP8 card, plugged in to the back of a 386 computer. This could be used to store single images, and had the capability of performing image processing on the acquired data. The card was used in conjunction with suitable image processing software, which was supplied with the card. Problems were encountered when trying to obtain hard copies of the video images, as much of their resolution was lost when using a laser printer. This was because conventional laser printers cannot print out a an image in true grey-scale; instead, they use a software algorithm to convert the grey-scale of the video images into a complex pattern of black dots, which tries to give the effect of a grey scale. Part way through the project, limited access was made available to a thermal video printer which was used to give high quality printed pictures with a true grey scale, one of which is included in the results section of this chapter.

6.4 Photoelastic system

6.4.1 The configuration

This is shown in Figure 6.7. The light source consists of a Stanley hi-super-bright 660nm LED, with a plane faced, clear epoxy case. The light from this is collected and focused with a short focal length lens, originally designed for compact-disk (C.D.) players. Because of the extreme accuracy needed when aligning this part of the system, the C.D. lens was mounted on a three axis manipulator, with the distance between the lens and the L.E.D. (along the X-axis) being very finely controlled using a precision micrometer adjuster. The L.E.D. was mounted rigidly on an optical mount.

The two large glass lenses (15cm diameter, 60cm focal length) were used to collimate, and then re-focus the light coming from the C.D. lens. It is to be noted that a number of authors have reported using large Fresnel lenses in their photoelastic systems as they can easily be made big enough to allow a larger field of view than can be obtained with glass lenses[11], however, the field of view obtained with the glass lenses was considered adequate for the experiments undertaken. (The thin, flat, moulded plastic structure of a Fresnel lens can be made much larger than can glass lenses).

The polariser and analyzer were made from a pair of 16cm×16cm sheets of either HN22, or HN32 polarising film (made by the Polaroid Corporation). The HN22 gave a high contrast between the visualised ultrasound and the background, but low light transmittance (22% for randomly polarised light through a single sheet), whereas the HN32 gave medium contrast, and higher transmittance (32% for randomly polarised light through a single sheet). The polariser/analyzer were

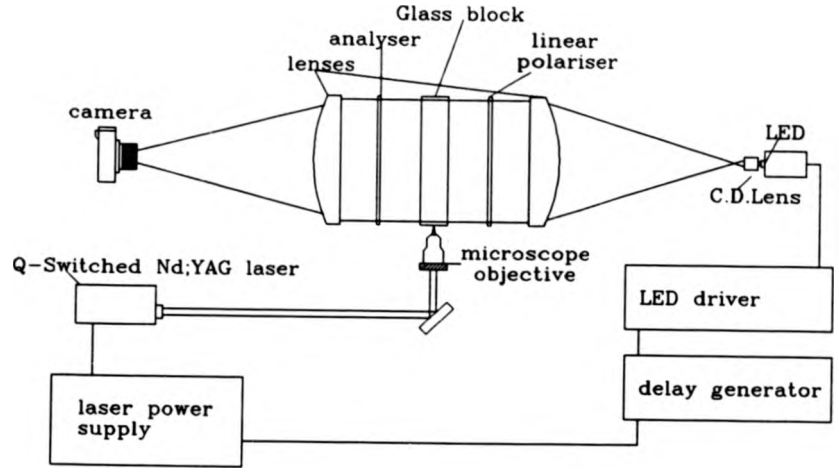

Figure 6.7 Experimental configuration for the visualisation of laser generated ultrasound in glass using the photoelastic method.

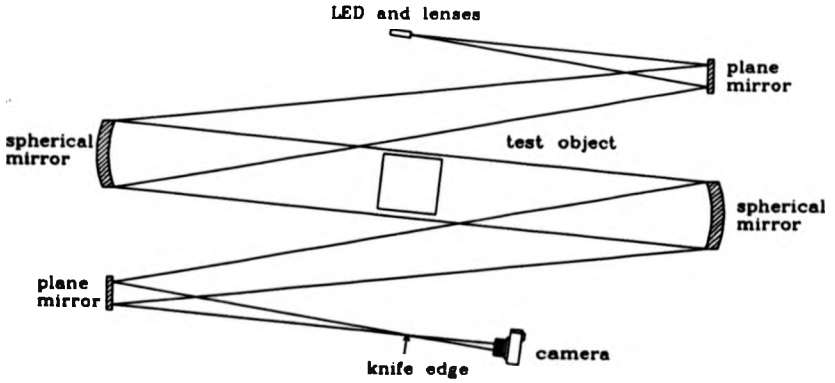

Figure 6.8 Experimental configuration for the visualisation of ultrasound using the schlieren method.

placed inside the two large lenses, as the stresses within the glass of the lenses are much greater than the stresses in the block caused by the ultrasound, and would therefore mask the image of the ultrasound if they were inside the polarisers. The polarisers were mounted in specially designed rotatable mounts.

The imaging end of the system consisted of either the video camera, the photographic camera, or the human eye. The cameras were fitted with zoom lenses to allow the field of view to be varied. Because of the design of the optical system, it was found to be necessary to place a 400mm focal length, 60mm ∅ converging lens between the zoom lens and the second large lens.

The complete optical system was assembled on a triangular optical mount system, and was enclosed in a light tight box. Access to the system was available through apertures in the box covered by light-proof rubber sheets.

6.4.2 The Visualisation medium

Glass was chosen as the medium in which to visualise ultrasound as it is transparent, machinable, and has ultrasonic velocities comparable to those of steel and aluminium. Originally, samples were made from 1" thick float glass which were machined along their edges to give a flat surface (to enable the transducers to make a good contact), but were otherwise untreated. One problem with these samples was that the stresses found around the edges of the blocks (caused by either machining or breaking the glass) tended to mask the ultrasonic stress field close to the surface of the block. This unfortunately made the visualisation of ultrasound close to the transducer particularly difficult. Attempts were made, in collaboration with Pilkington Glass, to try to relieve these stresses thermally, but

with no success (the stresses from the 'stress relieved glass' were found to be much greater than in the virgin glass). Towards the end of the project, a pair of specimens were produced, made from Schott BK7 glass. This glass was cut from a large block which was produced to be essentially stress-free. The cutting procedure was strictly controlled so as to minimise stresses. Subsequently, one of the specimens had holes carefully drilled in it with a diamond coated bit to represent defects. The two samples were then polished on their largest faces. These samples were found to have substantially less stress in them than had the original plate samples, and gave much improved images. This was particularly evident close to the edges of the blocks. Care had to be taken when handling these blocks as a localised temperature increase was induced by momentarily touching the glass, this created thermal stresses which masked the ultrasound.

6.4.3 Experiments and results- photoelastic system

The photoelastic system was used to look at a number of ultrasonic sources, these were;

1) The ultrasound from conventional piezoelectric transducers

2) Laser generated ultrasound

3) Ultrasound from a couplant-free transducer

4) Ultrasound propagating through an adhesive bond

1) Conventional piezoelectric transducers were investigated first as they are easy to drive with high repetition rates, and give an ultrasonic output with large amplitudes, and are therefore easy to visualise. They also give ultrasonic fields that

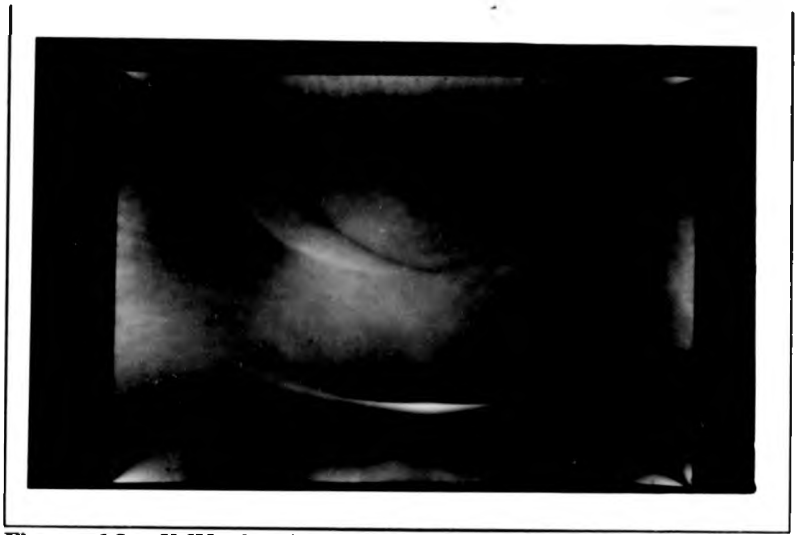

Figure 6.9a 5MHz longitudinal wave transducer with 10μS delay, (photoelastic system).

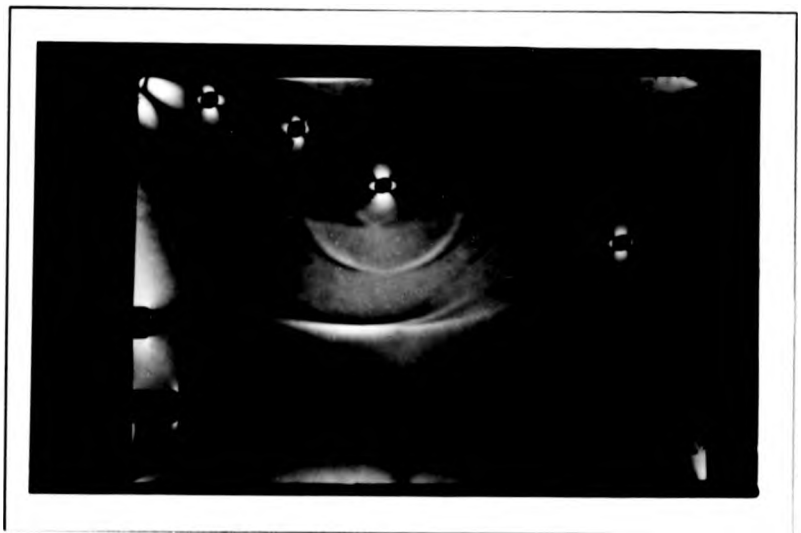

Figure 6.9b Interaction between a 5MHz longitudinal wave transducer and a defect, 7.54μS delay, (photoelastic system).

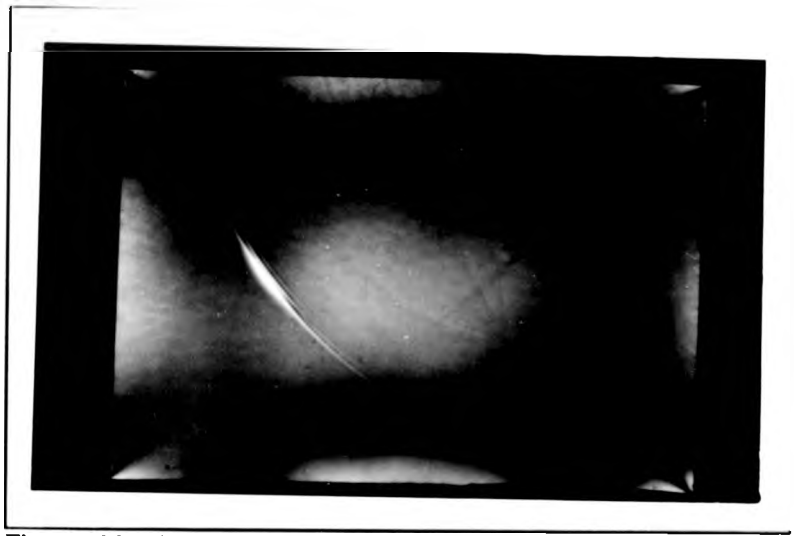

Figure 6.9c 4MHz, 45° shearwave transducer with a 20μS delay, (photoelastic system).

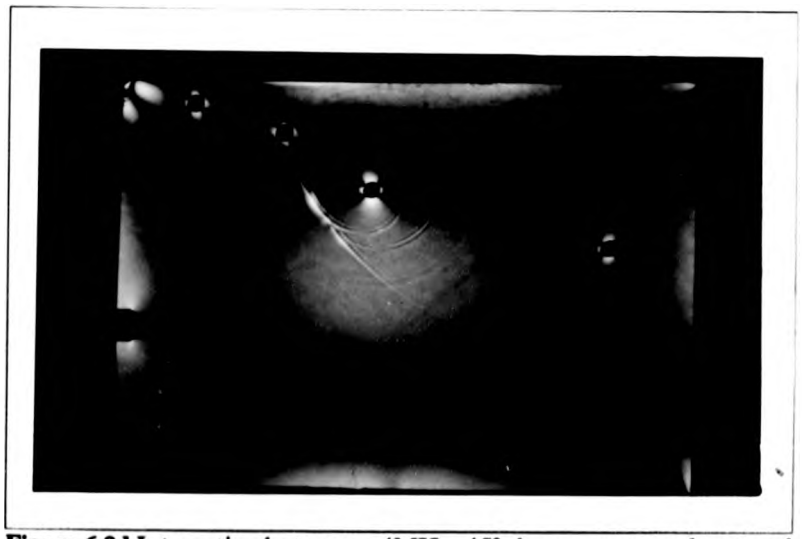

Figure 6.9d Interaction between a 4MHz, 45° shearwave transducer and a defect, 14μS delay, (photoelastic system).

the longitudinal wave that has now passed the hole, a shear wave produced by mode conversion at the hole (which can clearly be seen in the form of a circle centred around the hole). and finally, the longitudinal wave that has been reflected by the hole, and has subsequently been reflected at the top of the glass block. This picture shows how complicated the wave pattern can be in a supposedly simple situation.

Figure 6.9c is taken with a 4MHz, 45° shearwave transducer, with a delay of 20μS. This probe was known to be much more resonant than the longitudinal probes described above, and this is clearly seen in the form of multiple wavelets within the pulse. The wave polarisation is SV, allowing the polaroids to be aligned as for the longitudinal transducers.

Figure 6.9d shows the interaction of the ultrasound from this transducer with the same defect as in Figure 6.9b. This has a delay of 14μS, and three main waves, separate from the original pulse can clearly be seen. These centre on the hole, with the outer wave being a longitudinal wave, the middle wave being a shear wave. The inner wave is caused by the original shearwave producing a surface wave at the glass-air interface at the defect. This propagates around the circular hole, continuously mode converting into a shear wave, and it is this shear wave that is being seen.

2) It was thought that pictures of laser generated ultrasound might help to better the understanding of this phenomenon[34], and that they could help with the analysis of laser generated waveforms that are presented in chapters 4 and 5 in this thesis. The physics behind the generation of ultrasound with a pulsed laser is well documented in the literature[35,36], and is summarised in chapter 2. Figure 6.10

Figure 6.10 Laser generated ultrasound in a glass block, (photoelastic system).

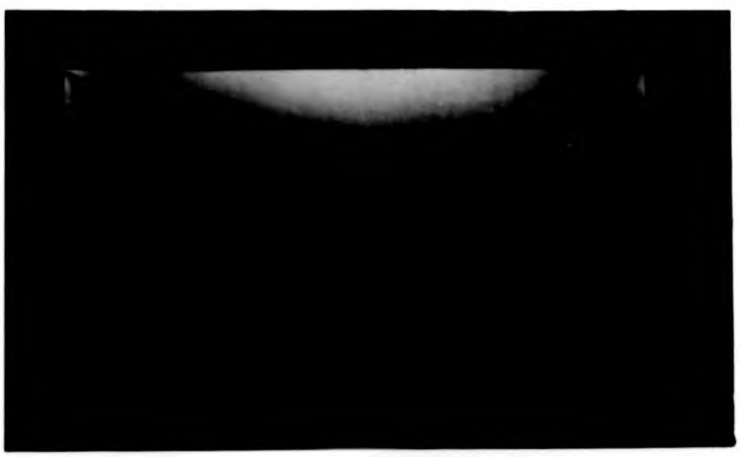

Figure 6.11 Ultrasound from a couplant-free transducer, (photoelastic system).

shows laser generated ultrasound in an image obtained with the photoelastic system. The beam from a Nd:YAG laser, delivering 4nS, 120mJ pulses of 1.06μm radiation, is focused on to the glass block on the top. The bright patch, around the point at which the laser is incident on to the sample, is caused by light from the laser, and has been partly masked by tape over the glass block. A shear wave can be clearly seen propagating away from the source, part of which has been reflected on the right hand edge of the glass. A reflected longitudinal wave is also visible. The bright lines on the right hand side of the block are due to imperfections in the glass. This photo was exposed for 45 minutes, with the laser (and therefore the L.E.D.) pulsing at 10 Hz.

3) Ultrasound from a couplant-free transducer; The output of a couplant free transducer is shown in Figure 6.11. This transducer is described in chapter 6), and shows a wavefront similar to the one generated by the 5MHz transducer in Figure 6.9a, with two exceptions, firstly that the pulse is greatly reduced in amplitude, and secondly that no shear edge waves appear to be present, which is because the delay line cannot support shear waves.

4) Ultrasound propagating through an adhesive bond; To complement the work described in chapters 3 and 4, it was thought that visualising ultrasound after it had propagated through an adhesive bond might give an insight into the effect that the structure has on the ultrasound. This photograph was taken by coupling an adhesively bonded sample, comprising of an aluminium - epoxy - aluminium sandwich, with the glass block using a thin layer of adhesive. Figure 6.12 clearly shows several wavefronts coming from multiple reflections within the adhered structure.

Figure 6.12 Ultrasound propagating through an adhesive bond, (photoelastic system).

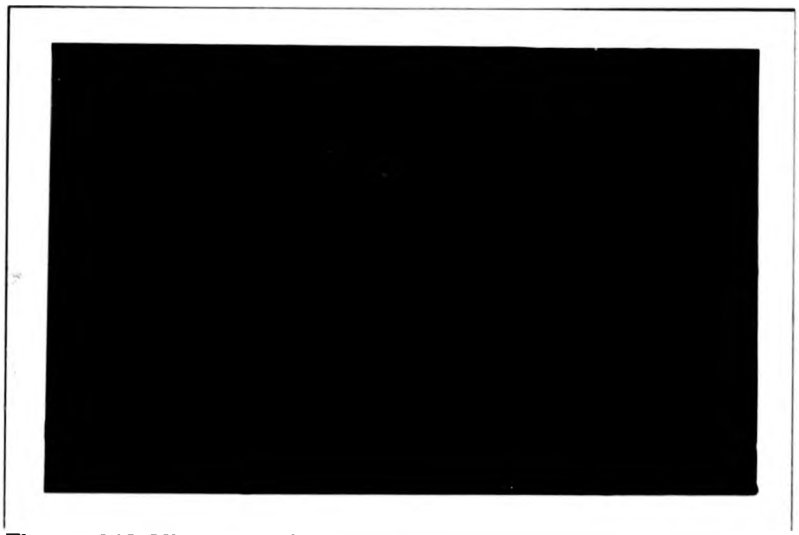

Figure 6.13 Ultrasound from a 5MHz, 0.5" immersion piezoelectric transducer, (schlieren system).

6.5 Schlieren system

6.5.1 Experimental configuration

This is shown in Figure 6.8, with the light source and C.D. lens being the same configuration as was used in the photoelastic system, but with a slightly larger L.E.D.-lens separation. This was necessary as the collection angle of this system (f20) was much smaller than in the case of the photoelastic system (f4). The lens was placed at the focal point of the first of two spherical mirrors (20' focal length, 12" diameter). After reflection from the first mirror, the light from the LED produced a plane collimated wavefront which then passed through the test medium. The beam was then focused with a second mirror to a point, where a knife edge was placed. Beyond the knife edge, the light deflected by the ultrasound was imaged on to the camera (video or film). The imaging optics consisted of a single 400mm focal length, 40mm diameter aplanatic doublet lens, (the use of such a lens was necessary as problems with spherical abberations were encountered when using a simple meniscus lens). The lens focused the light on to the body of the camera, (the camera lens was removed). The distance between the camera and the lens was altered to bring the images into focus.

The plane mirrors were used to fold the 20' long converging and diverging beams beam into the available laboratory space. Unfortunately, this reduced the distance between the sample and the stop, which reduced the sensitivity of the system, (The deflection of a ray of light by ultrasound in the sample by an angle, θ will give a displacement at the stop of $d\theta$, where d is the sample-stop distance, thus, assuming perfect optics, the sensitivity is directly proportional to the sample-stop separation). This arrangement, however was easier to use as having the

source and imaging optics in close proximity to each other, made the alignment of the system a lot easier.

The spherical mirrors were specially made for schlieren imaging applications. Normally, large diameter mirrors with long focal lengths are finished by hand to get their surfaces accurate to within a specified fraction of a wavelength of light (e.g. $\lambda/10$ for 633nm light). This process unfortunately introduces slope errors which can impede the performance of the mirror in a knife-edge system. Schlieren mirrors should always be finished on a lapping machine, so that, even though the mirrors might not be accurate to a specified fraction of a wavelength, slope errors cannot be introduced by the hand finishing. The mirrors used in the experiments were obtained second-hand, and were in fact, the same mirrors used in much of the pioneering work done on ultrasonic visualisation by Babarovski and Marsh at Tube Investments Ltd, Hinxton Hall, Cambridgeshire. The adjusters and mounts for the mirrors are the originals as used at Hinxton Hall (and are described in the literature[11]). They are mounted on a base specially made from 12mm thick boiler plate. Each mirror and mounting base weighs about 100Kg, and has been found to be very stable.

6.5.2 The Visualising Medium

For a proportion of the experiments, the ultrasonic medium was air, therefore no specimen needed to be made, however for the results taken in immersion, a water tank had to be made. The main requirement of the tank was that the transparent faces should not be bowed by the weight of the water within them. This was experienced when perspex windows were used in initial

experiments: the bowed windows acted as lenses, refracting the light from the normal. The final design of tank used 1" thick float glass windows, selected to have minimal optical inhomogeneities.

6.5.3 Image Processing

For the experiments undertaken with the schlieren system using some experimental airborne transducers, the images obtained were very weak, and were not clear enough to give any helpful information. To increase the sensitivity of the system, an image processing system was employed with the video camera. The output from the camera was fed into a 'frame grabber' in a computer, and the images were then stored, and were subsequently processed by a number of software algorithms. The final method of image enhancement used was to take two images of the field; one with the transducer turned on, one with it off. The two images were then subtracted from each other, and the difference stored in a third frame buffer. This was then repeated a number of times, and the difference images were added together. The final image was made from ten original pairs of images. This was found to give acceptable results.

6.5.4 Experiments and results- schlieren system

The schlieren system was used to look at a number of ultrasonic sources in air and in water, these were;

1) The ultrasound from conventional immersion piezoelectric transducers
2) Laser generated ultrasound in water
3) ultrasound after propagation through an adhesive bond

4) Airborne ultrasound from a transducer

5) Laser generated airborne ultrasound

1) The ultrasound from conventional immersion piezoelectric transducers; Figure 6.13 shows the ultrasonic pulse propagating from a 0.5" diameter, 5MHz immersion transducer. When this is compared to Figure 6.9b, it is seen that the width of the pulse propagating through the water has not increased as much as has the pulse propagating through the glass. This is explained by diffraction theory, as the wavelength of the ultrasound in water is around one quarter of that in glass (for the same frequency), because of the slower velocity. Longitudinal edge waves can faintly be seen as well. Unfortunately the photograph quality has been impaired by a problem with the negative, which has caused the picture to 'smudge'.

2) Figures 6.14a and 6.14b show the ultrasonic field produced by the pulsed laser (described in section 6.4.3, part 2) striking a 1mm thick steel plate in water. Figure 6.14a has a delay of 1μs, and shows both the hemispherical wave generated by the laser hitting the steel bar (seen as a semicircle), and secondly the cylindrical wave caused by the water absorbing some of the laser beam energy (seen as two parallel lines). Figure 6.14b shows the same situation, but with a delay of 10μs. This figure also shows the longitudinal wave that has been generated in the bar, and then transmitted into the water on the opposite side of the bar to the laser. Waves from multiple reflections within the steel bar are just visible. This merges into the waves generated in the water by re-radiation of Lamb waves in the bar.

3) Figure 6.15 shows ultrasound that has been reflected from an adhesively bonded

Figure 6.14a Laser generated ultrasound in water, 1μS delay, (schlieren system).

Figure 6.14b Laser generated ultrasound in water, 10μS delay, (schlieren system).

Figure 6.15 Ultrasound propagating through an adhesive bond, (schlieren system).

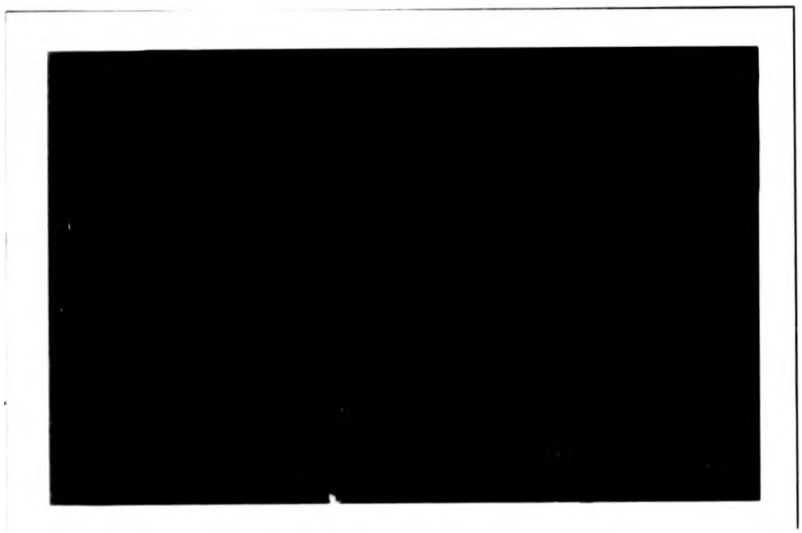

Figure 6.16a Airborne ultrasound from a capacitive air transducer, Avtek pulser, 350V, 1μS pulse (schlieren system).

sample, comprising of an aluminium - epoxy - aluminium sandwich. This was taken in immersion using a 0.5", 5MHz transducer as the source. Multiple reflections from within the sample can just be seen behind the main reflected pulse, as can a mode-converted surface wave, propagating at an acute angle to the sample.

4) To complement the work done in Chapter 6, it was thought that a demonstration of the ability to visualise the ultrasonic output from an airborne transducer would be useful for the understanding and future development of such devices. A capacitance transducer was selected to be investigated as this gave amplitudes that were sufficiently large to be visualised, this transducer had an active membrane some 37mm in diameter, and produced ultrasound around 0.25 MHz. The drive pulse to the transducer was varied, and the effect that this had on the visual appearance of the ultrasonic wave was investigated. In Figure 6.16a, the ultrasonic wave can clearly be seen as two or three straight lines parallel with the transducer. The Electrical pulse used to drive this was produced by an Avtek pulser (type AVRH-1-C), it had a delay of 30μS from the LED drive pulse, was 1μS wide, and was of 350V. Compare this with Figures 6.16b and 6.16c, which differ with Figure 6.16a in only the width of the drive pulses, Figure 6.16b has a drive pulse of 3μS, and Figure 6.16c has a drive pulse of 5μS. The effect of increasing the drive pulse from 1μS seems to be to produce two separate pulses, presumably caused by the leading and trailing edges of the pulse. Comparing Figure 6.16a with Figure 6.16d shows the effect of increasing the drive voltage from 350 to 450V. The pulse with the higher voltage is seen to be brighter, but is otherwise similar to the pulse with the lower voltage. This suggests that increasing the voltage increases the amplitude, but not the form of the pulse. Visible with a

Figure 6.16b Airborne ultrasound from a capacitive air transducer, Avtek pulser, 350V, 3μS pulse (schlieren system).

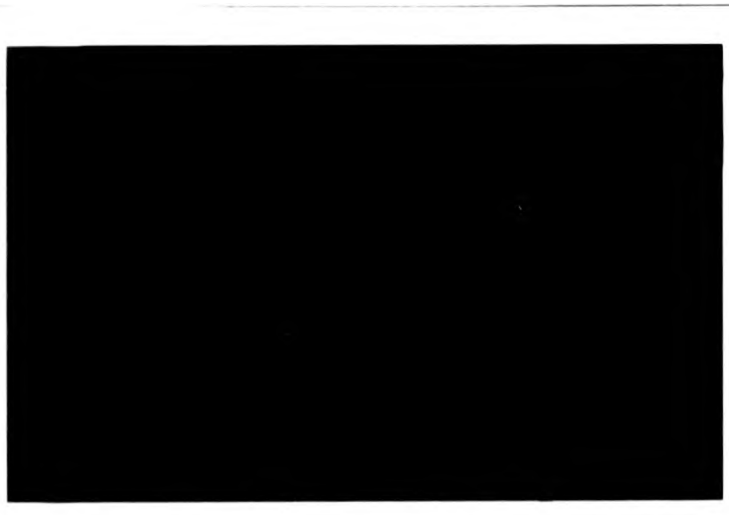

Figure 6.16c Airborne ultrasound from a capacitive air transducer, Avtek pulser, 350V, 5μS pulse (schlieren system).

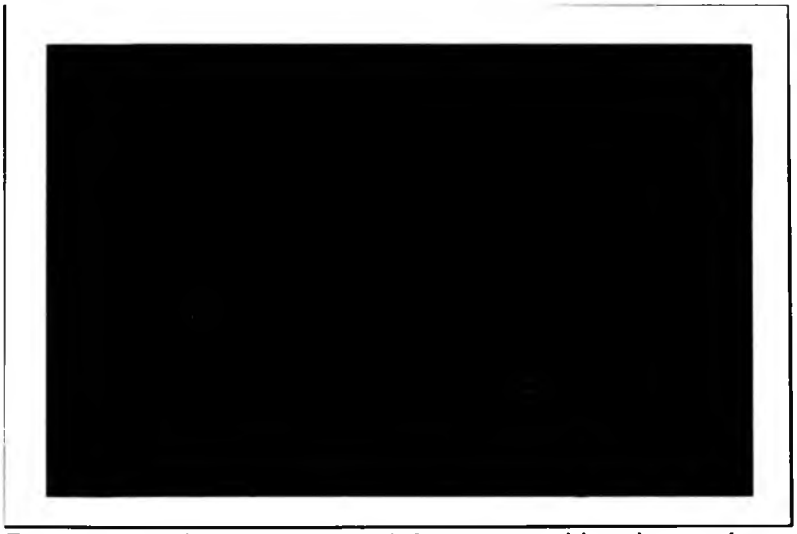

Figure 6.16d Airborne ultrasound from a capacitive air transducer, Avtek pulser, 450V, 1μS pulse (schlieren system).

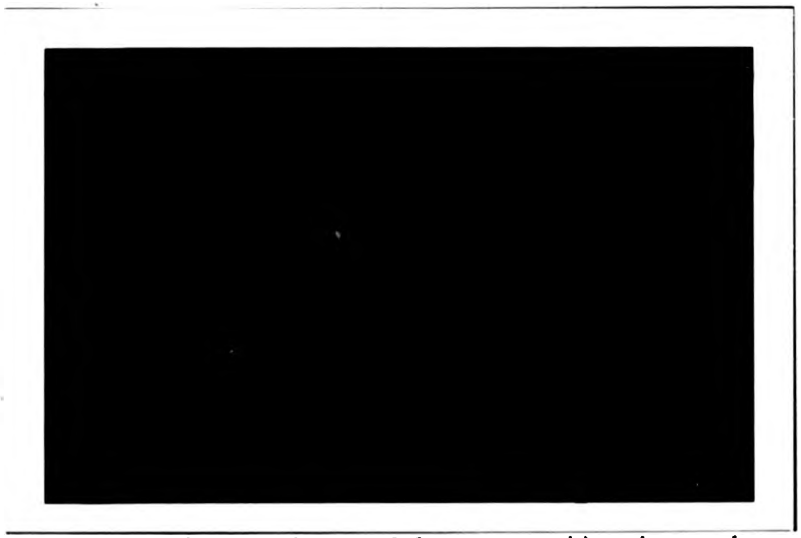

Figure 6.16e Airborne ultrasound from a capacitive air transducer, Panametrics pulser, (schlieren system).

video camera, but only barely visible in Figure 6.16d is the appearance of a multitude of tiny wavelets propagating behind the main wavefront, in a manner reminiscent of diagrams used to demonstrate Huygens construction. This suggests that the membrane is not acting as a uniform source for the ultrasound, but the ultrasound is being produced at a discrete number of points on the membrane. This substantiates current theory behind these devices. Figure 6.16e shows the air transducer being driven by a commercial piezoelectric transducer pulser (a Panametrics type 5055PR), the signal from this is only just visible, and gives very little useful information. Compare this with Figure 6.17, which is a picture of the same transducer and pulser, but captured with a video camera, and subsequently image processed as described in section 6.5.3. The clarity of the image is seen to have improved markedly, and useful information about the ultrasonic wave can now be obtained. This ultrasonic pulse seems to be, firstly, non-uniform over its width, (which was subsequently found to be caused by a defect in the membrane of the transducer), and secondly, considerably more resonant than its analog generated with the Avtek pulser. It is not known why this is, and much more work remains to be done with this system to help with the understanding of these ultrasonic airborne devices.

5) Figure 6.18 shows the airborne wave produced by a laser striking a steel bar in air, with a delay of 50μS. The hemispherical ultrasonic pulse is clearly visible on the side of the bar closest to the laser, No airborne ultrasound can be seen that is caused by the re-radiation of longitudinal waves from the steel bar into the air. This is because of the great impedance mismatch between the two media.

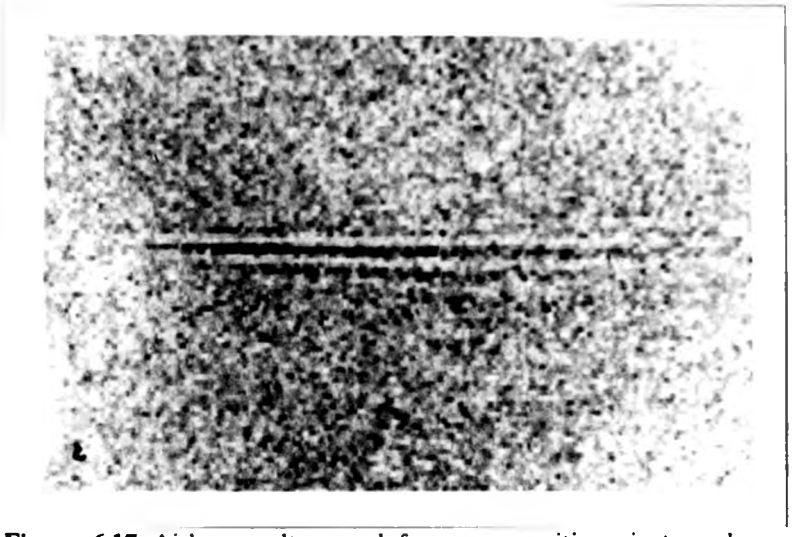

Figure 6.17 Airborne ultrasound from a capacitive air transducer, Panametrics pulser, (image processed schlieren system).

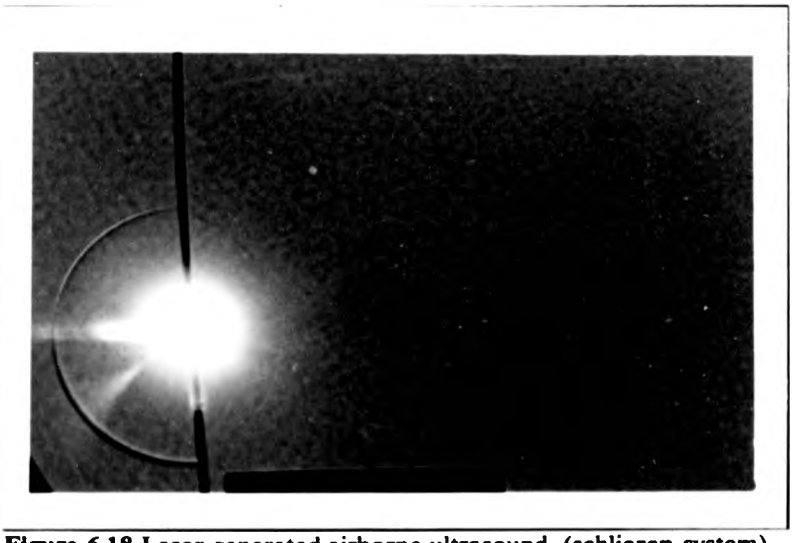

Figure 6.18 Laser generated airborne ultrasound, (schlieren system).

6.6 Conclusions

It has been shown that ultrasound can be successfully visualized in a solid (glass), a liquid (water), and a gas (air), using a variety of sources. Useful information pertaining to the generation and propagation of ultrasound has been obtained from these experiments, and has helped in the study of the phenomenon investigated in the preceding chapters in this thesis.

6.7 References

1) A.Holm and H.W.Personn, "Optical diffraction tomography applied to airborne ultrasound", Ultrasonics, 1993, Vol. 31, 4, pp. 259-265.

2) R.Eriksson, A.Holm, M.Landeborg, H.A.Personn and K.Lindström, "The 10 MHz ultrasonic near-field: calculations, hydrophone and optical diffraction tomography measurements", Ultrasonics, 1993, Vol. 31, 6, pp. 439-446.

3) R.Hooke, Micrographia observation, Vol. LVIII, pp. 217-213, 1665

4) H.W.Robinson and W.Adams,(eds) "The diary of Robert Hooke, 1672-1680", Taylor and Francis, London, 1953.

5) R.W.Wood, "Photography of sound waves, and the kinematographic demonstration of the evolutions of reflected wave-fronts", London, Edinburgh and Dublin Philosophical magazine, Vol. 50(7), pp. 148-156, 1900.

6) L.Brillouin, Ann. Phys. (Liepzig), **17**, 88.

7) P.Debye and F.W.Sears, Proc. Natl. Acad. Sci. U.S., **18**, 409, 1932.

8) R.Lucas and P.Biquard, C. R. Acad. Sci. Paris, 194, 2132, 1932.

9) C.V.Raman and R.S.Nagendra Nath, Proc. Indian Acad. Sci., A **2**, 406, 413, 1935.

10) C.V.Raman and R.S.Nagendra Nath, Proc. Indian Acad. Sci., A **3**, 75, 119, 495, 1935.

11) D.M.Marsh, "Methods of visualising ultrasound", in Research Techniques in Nondestructive Testing, Vol.2, (Academic Press, New York, R.S.Sharpe, ed., 1973), pp. 317-367.

12) V.M.Baborovsky, "Visualisation of ultrasound in solids", Phys. Technol. Vol. 10, 1979. pp. 171-177.

13) V.M.Baborovsky, D.M.Marsh and E.A.Slater, "Schlieren and computer studies of the interaction of ultrasound with defects", Non-destructive testing, August 1973, pp.200-207.

14) K.G.Hall, "Railway applications of ultrasonic wave visualisation techniques", Brit. J. NDT, March, 1984, pp.162-171.

15) K.G.Hall, "Observing ultrasonic wave propagation by stroboscopic visualisation methods", Ultrasonics, July 1982, pp.159-167.

16) D.R.Andrews, and L.J.Wallis, "Light emitting diode as a short-duration stroboscope - application to visualisation of ultrasound", in J. Phys. E, 1977, vol.10, 1975, p. 95.

17) D.R.Andrews, "Study of wavefronts in acoustic diffraction patterns using a stroboscopic schlieren technique", SPIE Vol348, High speed photography (San Diego), 1982, pp.565-570.

18) J.A.Bucaro and H.D.Hardy, "Sensitivity of the schlieren method for the visualisation of low-frequency ultrasonic waves", J. Acoust. Soc. Am. 63 (3),

March 1978, pp. 768-773.

19) B.Porter, "Quantitative real-time schlieren system for ultrasound visualisation", Rev. Sci. Instrum., 55, 2, February 1984, pp. 216-221.

20) G.H.Thomas and M.Kelley, "Ultrasonic application of schlieren imaging", Conf. 1982 paper summaries ASNT spring and fall, Boston and Pittsburgh, pp.204-207

21) J.Wilkund, "A schlieren study of the generation of different types of ultrasonic waves in thin plates", NDT International, August 1977, pp. 187-192.

22) R.C.Wyatt, "Imaging ultrasonic probe beams in solids", Brit. J. ndt, September 1975, pp.133-140.

23) D.C.Emmony, "Interaction of I.R. laser radiation with liquids", Infrared Physics, Vol. 25, No. 1-2, Feb. 1985. pp.133-139

24) Y.Bar-Cohen, B.Ben-Joseph and E.Harnik, "Schlieren ultrasonic visualisation of delaminations in composite materials", Ultrasonics, January 1979, pp. 9-10.

25) Y.Bar-Cohen, S.Kovnovish and E.Harnik, "Direct ultrasonic visualisation of fatigue cracks", NDT International, April 1980, pp.63-64.

26) A.S.Greer and B.T.Cross, "Schlieren techniques for NDT", non-destructive testing, June 1970, pp.169-172.

27) Hamamatsu technical data sheet T-107, Hamamatsu Photonics UK Ltd, Enfield, UK.

28) C.F.Ying, "Photoelastic visualisation and theoretical analyses of scatterings of ultrasonic pulses in solids", in Physical acoustics Vol. XIX, Academic

press. New York, 1990 pp. 291-343.

29) D.R.Newman, "Ultrasonic schlieren system using a pulsed gas laser", IEEE Trans. son. ultrason., Vol. SU-20, No.3, July 1973, pp. 282-285.

30) G.P.P.Gunarathne and J.Szilard, "A new stroboscope for schlieren and photoelastic visualisation of ultrasound", Ultrasonics, Vol. 21, Pt.4, July 1983 pp.188-190.

31) I.M.Hutchings and D.R.Andrews, "Light emitting diodes as short duration light sources", Proceedings of the 13th international congress on high speed photography and photonics, Tokyo, 1978. pp.222-225.

32) R.Haley and P.R.Smy, "An inexpensive light source for high-speed schlieren photography", J.Phys. E: Sci.Instrum. 21 (1988) pp.1172-1174.

33) J Krautkramer and H Krautkramer, "Ultrasonic testing of materials" Springer-Verlag, New York, 1969.

34) D.R.Billson and D.A.Hutchins, "Visualisation of laser generated ultrasound in a solid, a liquid and in air", Rev. prog. quant. N.D.E., Vol.12, New York, 1993. pp.595-601.

35) D.A.Hutchins, "Ultrasonic generation by pulsed lasers", in Physical Acoustics Vol. XVIII (Academic press, New York, W.P.Mason and R.N.Thurston, eds., 1979), pp.277-407.

36) D.A.Hutchins, R.J.Dewhurst, and S.B.Palmer, "Directivity patterns of laser generated ultrasound in Aluminium", J. Acoust. Soc. Am., 70, No.5, Nov. 1981, pp.1362-1369.

CHAPTER 7

CONCLUSIONS AND FUTURE WORK

This thesis has been devoted to studying nondestructive methods for testing materials. The theme running through the work has been the development of new transducer designs and instrumentation systems for the testing of materials which are not amenable to testing by conventional methods. This has included advanced optical, EMAT and air-coupled designs.

The first chapter of this thesis started by relating how this work fits into the context of both academic NDT research, and practical industrial applications. This chapter then described the basic theory behind laser generation, and EMAT reception of ultrasound, both of these subjects being essential for the rest of this thesis.

Chapter 2, after describing the background behind the nondestructive testing of adhesive bonds, finished with a description of a computer model that could predict the frequency response of an adhesively bonded structure. The frequency response of a typical bond, comprising of an aluminium-adhesive-aluminium "sandwich", was seen to contain a number of discrete through-thickness resonances, in the manner of "Kundt's tube". An analysis of the vibrational modes of these resonances showed that the proportion of strain-energy in the adhesive layer varied between layers. The important conclusion that was drawn from this was that a change in the adhesive layer would affect some resonances more than others, suggesting that this technique could be used for analyzing the condition of an adhesively bonded structure. This work was investigated using both shear and longitudinal waves, giving similar predictions for both.

Chapter 3 followed on from Chapter 2 by comparing the predicted frequency spectra of adhesive bonds with that produced experimentally. After the frequency response of the transduction system had been accounted for, it was found that theory and experiment corresponded very well with each other. This was repeated for both longitudinal, and for shear waves. The technique was then applied to distinguish between "good" bonding and "gross disbonding" in a sample. The frequency spectra from the "good" portion of the bond was found to be very similar to that predicted by the computer program, whereas the frequency spectrum from the "gross disbond" was found to be markedly different. The chapter followed by looking at non-contacting techniques to generate the frequency spectra, which was found to be possible with all of the techniques used (albeit with greater noise levels). One of these techniques (a laser-EMAT technique designed for longitudinal waves) was then applied to monitor the state of an adhesively bonded sample as it was heated beyond its failure point. This was seen to show the point at which the joint "failed" (disintegrated).

The rest of the chapter was devoted to the problem of detecting "poor bonds" (bonds that appeared normal, but had reduced strength). The computer program was used to predict what effect a poor bond would have on the frequency response of the specimen. Despite the fact that a number of assumptions had to be made in this model, a qualitative indication of how the frequency spectra was predicted to change was determined. This was followed by using this prediction as a guide to compare the frequency spectra between a number of samples containing a range of bonds, and plotting this against the tensile strength of the bonds (obtained by tensile testing). No correlation was found. The failure of this might

be attributed to this being only a very small effect, and factors such as noise, transducer coupling and adhesive thickness might easily have masked this effect. This was investigated by taking frequency spectra from bonds as they were being destructively tested in a tensile test rig (this reduced most of the "noise" from sources such as adhesive thickness and transducer coupling by looking at a single sample). In this case, it was found that as the bonds were stressed, the predicted changes in the frequency spectra could be clearly seen. The conclusion that must be made from this is that the spectroscopic technique works well for detecting gross disbonds, and for monitoring the deterioration of an adhesive bond under stress, but it cannot be used currently to test for poor bonding. Much work needs to be done to improve this technique to see if it can be used to look for poor bonds, particularly in the elimination of the "noise" described above. One way forward would be to use a computer program to filter out the effects of the variation in adhesive thickness between samples, and another could be to use EMATs to eliminate couplant variabilities. Despite the difficulties that such work would inevitably encounter, it was thought by the author that pursuing this line of research would be worthwhile.

Chapter 4 looked at nondestructive methods to determine the levels of hydride in zircalloy. This preliminary study was highly successful in that both ultrasonic-velocity measurements and thermal expansion measurements (dilatometry) were shown to give the solid solubility temperature of the samples, from which the hydride concentration can be determined. For this work to proceed, ways need to be developed to perform these measurements in situ inside a nuclear reactor. The laser EMAT techniques described in the chapter could be

applicable to work done in-situ, but would be very difficult to apply. A step towards addressing this application problem was made in Chapter 5 of this thesis, where air transducers that could operate at elevated temperatures were described. If these transducers could be made with sufficient sensitivity and bandwidth, then they could be made compact enough to fit inside the tubes, allowing practical testing. The dilatometry work has been taken a step further by another worker at Warwick University: the change in thermal expansivity at the solid solubility temperature has been detected in pipes with both capacitive transducers, and with strain gauges.

Chapter 5 looked at novel transducers: The first transducer was a couplant-free transducer, which was shown to perform well with a number of specimens. The development of a high frequency transducer was seen as a solution to a variety of problems that have been encountered by a number of nondestructive testing practitioners, and a great deal of interest has been expressed in this aspect of the author's work by workers throughout the world. To date, the manufacture of these transducers is being negotiated with a major NDT company, and the trial production of roller probes based on this technology has already begun.

The air transducers described in the latter part of this chapter were found to perform with varying levels of success, although none of the transducers were found to exhibit a performance comparable to that of the capacitive devices that were used for comparison. It must, however be remembered that these transducers were investigated because they were wholly novel, not because they were expected to surpass the capacitance devices. It must also be taken into consideration that capacitance devices have been investigated for many years, whereas these devices

have had, by comparison, only a very brief amount of effort put into them. The optical detector was found to work with the air transducers, but was found to exhibit extremely low sensitivity. Theory suggests that the bandwidth and the spatial resolution of such a detector are very high (although, with such noisy signals, this could not be verified), and the detector could, (with greater sensitivity) be extremely useful as a high quality optical detector for calibrating ultrasonic transducers. Whilst the sensitivity of this detector in air would be difficult to improve (because of the refractive index of air being very close to 1), such a device could operate well in immersion, and experiments are planned to verify this. If this is found to be the case, then as well as a tool for characterising the optical field from an immersion transducer, this detector might also be applicable to ultrasonic holographic techniques.

Chapter 6 described the construction and use of both a schlieren, and a photoelastic rig for visualising ultrasound. Both rigs were found to work well with the samples and probes investigated, allowing a large number of photographs to be taken. It can be argued that the quantitative conclusions that can be drawn from this aspect of the work do not give full justice to the power of the visualisation techniques, especially as many of the better results can only be wholly appreciated by observing a moving image, which, of course cannot be included in a thesis. However the photographic records obtained with this setup and given in Chapter 6, can be seen as an insight into the valuable contribution that this part of the work gave to the author's understanding of some of the complex ultrasonic propagation phenomena that were encountered in the work described in the preceding chapters. The photographs given with Chapter 6 depict phenomena

including laser-generated ultrasound, ultrasound propagating through adhesive bonds and ultrasound from a couplant free transducer, as well as ultrasound from an air transducer. It can be argued that a full appreciation of the value of this work can only be obtained by the reader using the rig directly. It is hoped this work will continue with experiments that use the schlieren rig as an aid to developing both the capacitive, and the new air transducers described in Chapter 5.

To conclude, it is hoped that the work described in this thesis has contributed to the field of ultrasonic nondestructive testing, and that the work described here will lead to new and improved NDT techniques.

Bibliography

The set of guidelines followed in the preparation of this thesis is PHYS/PG/3, which relates to the University document "Guide to examinations for higher degrees by research".

This thesis was written using the "face-lift for word perfect" and "Word Perfect 5.1" word processing packages, and is printed in a 12 point Dutch-Roman typeface.

The publications arising from this work are as follows;

1) Ultrasonic testing of adhesivley bonded layers using shear waves, D.R.Billson and D.A.Hutchins. Ultrasonics International 1991 conference proceedings, pp.447-450

2) Laser-EMAT ultrasonic measurements of bonded metals, D.R.Billson and D.A.Hutchins. Nondestr. Test. Eval., Vol 10, pp. 43-53. 1992

3) Resonance studies of bonded Aluminium joints, D.A.Hutchins, L.F.Bresse and D.R.Billson. Nondestr. Test. Eval., Vol 10, pp. 149-165. 1992

4) Ultrasonic shearwave measurements of phase transitions in zircalloy at elevated temperatures, D.R.Billson and D.A.Hutchins. Rev. Prog. Nondestr. Eval., Vol 12, pp 1661-1666, New York, 1993

5) Visualisation of laser generated ultrasound in a solid, a liquid and in air, D.R.Billson and D.A.Hutchins. Rev. Prog. Nondestr. Eval., Vol 12, pp. 595-601, New York, 1993

6) Development of a novel piezoelectric ultrasonic transducers for couplant-free non-destructive testing, D.R.Billson and D.A.Hutchins, British journal of NDT., December 1993, pp. 705-709

7) Nondestructive evaluation of hydride concentration in zirconium-niobium alloys, D.R.Billson and D.A.Hutchins, submitted to JASA.

Fin.

"Round the back for the old brandy then Wal."
Sir Harry Secombe as "Neddy Segoon" in "The Goon show"

TITLE ADVANCED NON-CONTACTING ULTRASONIC TECHNIQUES FOR NON-DESTRUCTIVE TESTING.

AUTHOR Duncan Robert BILLSON

DEGREE Ph.D

AWARDING BODY Warwick University

DATE 1994

THESIS NUMBER DX190831